Target Design, Signature and Biases

AMPLITUDE CORRECTIONS TO DELAY MEASUREMENTS

John Luck, Tom Stamp, Mark Elphick and Suzanne Jackson

Orroral Geodetic Observatory
Australian Surveying and Land Information Group
PO Box 2, Belconnen ACT 2616, Australia

Phone: +61 (6) 235-7111
Fax: +61 (6) 235-7103
E-mail: johnluck@auslig.gov.au

Abstract

The relationship between delay variations and received signal strength has been calibrated for the MCP in use at Orroral, and the resulting linear formula is routinely applied to all satellite measurements on a shot-by-shot basis. The calibration is effected by varying several parameters such as MCP voltage, PLZT polarization and pointing while ranging to the ground target and the real-time external calibration target. This procedure has resulted in substantial improvement in station performance especially on the stronger satellites. Fitting a cubic polynomial over a limited amplitude range can give even better results.

The procedure has also proved to be a valuable diagnostic tool.

1. Introduction

It is well known that the propagation delay in a laser ranging system depends upon the intensity of light hitting the detector, and voltage applied to the detector. It is one of the functions of the discriminator to eliminate - as far as possible - the delay variations arising from such amplitude variations coming from the detector. A great deal of effort, and mystic art, goes into setting up the discriminator in stations using MCP-type detectors. Nevertheless, delay variations remain which affect adversely the precision and accuracy of ranging results, especially for very 'bright' targets such as TOPEX/POSEIDON and AJISAI which yield uncontrollably large fluctuations in received intensity.

The relationship between delay variation and amplitude variation has been calibrated by measuring these quantities as the intensity of return signal from local calibration targets, and MCP voltage, are varied in a controlled manner. It has been found that substantial improvements in satellite r.m.s., and some improvement in range biasses, result.

2. Experimental Configuration

The equipment used is exactly the same as used in normal ranging to satellites and to ground targets. It is described in Table 1. The physical arrangements are as shown in [Luck,1994]. The "PLZT" operates for the calibration targets "Spider" and "Rock" but not for satellites, and is varied by the operator during ranging to equalize (approximately) the signal strengths being received from both "Spider" and the satellite at the time.

Being a polarization-induced attenuator, the transmission T of the PLZT is given by:

$$T = A + B \sin^2(\pi P/2000)$$

where A and B do not need to be known, and P is the setting between 0 and 1000 which controls the voltage applied to the PLZT. The amplitude from the MCP nominally doubles for each 100 volt increase in its applied voltage M.

As the parameters P and M are varied, the following observables are measured every shot:

s:	Signal strength from Charge Digitizer, in arbitrary counts (0-1024)
c:	Real-Time ("Spider") Calibration delay, in nanoseconds
r:	Ground target ("Rock") delay residual, O-C, in nanoseconds.

TABLE 1 : Equipment Configuration for Amplitude Dependence Calibration

Ground Target:	50mm solid retroreflector on a "Rock" 1.1km distant
Real-Time Target:	20mm solid retroreflector mounted on telescope "Spider" vanes
Variable Filter:	"PLZT", electrically controlled crossed polarizing ND filter
Detector:	ITT F4129f z-plate "MCP" PMT
Discriminator:	Tennelec 454 CFD cascaded according to NASA setup
Charge Monitor:	LeCroy 2249A ADC "Charge Digitizer", accessed via CAMAC Dataway
Event Timer:	LeCroy 2229A TDC, modified, accessed via Electro Optic Systems MRCS

3. Linear Model for Calibration

The calibration model adopted in November 1995 has the following form for each return 'i':

$$c_i = c_0 + a.(s_i - 130)$$

$$r_i = r_0 + a.(s_i - 130)$$

where s, c and r are defined above, c_0 and r_0 are the estimated values when the signal strength reads 130 - which was the average value observed from LAGEOS I & II passes over the previous twelve months - and the most important estimated value is 'a', the slope in nanoseconds/count. The observation equations are coupled through the solution parameter 'a', so are solved together by the method of least squares.

Subsequently, the range 'x' nanoseconds on every shot 'j' is corrected by:

$$x_j(\text{corrected}) = x_j - a.(s_j - 130).$$

3.1 Cubic Model

A cubic model of the following form has been tested but not implemented:

$$c_i = c_0 + a.(s_i - 130) + b.(s_i - 130)^2 + c.(s_i - 130)^3$$

$$r_i = r_0 + a.(s_i - 130) + b.(s_i - 130)^2 + c.(s_i - 130)^3$$

4. Results

Figure 1 shows how the signal strength (amplitude) measurements vary as the parameters P (PLZT setting, in counts) and M (MCP volts) are varied, from a session of ground target ranging in which each setting was held for one minute, yielding approximately 250 returns per setting. It is clear that, particularly for the Ground Target, the $\sin^2 P$ law for the PLZT applies approximately, until the signal strength exceeds 500 counts.

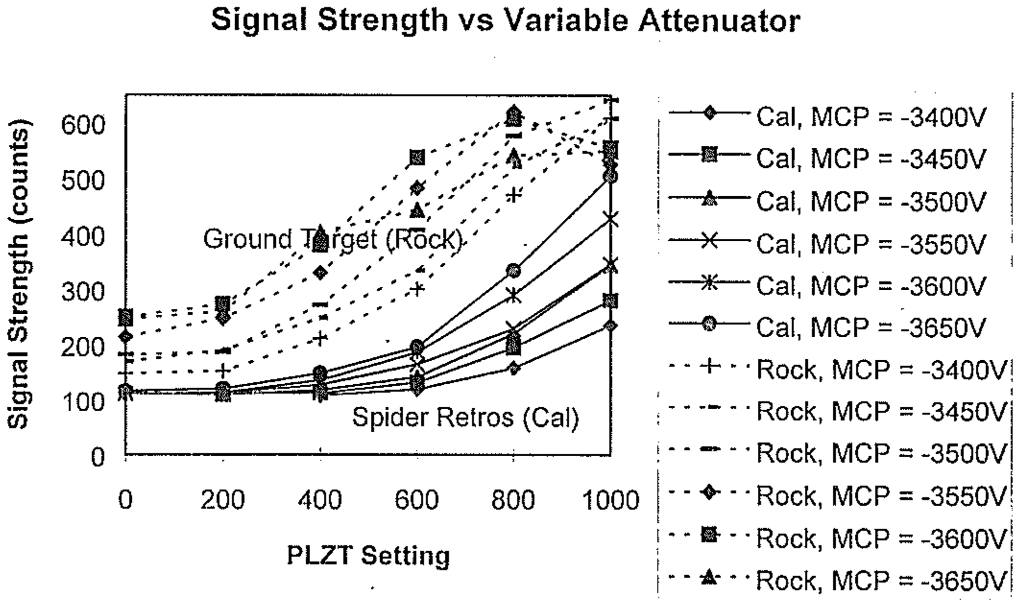

Figure 1: Amplitude variation as PLZT setting and MCP volts are varied systematically.

In Figure 2, the corresponding effects on propagation delay are plotted, relative to an arbitrary zero point. There is a very large increase in delay for large PLZT settings and high MCP volts, ie when signal strength exceeds 500 counts.

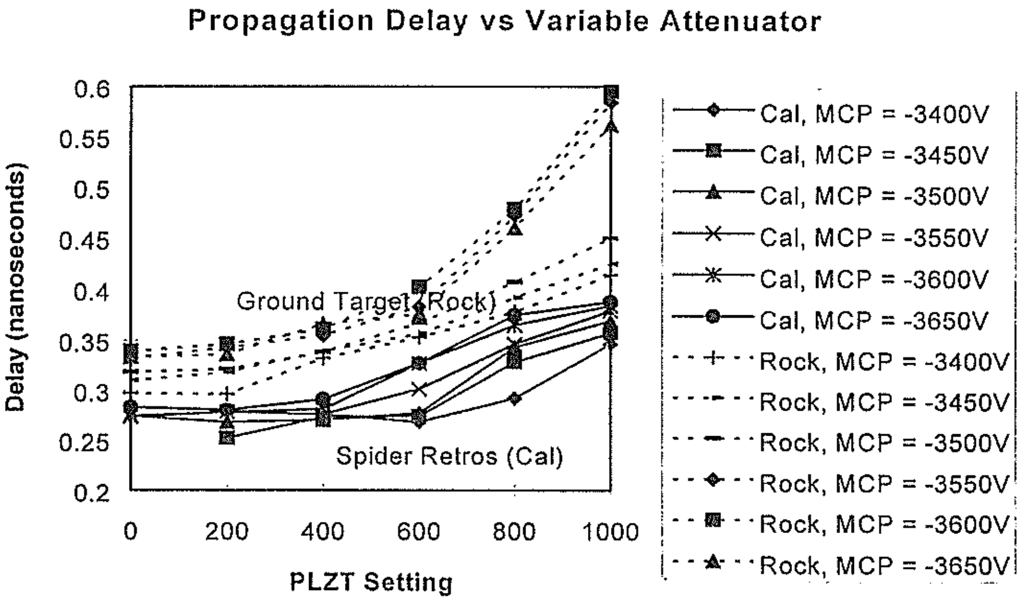

Figure 2: Propagation delay variation as PLZT setting & MCP volts are varied systematically.

4.1 Linear Model Fit

The linear model was then fit to the Delay vs. Signal Strength data implicit in Figures 1 and 2. The residuals from the fit are shown in Figure 3. Note that, for clarity in the graph, 1000 counts have been added to the Signal Strength values for the Rock residuals on the right-hand side of the graph - they really overlap the points for the Spider in the left-hand half. Obviously, some points above 520 counts (shown as 1520 counts) should have been deleted - they are the same points showing non-standard behaviour in Figures 1 and 2.

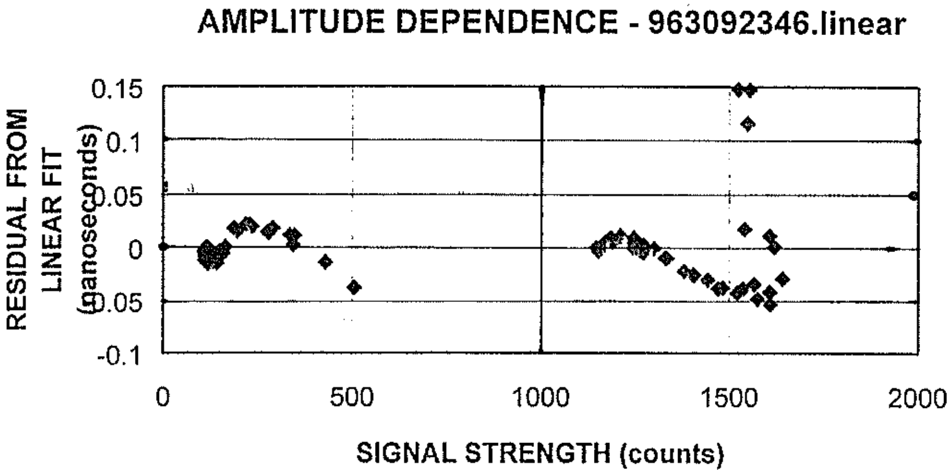

Figure 3: Residuals from linear fit to amplitude calibration data. Note that ground target data has been shifted to the right by 1000 counts, for clarity.

A similar procedure was followed for a set of calibration data observed in October 1995. Its linear solution yielded:

a = 0.409 picoseconds/count :- adopted on 26 November 1995
r.m.s. of residuals about the fit = 15 picoseconds.

4.2 Cubic Model Fit

Figure 4 shows the results when the cubic model is fitted through the previous data set, restricted to signal strengths less than 520 counts. Again, the Rock values have 1000 counts artificially added for graphing clarity. The r.m.s. of the residuals is now 6 ps. The repeatability of this result has not yet been established, so it has not been adopted.

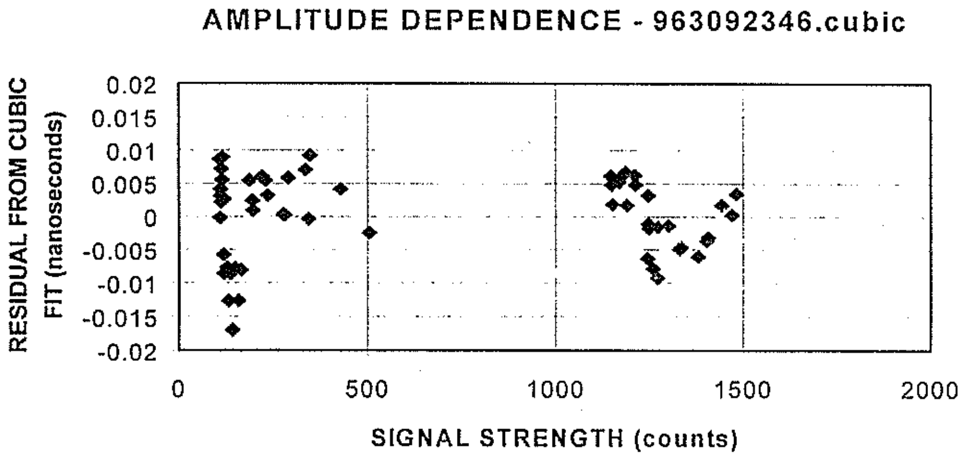

Figure 4: Residuals from a cubic fit to amplitude calibration data, restricted to signal strengths less than 520 counts. Note that ground target data has been shifted to the right by 1000 counts, for clarity.

4.3 A Pathological Case

A set of data taken on a previous occasion is displayed in Figure 5. Something is wrong!

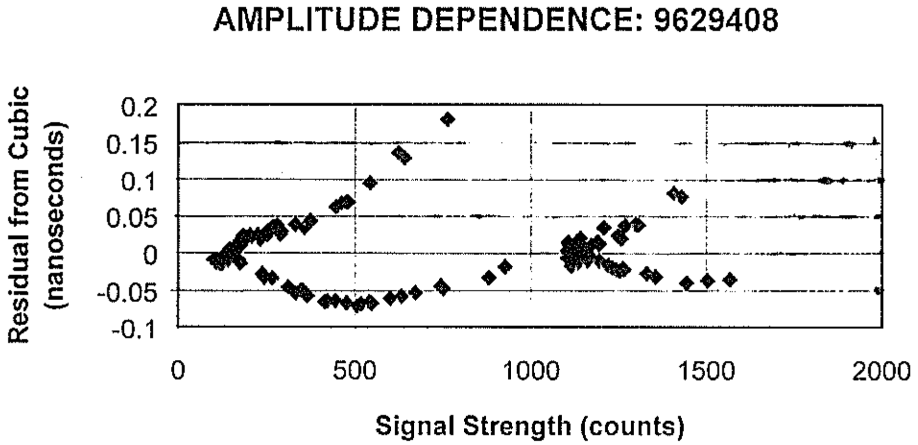

Figure 5: Residuals from a cubic fit to some pathological data. Note that ground target data has been shifted to the right by 1000 counts, for clarity.

It turns out that, due to a malfunction of a Ledex flip mirror, the beam was hitting the edge of the MCP aperture, not the centre. This type of analysis, plus careful examination of the shapes of the curves in Figures 1 and 2, have proved to be very useful diagnostic tools.

5. Effect on Precision and Range Bias

Application of the linear model correction has reduced the Orroral LAGEOS r.m.s. from about 70 ps single-shot to typically 45 ps. As expected, little effect has been noted on the range biasses for LAGEOS as reported in the University of Texas Center for Space Research's weekly analyses because the model has been normalised to LAGEOS results and the amplitude variation is small, anyway.

Topex/Poseidon range biasses improved considerably as a result [Dunn,1996]. Figure 6 illustrates a pronounced move towards zero and much smaller scatter of range biasses from Cycle 118 which started on 95 Nov 17, about when the new algorithm was implemented. These data from the TOPEX Precision Orbit Determination Group do not contain the spurious height rate of 9.3mm/year previously attributed to Orroral. Dunn's data also shows a decrease in the Normal Point r.m.s. from 15mm to 9mm from the same date.

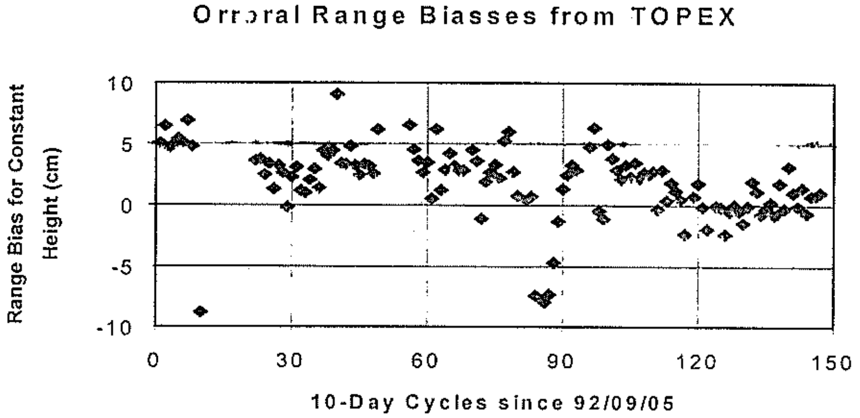

Figure 6: Orroral range biasses from Topex/Poseidon data [Dunn,1996]. The new algorithm was introduced at Cycle 118.

6. Summary and Conclusions

The linear model has been adopted with confidence in its applicability because of the controllability and repeatability of the calibration experiments which use identical equipment and configurations as in normal ranging operations. It has produced substantial improvements to r.m.s. of ranging results, both for single-shot and normal-point estimations. Range biasses from TOPEX/POSEIDON have reduced and tightened noticeably.

The adopted value for the slope coefficient is 0.409×10^{-3} *nanoseconds/count. It was implemented on 26 November 1995.*

The calibration procedure should be repeated at regular intervals, both because the constants need to be verified, and because the procedure highlights malfunctions in the ranging system.

An improved model obtained by fitting a cubic polynomial instead of a straight line, and by restricting amplitudes to certain admissible limits, can reduce the r.m.s. error from this source to 6 ps. It will undoubtedly be introduced in due course.

7. References

Dunn, P.J. (1996): Private communication - Topex data.

Luck, J.McK (1992): "Performance of the Upgraded Orroral Laser Ranging System", Proc. 8th International Workshop on Laser Ranging Instrumentation, Annapolis, MD, NASA Conf.Publ. 3214, p.11-6 ff.

ACCURACY OF THE SATELLITE LASER RANGING

S.SCHILLAK

SPACE RESEARCH CENTRE
OF POLISH ACADEMY OF SCIENCES
BOROWIEC ASTROGEODYNAMICAL OBSERVATORY
62-035 KÓRNIK, POLAND
tel: +48-61-170-187
fax: +48-61-170-219
e-mail: sch@cbk.poznan.pl

ABSTRACT. Accuracy of laser measurements is one of the most important parameters of SLR systems which determines the reliability and thus usefulness of results. It is of particular significance in determination of coordinates in the geodynamic projects. Accuracy includes contributions of two components: random error and systematic biases, and care should be taken to keep them as low as possible. The paper discusses contributions due to main sources of single shot RMS including: laser pulse width, detector time spreading, precision of time interval counter and electronic systems. Systematic bias combines the effects of the atmosphere, standard frequency inaccuracy (range bias and time bias), calibration system (the problem of the mean level of return pulses), accuracy of meteorological read out, target distance and position of the reference point. The effects of the photons distribution in front of the detector such as range bias dependence on the signal strength and pulse attenuation, and skewness in the residuals distribution were the subjects of particular interest.

The main aim of satellite laser ranging is determination of a distance between a stable point of the telescope and the satellite mass centre. This distance should be measured with a maximum accuracy, that is our results should be as close as possible to the real distance between these points. Each process of physical measurement is charged with two kinds of errors: random ones (precision) and systematic biases.

1. Precision.

The ideal measurements give a normal distribution of deviations. Other distributions can be expected when the effect of an experiment is asymmetrical or our experiment is disturbed by certain physical phenomena. In such situations the problem appears of a systematic bias as a difference between the peak value and the mean in the distribution of deviations. Table 1 gives contributions of the main sources of random errors in the satellite laser ranging which are the width of a laser pulse, jitter of the detector and precision of the electronics. The contributions due to these sources have been estimated for the best parameters of SLR systems in 1996 and for the corresponding parameters expected to be achieved in the year 2000. The contribution of the laser pulse width has been estimated taking into account the distribution of photons in front of the detector for the single-photoelectron level and the standard deviation of this distribution in centimetres. The standard deviation of the detector time spreading was assessed assuming that the detector jitter for a single-photoelectron pulse is 3σ. The standard deviation of errors due to the electronics (mainly the time interval counter or event timer) can be found experimentally (inner calibration without the detector) and the result is usually in agreement with technological specification of the instrument. In general we know the precision on site immediately after the satellite pass, and then sources of significant random errors can be found for each station. This RMS can be additionaly reduced by assuming normal points as means in certain time intervals.

Table 1. **PRECISION**
(Single Shot RMS)

ERRORS SOURCES	THE BEST SYSTEM 1996	NEAR FUTURE
WIDTH OF THE LASER PULSE - 35 ps => 20 ps	±1.7 mm	±1.0 mm
DETECTOR'S JITTER 100 ps => 25 ps	±5.0 mm	±1.2 mm
ELECRONIC'S JITTER 25 ps => 10 ps	±3.7 mm	±1.5 mm
TOTAL SINGLE POINT RMS	±6.4 mm	±2.2 mm
TOTAL NORMAL POINT RMS	±0.6 mm	±0.2 mm

Table 2. **SYSTEMATIC BIASES**

ERRORS SOURCES	THE BEST SYSTEM 1996	NEAR FUTURE
ATMOSPHERIC PROPAGATION	±5 mm	±2 mm
METEOROLOGICAL MEAS.	±1 mm	±1 mm
SATELLITE CENTRE OF MASS	±2 mm	±1 mm
SIGNAL STRENGTH VARIATION	±3 mm	±2 mm
TEMPORAL VARIATION	±2 mm	±1 mm
CALIBRATION PATH	±1 mm	±1 mm
CALIBRATION PATH - METEO	±1 mm	±1 mm
MOUNT ECCENTRICITIES	±1 mm	±1 mm
TOTAL	±6.8 mm	±3.7 mm

Table 3. **MAIN PROBLEMS**

ATMOSPHERE MODEL => TWO-COLOR RANGING

SATELLITE CENTER OF MASS => NEW TYPES OF CUBE CORNERS

CALIBRATION METHOD => SIGNAL STRENGTH
SATELLITE = CALIBRATION

PRECISION UPGRADING => BETTER DETECTORS
NEW TIME INTERVAL COUNTERS (<10 PS)
SHORTER LASER PULSE

ORBITAL METHOD => ACCURACY BETTER THAN 1 CM

COST => NEW GENERATION AUTOMATIC
STATIONS

MAX. ACCURACY
NOW = ±9 mm => FUTURE = ±4 mm

2. Systematic biases.

Identification and determination of systematic errors is much more difficult. The information on the contribution of systematic biases can be obtained after analysis of the satellite orbit, and unfortunately, the contribution of the errors following from the orbital method is significant particularly for the best stations. The main sources of systematic deviations are specified in Table 2. The problems related to the accuracy of measurements and the proposed ways of their elimination are illustrated in Table 3. The most important problem is the atmospheric delay which is probably greater than 5 mm but unfortunately, this effect has been rather poorly recognised. The use of two- or multi-colour measurements can reduce the contribution of this effect to about 2 mm, however, high cost and technological difficulties inhibit realisation of this task . The other systematic biases are relatively small and not so difficult to establish. Among them particular attention should be paid to the effects of varying the strength of the return signal. This effect is particularly important for photomultipliers and avalanche photodiodes where it is known as the time walk.

3. Signal strength variation.

Systematic bias related to the varying strength of the return signal originates from two sources: a distribution of photons in front of the detector and the amplitude of the return signal. The second source is related to the types of the detector and discriminator used and is discussed in detail in a few other papers in these Proceedings. The mean distribution of photons in front of the detector, for a gaussian laser pulse of full width of 200 ps and a few levels of the signal strength is illustrated in Fig. 1. For a weak signal the detector start is delayed and when the calibration is not at a similar level the results will be charged with range bias. In order to avoid this problem particular care should be taken to control the strength of the return signal during the calibration and satellite observation. For the multi-photoelectron method the effect will be more pronounced because of changes in the signal strength during the satellite pass and difficulties in establishing a proper mean calibration amplitude. For the single-photoelectron method the situation will be more stable. Moreover, the use of an attenuator eliminates inner pulses and the probability of range bias occurrence diminishes.

Another effect due to a distribution of photons in front of the detector is the skewness of the pulse. This effect appears for weak single photoelectron pulses (Fig. 2), as the probability of the detector start by photons on the right - hand side is greater (greater number of photons) than by those on the left. Consequently, the distribution of deviations is asymmetrical. For strong pulses this effect is very small so in practice it can be neglected. The contributions due to all the effects related to the varying strength of the signal can be reduced by the use of shorter laser pulses.

The effects related to the varying strength of the return signal have been assessed on the basis of laser observation data from Borowiec SLR collected in October 1996. The passes of LAGEOS are divided into two populations, those with weak signals (12 passes, less than 300 returns per pass) and strong signals (11 passes, about 700 returns per pass), see Figs. 3a and b, respectively. For weak signals the skewness and the difference between the peak value and the mean (12mm) are clearly visible, whereas for strong signals these effects do not appear. A similar analysis was performed for the distribution of calibrations for exactly the same passes, see Figs. 4a and b. The results are similar which means that the level of the calibration signal is similar to that of the observed signal, consequently, the range bias of results of the laser ranging in Borowiec is not caused by the effects of this kind. The effect of the signal attenuation is noticeable in the passes of TOPEX/ POSEIDON. For LAGEOS we do not use the attenuator while for low satellites we use 8dB attenuation. In the case of the latter, RMS is lower and the distributions of deviations for the observations (Fig. 5a) and calibrations (Fig. 5b) are close to the normal one without the skewness and significant differences between the peak and the mean. However, the calibrations are a bit too good.

Acknowledgements.
This work was supported within the grant Z/137/t12/96/07 of the Committee for Scientific Research.

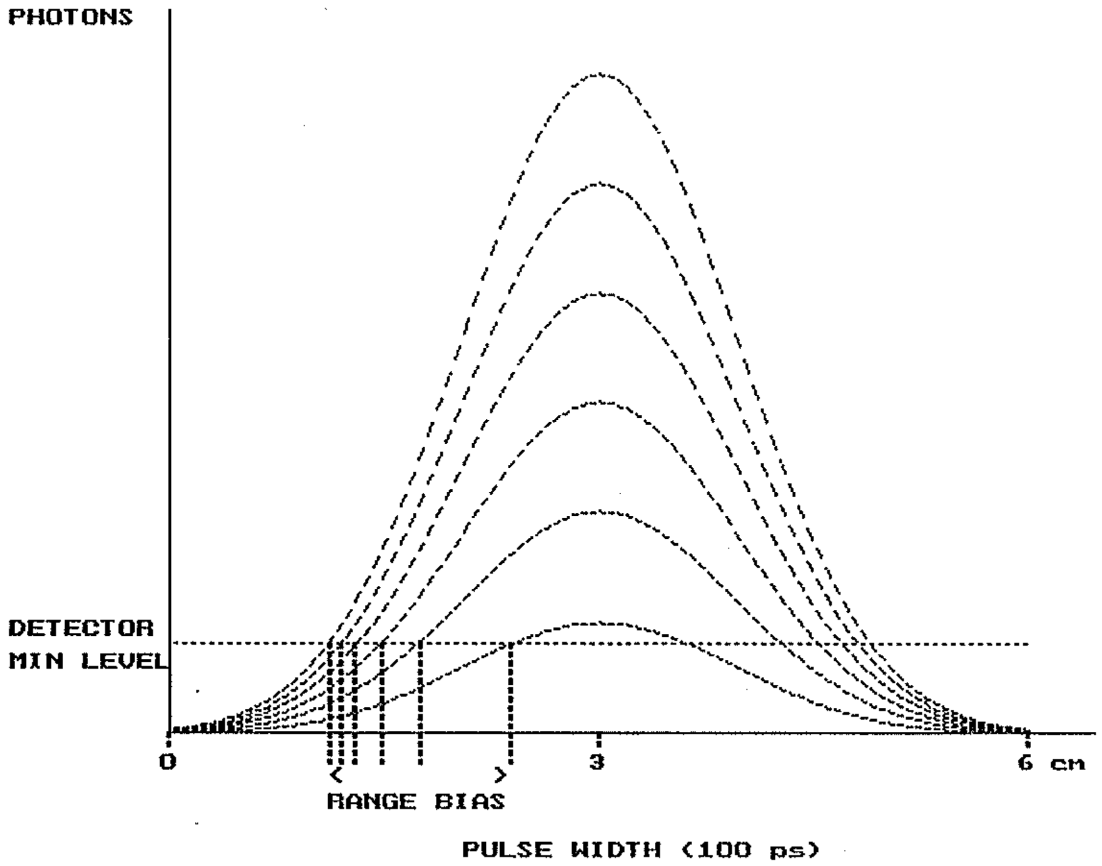
PHOTONS
DETECTOR
MIN LEVEL
0
3
6 cm
<
>
RANGE BIAS
PULSE WIDTH (100 ps)

Fig. 1

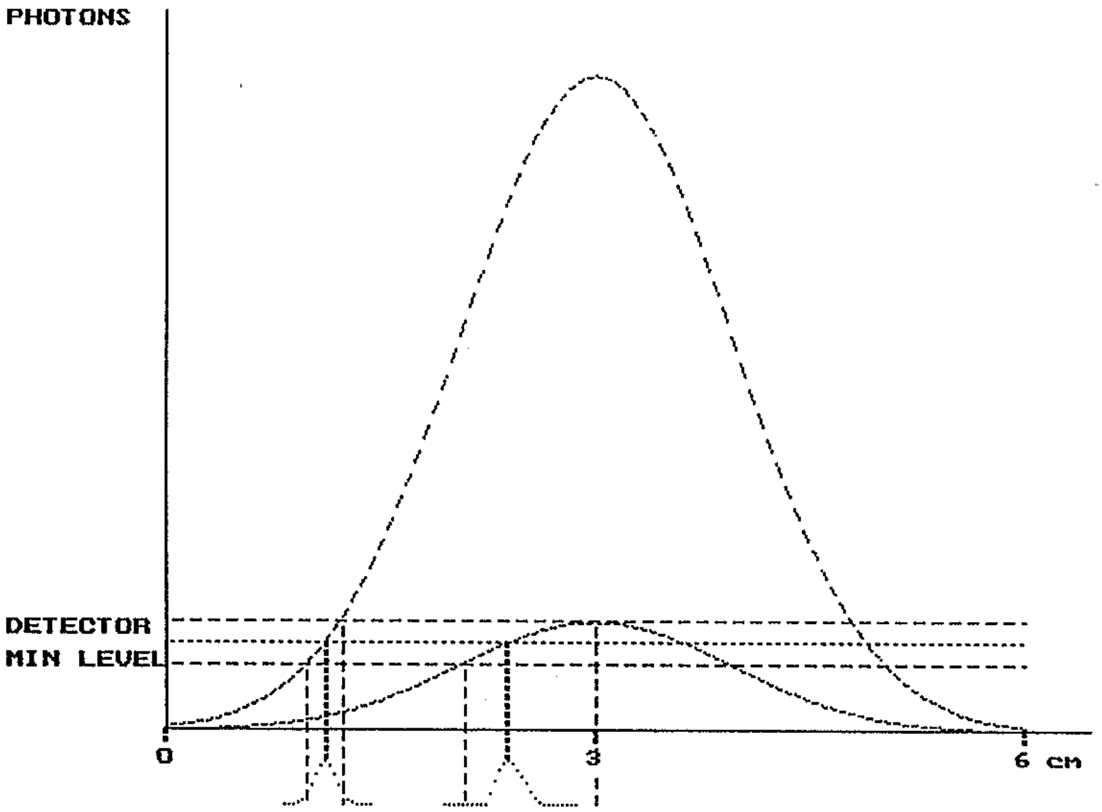
PHOTONS
DETECTOR
MIN LEVEL
0
3
6 cm

Fig. 2

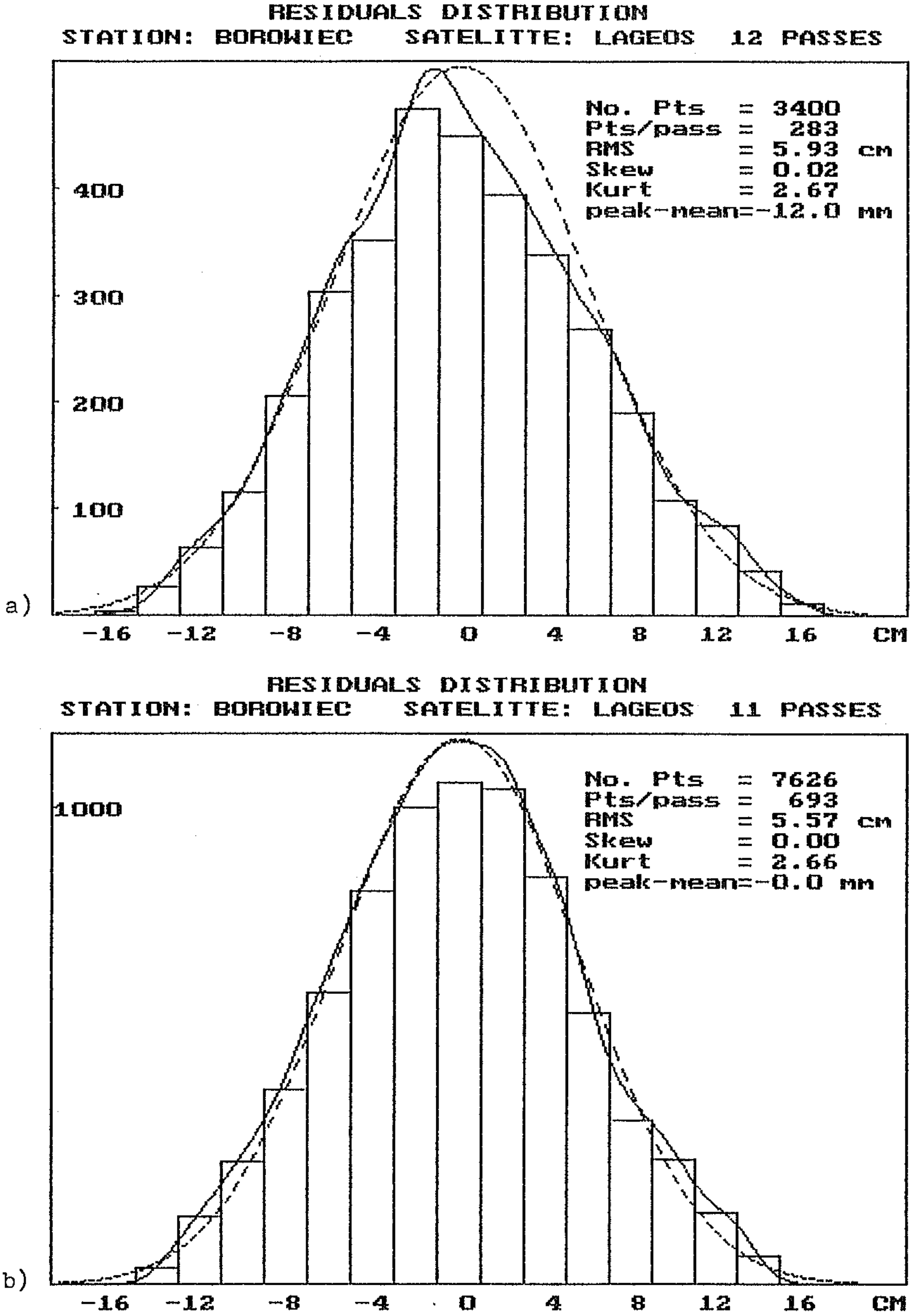
RESIDUALS DISTRIBUTION
STATION: BOROWIEC SATELITTE: LAGEOS 12 PASSES
No. Pts = 3400
Pts/pass = 283
RMS = 5.93 cm
Skew = 0.02
Kurt = 2.67
peak-mean=-12.0 mm
400
300
200
100
a)
-16
-12
-8
-4
0
4
8
12
16
CM
RESIDUALS DISTRIBUTION
STATION: BOROWIEC SATELITTE: LAGEOS 11 PASSES
No. Pts = 7626
Pts/pass = 693
RMS = 5.57 cm
Skew = 0.00
Kurt = 2.66
peak-mean=-0.0 mm
1000
b)
-16
-12
-8
-4
0
4
8
12
16
CM

Fig. 3

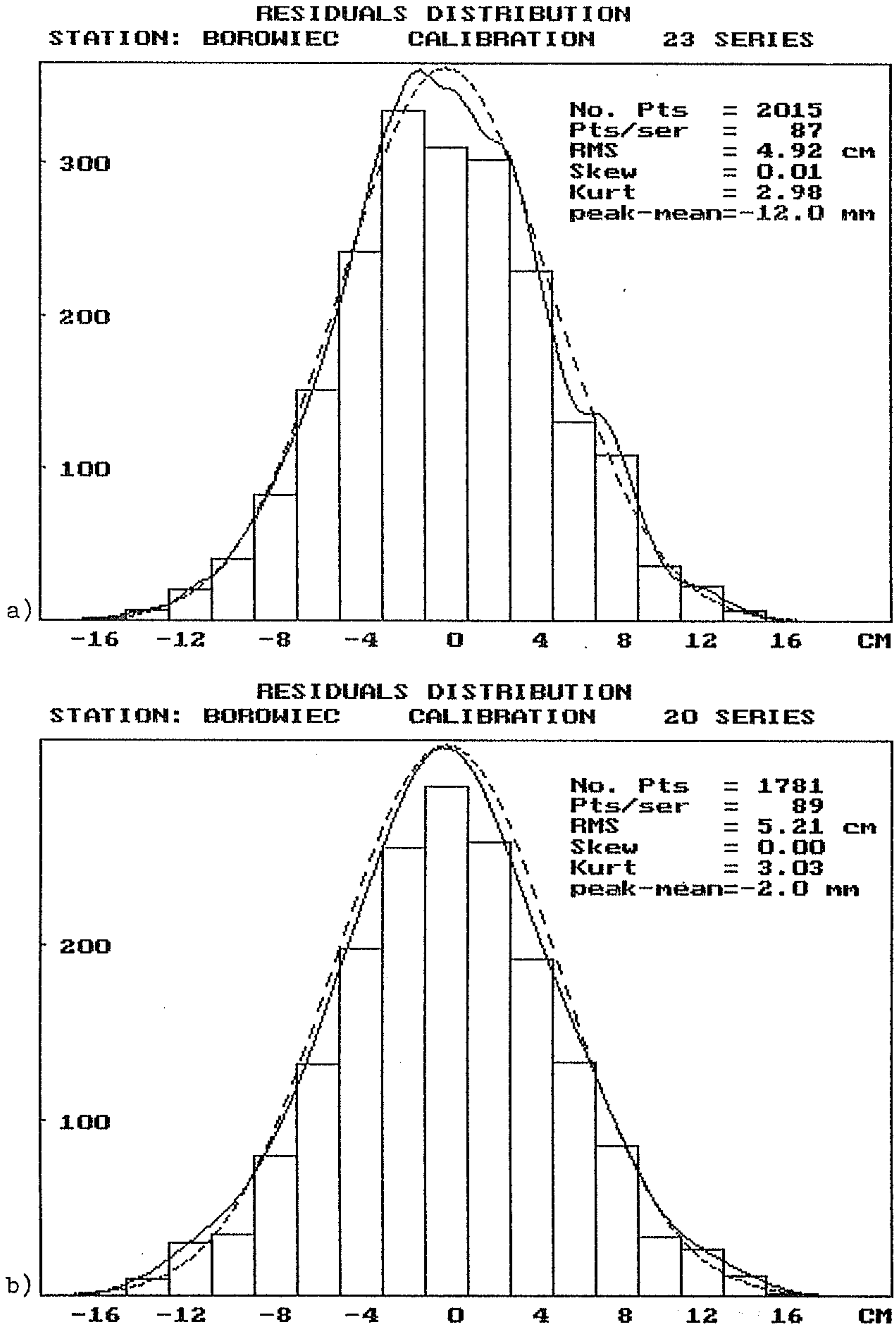
RESIDUALS DISTRIBUTION
STATION: BOROWIEC CALIBRATION 23 SERIES
No. Pts = 2015
Pts/ser = 87
RMS = 4.92 cm
Skew = 0.01
Kurt = 2.98
peak-mean=-12.0 mm
300
200
100
a)
-16
-12
-8
-4
0
4
8
12
16
CM
RESIDUALS DISTRIBUTION
STATION: BOROWIEC CALIBRATION 20 SERIES
No. Pts = 1781
Pts/ser = 89
RMS = 5.21 cm
Skew = 0.00
Kurt = 3.03
peak-mean=-2.0 mm
200
100
b)
-16
-12
-8
-4
0
4
8
12
16
CM

Fig. 4

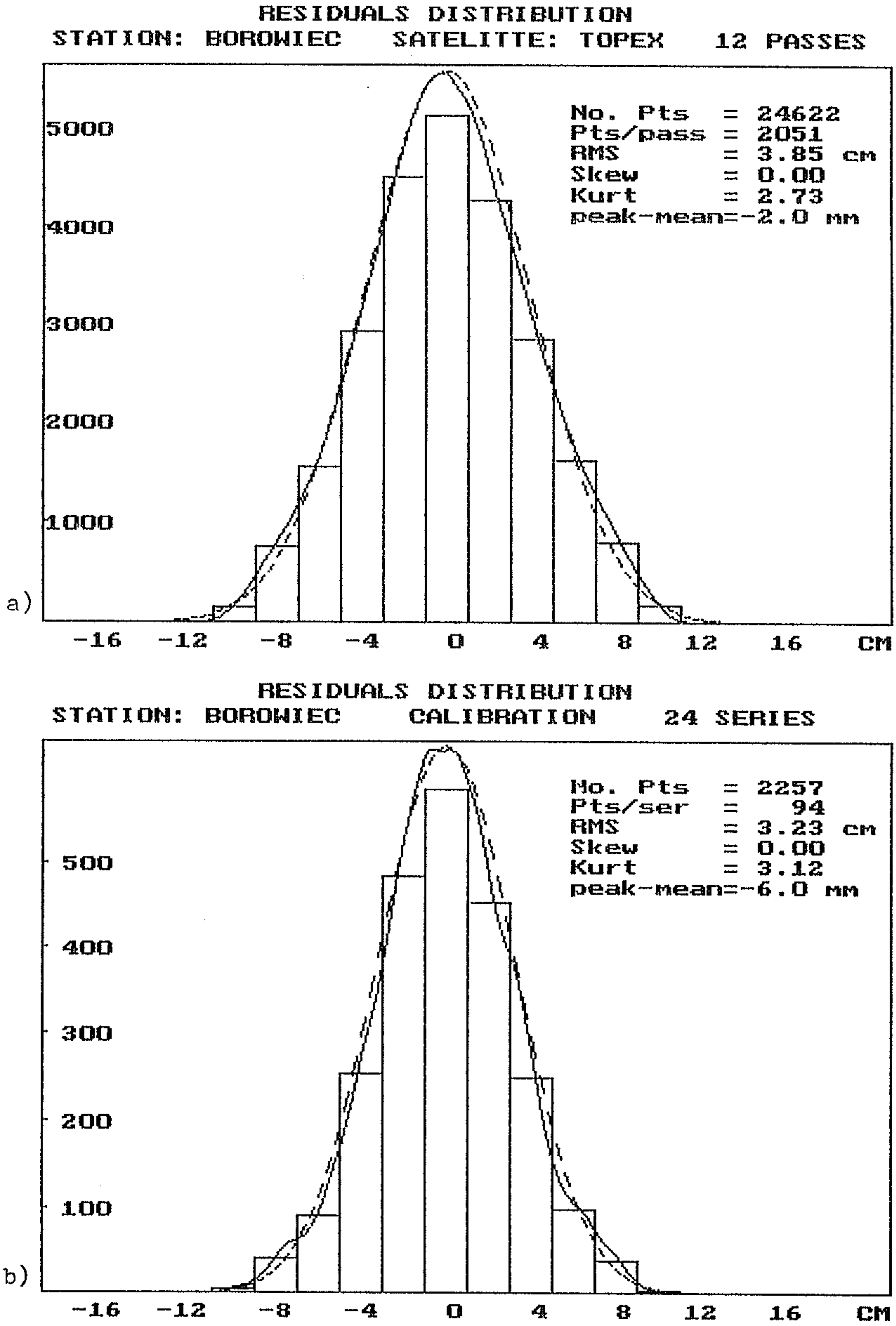
RESIDUALS DISTRIBUTION
STATION: BOROWIEC SATELITTE: TOPEX 12 PASSES
No. Pts = 24622
Pts/pass = 2051
RMS = 3.85 cm
Skew = 0.00
Kurt = 2.73
peak-mean=-2.0 mm
5000
4000
3000
2000
1000
a)
-16
-12
-8
-4
0
4
8
12
16
CM
RESIDUALS DISTRIBUTION
STATION: BOROWIEC CALIBRATION 24 SERIES
No. Pts = 2257
Pts/ser = 94
RMS = 3.23 cm
Skew = 0.00
Kurt = 3.12
peak-mean=-6.0 mm
500
400
300
200
100
b)
-16
-12
-8
-4
0
4
8
12
16
CM

Fig. 5

Preliminary Design of the Laser Reflector Array for the CHAMP Satellite

Reinhart Neubert
GeoForschungsZentrum Potsdam, Div.1: Kinematics and Dynamics of the Earth
Telegrafenberg A17, D-14473 Potsdam, Germany
Tel.: (49)-331-288-1153, Fax.: (49)-331-288-1111, e-mail: neub@gfz-potsdam.de

Introduction:

The CHAMP mission is dedicated to the study of the Earth's gravity field, magnetic and electric fields as well as for sounding of the atmosphere [10]. The high resolution accelerometer will give the unique possibility to measure the non-gravitational forces acting on the surface of the satellite. The result could be an accuracy improvement of the derived geoid undulations at about 1000 km wavelength by one order of magnitude compared to the present knowledge.
Main data source for the orbit determination will be an advanced space-born GPS receiver providing full global coverage. Laser ranging will be used as a supporting and independent data source for orbit determination. Its limitation is the rather poor global and temporal coverage but the SLR data are free from ambiguities and directly related to the terrestrial reference frame.
The CHAMP satellite (Fig.1) shall be launched in mid 1999 into a near circular polar (83°) orbit with 470 km altitude above ground. It is expected that the altitude will go down to 300 km after about 5 years and then decay very fast.

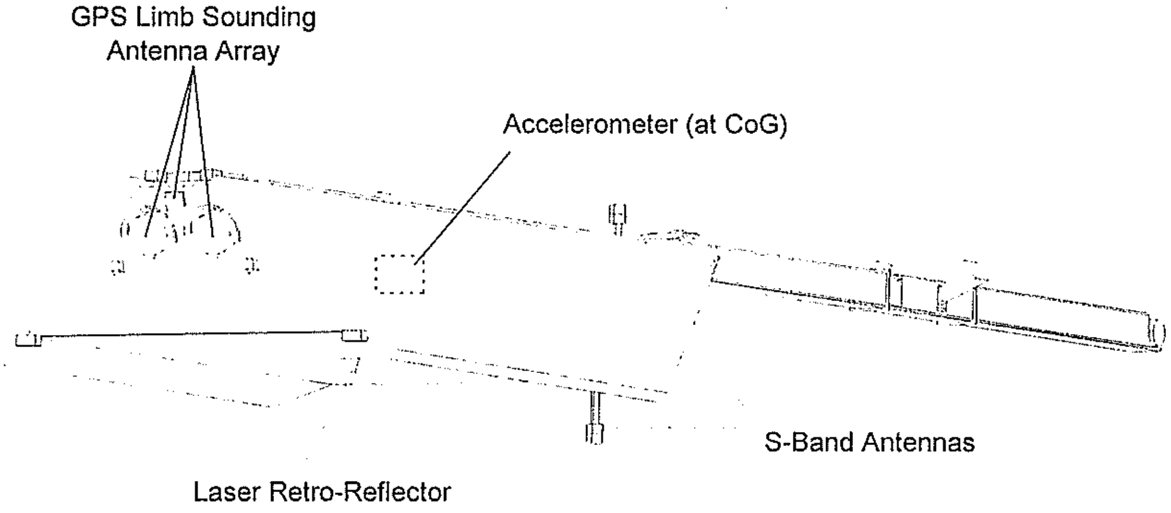

Fig.1 : Schematic drawing of the CHAMP satellite

Design philosophy of the reflector

The first requirement of the laser reflector is to enable the worldwide SLR station network to track the satellite with a resolution of about 1 cm. This can be fulfilled quite easily using a small array of standard design like the ERS-1 reflector for instance. Recent improvements of the SLR technology suggest to make the reflector suited for very high resolution ranging. Especially there is a lack of targets for demonstrating the power of the dispersion method (two-colour ranging).

An ideal target would be a single cube corner reflector but because of its limited angular field it is not well suited for very low orbiting satellites. An example of this type is the special purpose RIS reflector [5] on ADEOS. Another approach for spherical (rotating) satellites, proposed by Degnan [2], uses a high number of evenly distributed cube corners with a drastically reduced field of view. The first realization of this idea will be the WPLTN-1 satellite [8] with only one prism visible at any orientation. The drawback of this design is the strong fading: in about 50 per cent of the orientations the signal will be extremely weak or zero but this is tolerable for the goals of the WPLTN-1 project.

In the case of CHAMP we prefer a more simple and compact design similar to the concept of the GLRS-R reflector [6],[7]. It consists of four prisms only. This concept implies the use of the full unrestricted angular field of the cube corners to get sufficient coverage..

Estimation of the Ranging Performance

The following calculations of the performance parameters assume the use of standard quartz prisms with 19.1mm vertex and 45 degrees inclination of the front faces. The radial distance of the centers of the front faces of each prism from the symmetry axis of the array has been set to 33 mm.

The most interesting performance parameters are the variation of the signal strength and the location of the effective reflection plane (range correction). Special attention has to be paid to the influence of aberration and diffraction.

Basic relations

Signal Strength

The signal variation is mainly governed by the effective reflecting aperture, diffraction, the range and the atmospheric transmission. The dependence of the active reflecting aperture of a cube corner with circular front face can be approximated by a linear relation [3]. In addition the far field diffraction pattern is changing because the shape of the active area becomes more and more elliptical with increasing angle of incidence. If the station would be always in the centre of the far field, the combined effect can be approximated by the simple relation:

Eq.1
$$\mathrm{I}(\alpha) = \Big(1 \quad \frac{\alpha}{\alpha c} \Big)$$

where the cut-off angle αc is about 0.85 radians. Actually the station is not in the maximum of the far field in general because of velocity aberration. Nevertheless we are using the simple Eq.1 for this preliminary study. The real intensity can be weaker by as much as a factor of three to four. In addition we take the the R^{-4} dependence on range and the clear sky transmission [3] into account in the computation of the relative signal strength.

Range Correction

The range correction of the array refers to some reference point which can be defined arbitrarily.

We are using the intersection of the optical axes of the cube corners as a reference point. The reduction from this point to the centre of mass of the satellite can be done very precisely because of CHAMP's attitude stabilization. The range correction for a particular single prism to the reference point can be expressed by:

Eq.2
$$\Delta R = D\cdot\cos(\alpha) \quad L\cdot \; n^2 \quad \sin(\alpha)^2 \qquad\qquad \cos(\alpha) = (\underline{\mathbf{N}}\cdot\underline{\mathbf{C}})$$

where D is the distance from the reference point to the centre of the front face, α the angle of incidence, L the vertex length an n the refractive index. The angle of incidence can be obtained from the scalar product of the unit vectors **N** (normal to the front face) and **C** (line of sigth direction).

Velocity Aberration

The angular displacement vector of the returning beam due to aberration can be expressed by the vector relation (first order approximation):

$$\underline{\mathbf{ab}} = \frac{2 \cdot v}{c} \cdot \left(\underline{\mathbf{V}} - (\underline{\mathbf{V}} \cdot \underline{\mathbf{C}}) \cdot \underline{\mathbf{C}} \right)$$

Eq.3

In this formula **V** and **C** are unit vectors parallel to the satellite velocity and the laser beam, v and c the absolute values of the velocities. The aberration vector is coplanar with **V** and **C** and orthogonal to **C**.

The absolute value of the aberration is given by:

$$\left| \underline{\mathbf{ab}} \right| = \frac{2 \cdot v}{c} \cdot \sin(\delta) \qquad \cos(\delta) = (\underline{\mathbf{V}} \cdot \underline{\mathbf{C}})$$

Eq.4

It has been suggested that the aberration is smaller for a moving prism because of the Fizeau effect and will be zero for a special value of the refractive index [11]. Return energy measurements using specially designed reflectors seem to confirm this prediction [12]. However, the special relativity theory does not predict such an effect. This can be seen easily when using a reference frame moving with the satellite. In this system the usual optical formulas for refraction and reflection are applicable. But the incoming laser beam as well as the apparent position of the station are shifted. The refractive index of the prism has no influence on aberration within the frame of special relativity. To explain the strong returns observed in the Fizeau experiments one has to look for some other effect. Possibly atmospheric distortion is responsible.

To be on the safe side, we decided to take the classical aberration into account in the case of the GFZ-1 satellite and for CHAMP as well.

Results

Let us first get an overview of the angular fields of the individual cube corners using Fig.2.

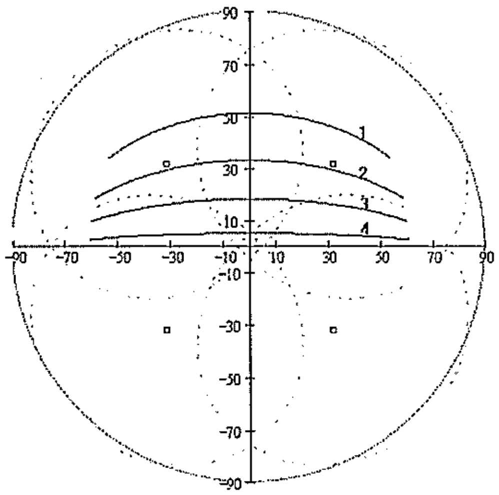

Fig.2: Polar plot of the angular fields of the cube corners.

Origin: Nadir direction.

Radial : Angle between Nadir and line of sight

Peripheral: Azimuth of line of sight (no scale printed)

Angular positions of the cube corner optical axes are indicated by small boxes

Dotted curves surrounding the boxes: loci of the cut-off

Curves 1 to 4 : Angular tracks of the laser beam direction for passes with a culmination elevation of 32.4°, 53.7°, 70.0° and 84.5°, respectively.

The velocity vector is directed from left to right

From Fig.2 it can be seen that there is some overlap but regions where only one prism is contributing are existing as well.

For the visualization of the performance characteristics we use two representations:

a) mapping the parameters over the relative location between the station and the sub-satellite point
b) plotting the time dependence of the relevant parameters assuming circular orbits of different culmination elevation

Signal Strength

Fig.3 a,b are examples of the first representation. In these graphs the following coordinate system is used: Let the z-axis be directed from the geocentre to the satellite, the x-axis from the geocentre parallel to the satellite velocity and the y-axis orthogonal to both. Let the station coordinates vary on a spherical Earth. The coordinates x and y of the station are now used as the independent variables in Fig.5. That means that the origin corresponds to the sub-satellite point and x and y are the orthogonal distances of the station from the line geocentre to the satellite.

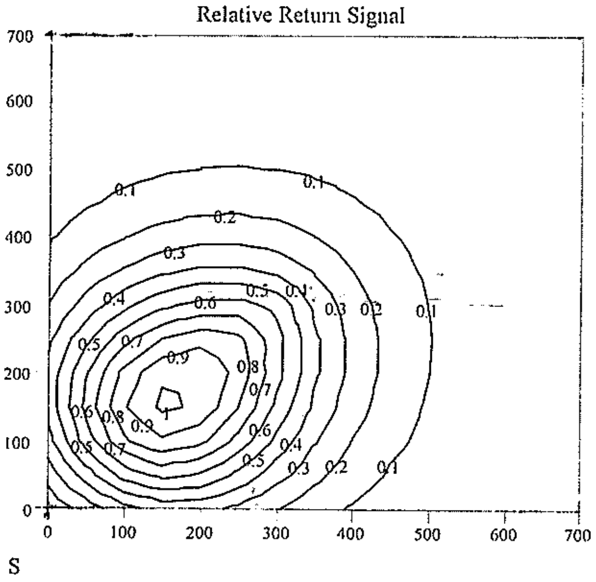

Fig. 3a: Relative signal strength over the station position . Origin: Sub-satellite poin
The scale is in km

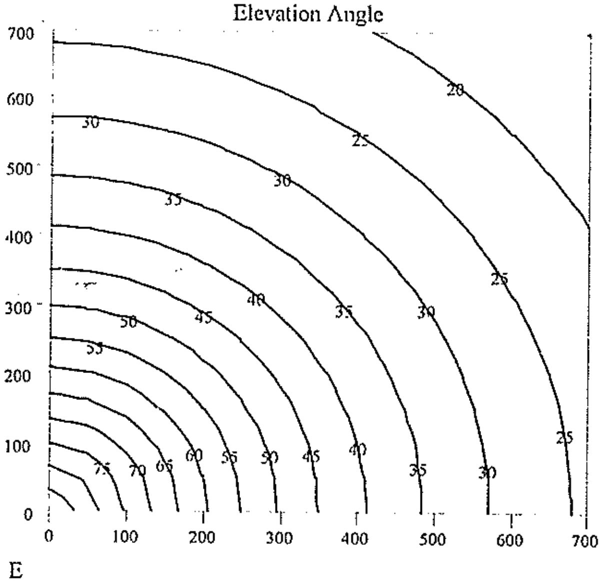

Fig.3b: Elevation angle over the relative station position.

Fig.3a is a map of the relative signal of one prism. Only one quadrant is represented to avoid confusion .

Fig.3b maps the elevation angle in the same representation to enable cross-reference to this quantity.

In the following Fig.4 a..d we plot the relative signal versus time of all the individual cube corners. From these plots it can be seen that for more than 50 per cent of the total observation time one prism is responding only. Strong crosstalk between the reflectors are observed at very high elevation passes.

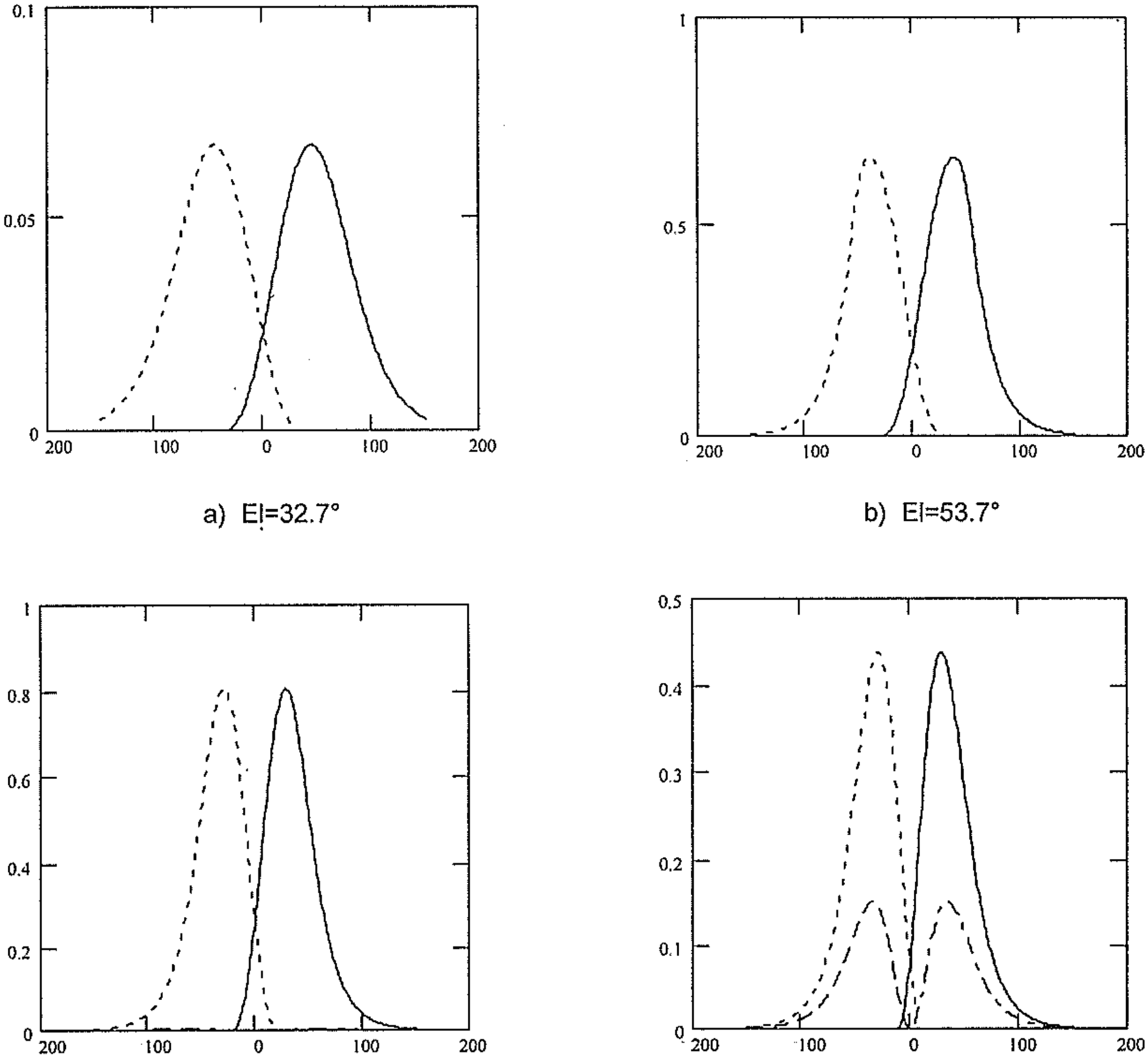

a) El=32.7°

b) El=53.7°

c) El=70.0°

d) El=84.5°

Fig.4 a...d: Signal strength versus time for passes with different elevation at culmination. Time scale is in seconds. The vertical scale is relative to the expected signal of GFZ-1 for 54° elevation.

Range Correction

The range correction for each prism can be easily obtained from Eq.2. If more than one prism is contributing, the weighted mean can be used as the range correction. This definition is correct for a single photon system working at very low signal level. The majority of observations will be single prism responses however. In this case the range correction does not depend on the receiving system, provided that the calibration is done at the same signal level as the satellite returns, or the ranges are properly corrected for signal level.

In Fig.5 we plot the mean range correction versus time for the 4 test orbits. As can be seen, the range correction is very weakly dependent from the orientation except for near culmination. This is not a source of error because the orientation of the satellite and, therefore, the actual range correction are known at any time. If the model error of the orbit exceeds 10 mm, then the range correction can be replaced by a constant value of about 15 mm.

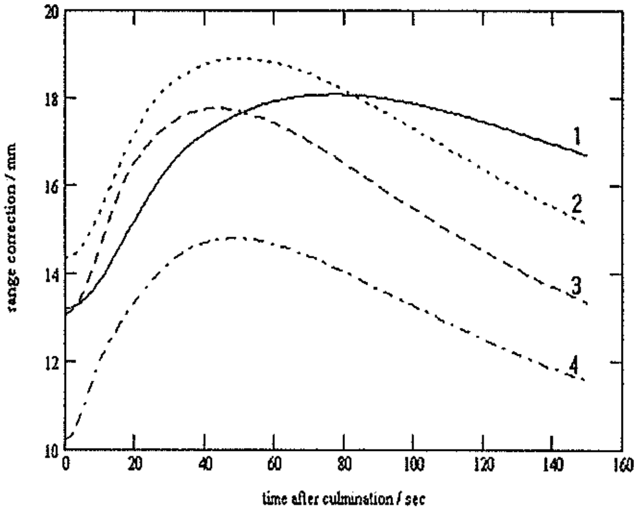

Fig.5: Effective range correction versus time for circular passes
time scale: sec; vertical scale: mm
The tracks 1 to 4 correspond to the elevations at culmination of 32.7°, 53.7°, 70.0° and 84.5°, resp.

The effective range correction is the weighted mean of the single cube values. It differs from the single cube correction near culminatation or for high elevation passes (>70°).

Aberration and Diffraction

Although the orbital velocity is constant for a circular orbit, the aberration vector varies both in its orientation and length. This is represented in Fig.6. It can be seen that there is a transversal component except when the station is on the x-axis (zenith pass) or on the y-axis (culmination). The simplest way to match the reflector to this situation is to use a small offset of one of the dihedral angles of each prism. The result is a two-spot far field diffraction pattern. The splitting must be adjusted in such a way, that one of the lobes is approximately directed to the apparent place of the station.

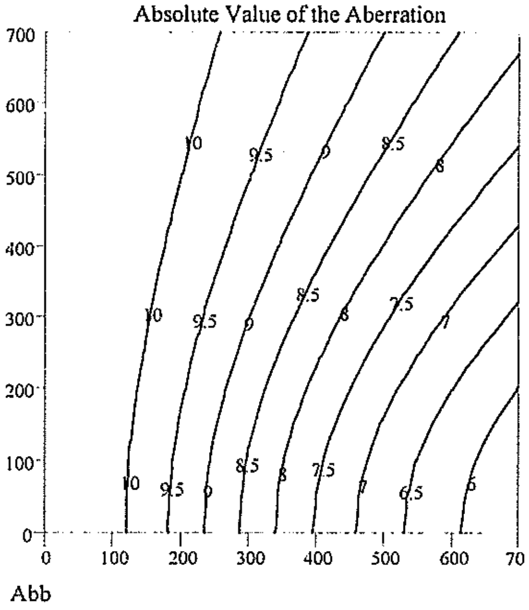

Fig.6a: Absolute value of the aberration vector over the relative station position

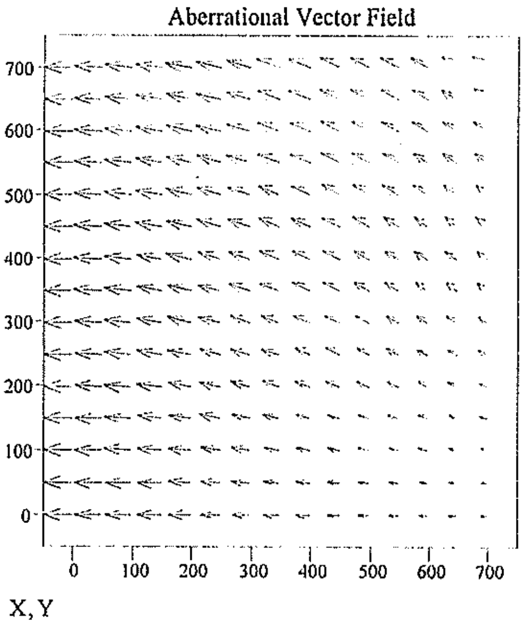

Fig.6b: Projection of the aberration vectors onto the x-y-plane

Because of the varying aberration the two lobes must have a certain width. Small prisms have a sufficient natural width of the far field because of diffraction. If necessary, a small spherical distortion can be added to optimize the field. Full optimization has to consider the dependence of the far field from orientation [4]. Most pronounced changes of the pattern occur when both lobes overlap. In this case the maximum tends to be in the centre as can be seen in Fig 7 for a 28° rotation in the plane of the spots. Similar patterns have been observed experimentally by Burmistov et al. [9].

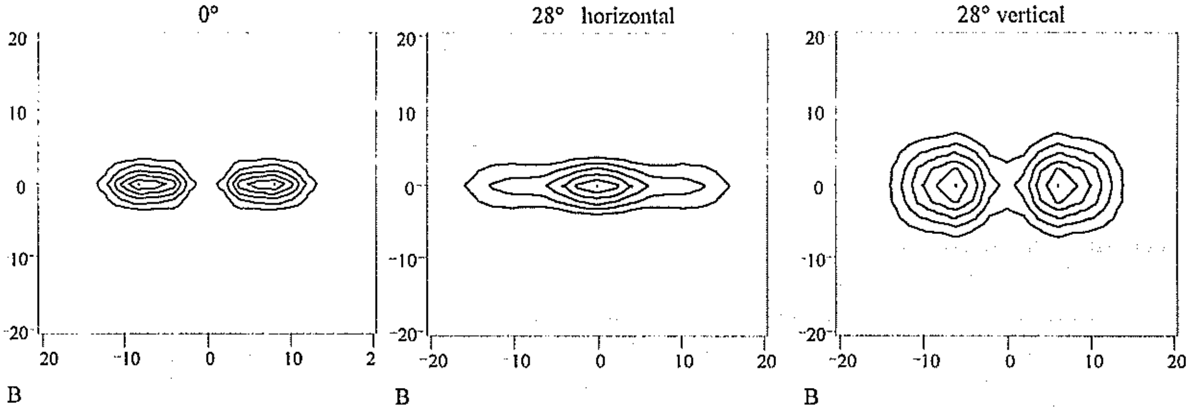

Fig.7: Computed far field patterns for normal incidence and inclined by 28° in two orthogonal directions The geometrical splitting of the lobes at normal incidence has been set to 16". The lowest level contour lines correspond to 17% of the maximum.

References:

[1] D.A.Arnold: Method of Calculating Retroreflector-Array Transfer Functions, Smithsonian Astrophysical Observatory Special Report No. 382 (1978)
[2] J.J.Degnan: Millimeter Accuracy Satellites for Two- Colour Ranging Proc. 8th Workshop on Laser Ranging Instr., Annapolis, p.7-36....7-51 (1992)
[3] J.J.Degnan: Millimeter Accuracy Satellite Laser Ranging: A Review Geodynamics Series Volume 25: Contribution of Space Geodesy to Geodynamics: Technology, p.133-162, 1993
[4] A.Minato, N.Sugimoto, Y.Sasano: Optical Design of Cube Corner Retroreflectors Having Curved Mirror Surfaces, Appl. Opt. Vol.31, No.28, p.6015-6020, (1992)
[5] N.Sugimoto, A.Minato: Optical Characteristics of the Retroreflector in Space for the Advanced Earth Observing Satellite, Optical Review, Vol.3, No.2, p.62-64 (1996)
[6] G.Lund: New Perspectives for High Accuracy SLR with Second Generation Geodesic Satellites Proc. 8th Workshop on Laser Ranging Instr., Anapolis, p.7-56....7-64, (1992)
[7] G.Lund: GLRS-R 2-Colour Retroreflector Target Design and Predicted Performance Proc. 8th Workshop on Laser Ranging Instr., Anapolis, p.13-17....13-32 (1992)
[8] B.Greene, V.Shargorodsky, M.Fujita, H.Kunimori: A New Generation of Satellite for Sub-Millimeter Ranging, these Proceedings
[9] V.Burmistov, V.Shargorodsky, V.Vasiliev, N.Soyuzova: Study of Retroreflectors with Two-Spot Reflection Pattern at Sloped Light Incidence, these Proceddings
[10] Ch.Reigber, R.Bock, Ch.Förste, L.Grunwaldt, N.Jakowski, H.Lühr, P.Schwintzer, C.Tilgner: CHAMP Phase B, Executive Summary, GFZ Scientific Technical Reports STR96/13, (Nov. 1996)
[11] V.Vasiliev, V.Grishmanovskij, L.Pliev, T.Startsev: Effect of Motion of the Optical Medium in Optical Location, JETP Lett., Vol.55, No.6, March 1992, p.316-320
[12] V.Vasiliev, L.Gusev, J.J.Degnan, V.Shargorodsky: Experimental Verification of the Fizeau Effect Influence on the Reflected Beam Direction in Satellite Laser Ranging, Proc. 10th Workshop on Laser Ranging Instr., Canberra, Nov. 7-11, 1994, p.147-157

DEPENDENCE OF AJISAI'S CENTER-OF-MASS CORRECTION ON LASER RANGING SYSTEM

TOSHIMICHI OTSUBO *(otsubo@crl.go.jp)*,
JUN AMAGAI AND HIROO KUNIMORI

COMMUNICATIONS RESEARCH LABORATORY / TOKYO
4-2-1 NUKUI-KITA, KOGANEI, TOKYO, 184 JAPAN

1. Introduction

The size of geodetic satellites has become one of the limiting factors in laser ranging precision, and it is called the "satellite signature" effect. In this paper, we focus on the satellite signature of the Japanese geodetic satellite "Ajisai" and its center-of-mass correction values. Ajisai was launched in 1986 and it is still one of the most frequently tracked satellites according to a NASA CDDIS data summary.

The value of 101 cm for a 200 ps pulse width laser in the pre-launch analysis (Sasaki, 1987) has been the only standard for its center-of-mass correction, even though various laser ranging systems are currently in operation and their performance has improved considerably. According to Sinclair (1995), the Lageos' center-of-mass correction for the single-photon system differs several millimeters from its standard value. The bigger Ajisai is considered to be more dependent on laser ranging systems.

In this paper, the return pulse shape from the Ajisai is simulated and Ajisai's center-of-mass values are determined for several system configurations. The range biases for multi-photon stations and single-photon stations are then estimated by an orbital analysis.

2. Simulation of return pulse shape

The specifications of the Japanese geodetic satellite Ajisai are listed in Table 1 and its external appearance is shown in Figure 1. Most of its surface is covered by mirrors to reflect sunlight, and the sets of corner-cube reflectors (CCR) are scattered sparsely between the mirrors. Therefore, the return pulse shape varies significantly according to the laser incident angle to Ajisai.

We can evaluate the satellite signature effect of Ajisai only by a computer simulation since Ajisai is already orbiting in space. In this section, the return pulse for each incident angle is simulated.

However, when we start simulating the return pulse from Ajisai using a detailed specification, two critical problems are found:

(1) All CCRs are installed so that its front face is located at 1.053 m from the center-of-mass with a tolerance of 5 mm.

(2) The angles between CCR faces have an error of about 2 arcseconds.

It is difficult to discuss the signature effect at 1 mm or better because of limitation (1). Calculation of the far field diffraction pattern would be meaningless with an error as large as (2). However, even if each simulated return pulse does not model the real one because of these limitations above, the statistical behavior is considered to follow our simulation. In this study, it is therefore assumed that the installation was done with no error and that the far field diffraction pattern is simple.

The CCR installed on Ajisai is shown in Figure 2. Let us consider the strength of the return pulse reflected by CCR here. The back face is not coated, and the reflectance of CCR is dependent on the azimuth angle especially when the incident angle is wide (Figure 3). (In the pre-launch analysis, the reflectance is uniformly treated as zero when the incident angle > 17 deg, which is corrected in this study.) Each vertex of the front face is cut as long as 8.5 mm, which makes the calculation of the effective reflection area complex (Figure 4). Although we gave up modeling the far field diffraction pattern, the diffracted area is spread in inverse proportion to the effective reflection area of

Launch	August 12, 1986 by NASDA
COSPER ID	8606101
Diameter	2.15 m
Mass	685 km
Number of CCRs	1436 (120 sets)
Optical index of CCR	1.46 (fused silica)
Number of mirrors	318
Orbit altitude	1485 km
Orbit inclination	50.01 deg.

Table 1. Specifications of Ajisai.

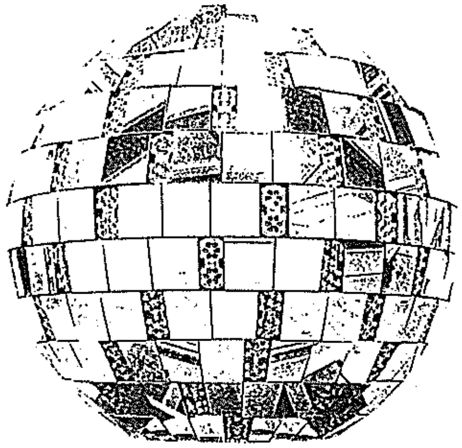

Figure 1. Outlook of Ajisai.

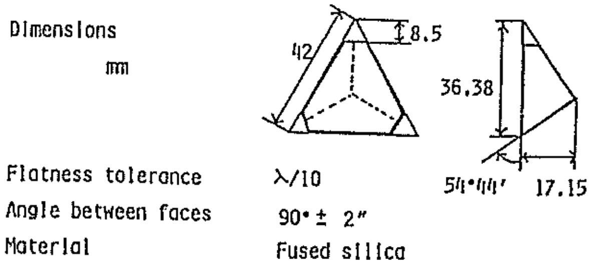

Figure 2. Ajisai's corner cube reflector.

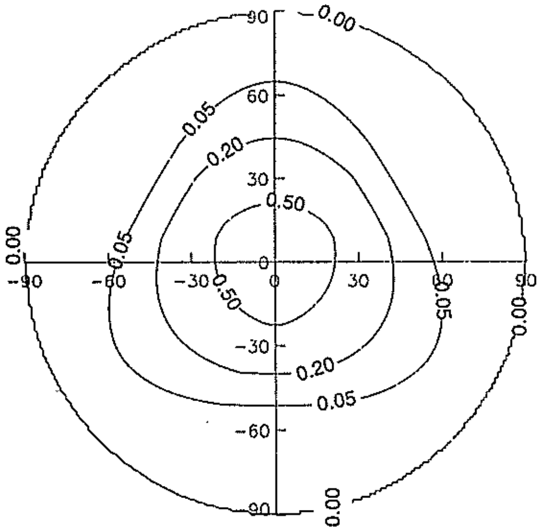

Figure 3. Effective reflection area of Ajisai CCR. (Area of the front face without vertex cut is 1.)

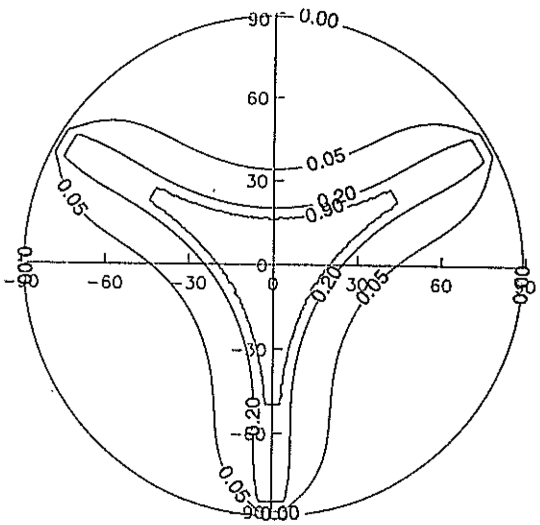

Figure 4. Reflectance of Ajisai CCR. It is calculated as the product of double refraction at the front face and triple reflection at the back face.

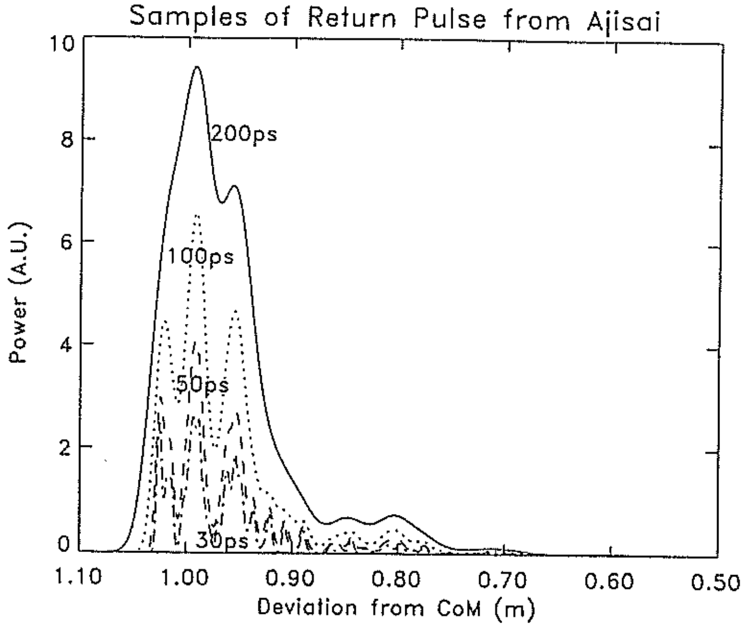

Figure 5. A sample of return pulse shape from Ajisai (Latitude=+13.5 deg and Longitude=-19.5 deg in Ajisai reference frame).

CCR. The return strength is hence in proportion to the effective reflection area for the diffraction effect. Then the relative return pulse strength for a CCR is given as:

$$(\textit{strength}) \propto (\textit{effective reflection area})^2 \times (\textit{reflectance}).$$

A return pulse shape from Ajisai is given as a simple sum of the contribution from each CCR as the diffraction pattern is neglected here. When an incident angle for Ajisai is taken, the delay and the return intensity for each CCR are calculated and the contribution of each is totaled.

We generate return pulse shapes taking 10267 incident angles equally around Ajisai with the interval of about 2 degrees. The incident laser pulses are assumed to be a Gaussian distribution with pulse widths (FWHM) of 200 ps, 100 ps, 50 ps and 30 ps. A sample is shown in Figure 5; the return pulse ranges more than 40 cm, the deformation of the pulse is simple for a 200 ps laser, but complex for a 50 ps and 30 ps laser with many peaks.

3. Center-of-mass corrections

3.1. Multi-photon System

Most laser ranging stations are now operated as the return echo is detected as a pulse, i.e., at a multi-photon level. The combination of a micro-channel plate photomultiplier (MCP) and a constant fraction type discriminator (CFD) is popularly used in current laser ranging stations. In this study, both the MCP and the CFD are assumed to work ideally.

The center-of-mass correction for this multi-photon system is calculated here. Figure 6 is a sample of the dependence on the incident angle, taking a laser pulse width of 100 ps; (a) and (b) are graphs for Ajisai's upper hemisphere and lower hemisphere. The center-of-mass correction varies about 3 cm from peak to peak. The vague pattern of the 120-degree azimuth interval in Figure 6 is caused by the arrangement of sunlight reflection mirrors; that is, three mirrors in each row are identical.

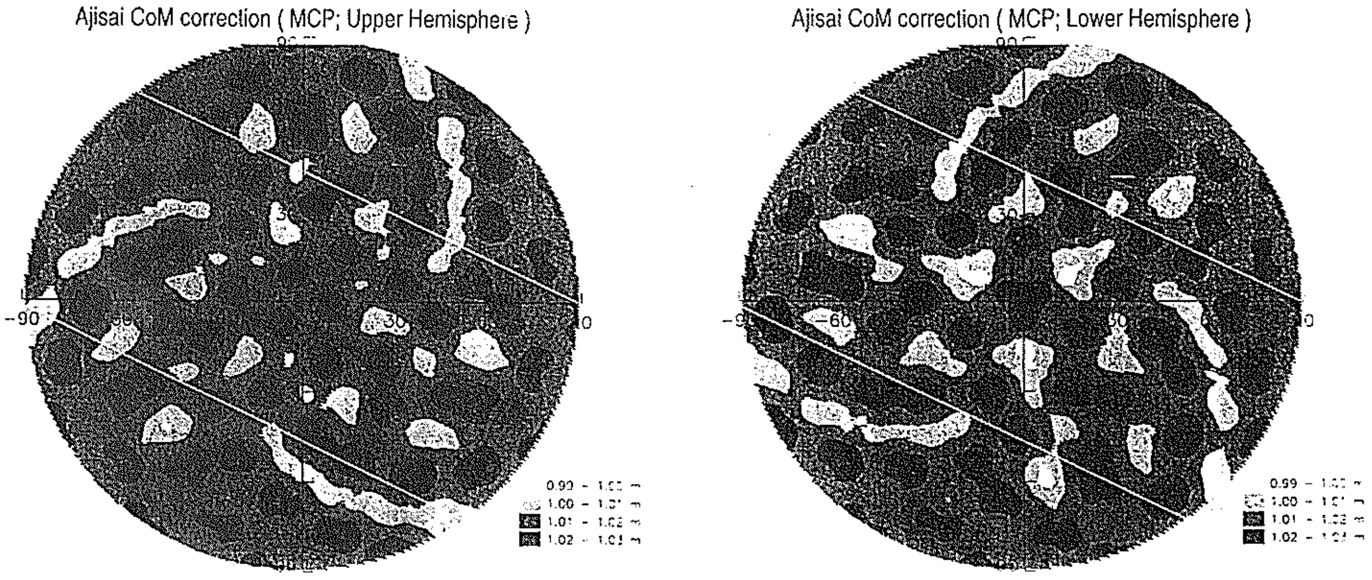

(a) upper hemisphere

(b) lower hemisphere

Figure 6. Ajisai's center-of-mass correction for a multi-photon system with respect to the incident angle.

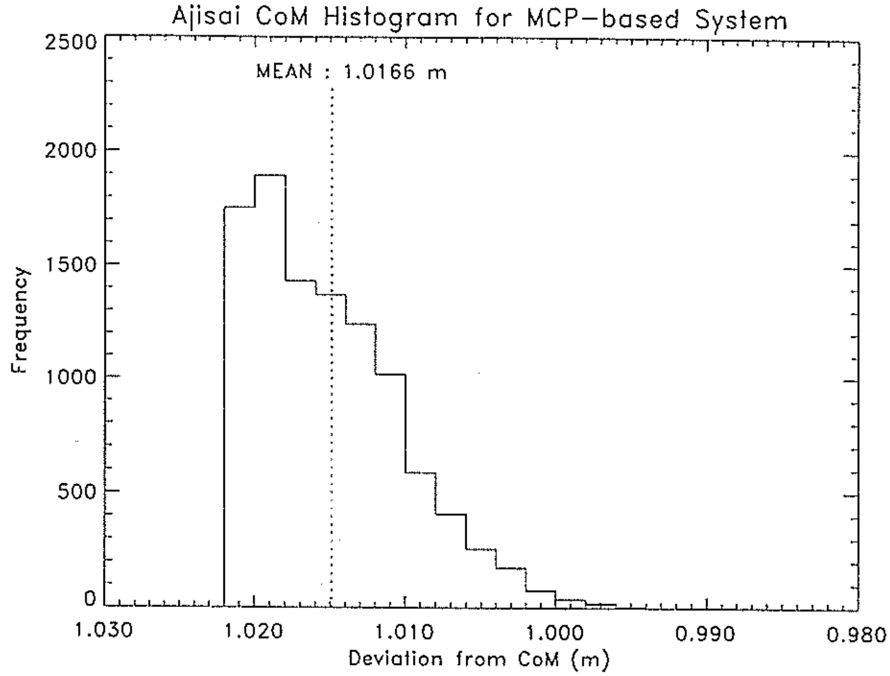

Figure 7. A histogram of Ajisai's center-of-mass correction for a multi-photon system (100 ps laser pulse width).

A histogram of the center-of-mass correction values for 10267 incident angles is plotted in Figure 7 for a 100 ps laser. It represents the distribution of full-rate data residuals under the condition that Ajisai is shot adequately and uniformly from every direction, and that the tracking operation is done with no systematic error. In other words, the rms of the full-rate data residuals cannot be better than that of Figure 7; 5.4 mm for a 100 ps laser. The results for 200 ps -- 30 ps pulse widths are listed in Table 2. The pre-launch value, 1.01 m, which was derived for a 200 ps laser, agrees well with our result for a 200 ps laser, 1.0103 m, although the effective digit of the pre-launch value is not clear. The shorter the laser pulse width is, the longer the center-of-mass correction becomes. We must take notice of its dependence on the laser pulse width since it might cause cm-level bias because of the system configuration.

Laser pulse width (FWHM)	Center-of-mass correction and rms (m)
200 ps	1.0103 (0.0060)
100 ps	1.0166 (0.0054)
50 ps	1.0199 (0.0049)
30 ps	1.0211 (0.0047)

Table 2. Ajisai's center-of-mass correction for a multi-photon system with respect to the laser pulse width.

We should comment that the MCP response time or any jitters also limit the laser ranging precision, and its behavior in the leading edge becomes important if the laser pulse width is sufficiently shorter than it. Hence the value for the

30 ps laser in Table 2 might not be realistic in current stations even if such a short pulse laser is available.

3.2. Single-photon System

Several stations have adopted a single-photon avalanche diode (SPAD) recently (ex. Herstmonceux, Graz, Wettzell, Orroral, Riyadh, Tokyo) and it seems Herstmonceux is now the only station which regularly uses a SPAD for Ajisai ranging at the single-photon level.

The return epoch cannot be determined for each shot, but its statistical behavior can be estimated. The return pulse shape like Figure 5 is the probability distribution for the SPAD system as long as the signal strength is kept at a single-photon level. It is of no use to examine each return pulse shape, but the residual distribution will follow the "average" pulse shape (Figure 8) if the data amount is sufficient. Figure 8 is a sum of the 10267 simulated pulse shapes for incident laser pulses, at 200 ps -- 30 ps. It should be emphasized that the mean is almost a constant --- 0.9712 m, independent of laser pulse width.

Because the distribution in Figure 8 is apparently larger than the current system noise and because it is skewed, the pre-processing procedure will reject a certain part of the distribution tail. The data clipping method is currently different from station to station but most of them adopt a Gaussian fitting with 2 -- 3 x rms clipping criteria. We repeat 2.0, 2.5 and 3.0 x rms clipping and determine its

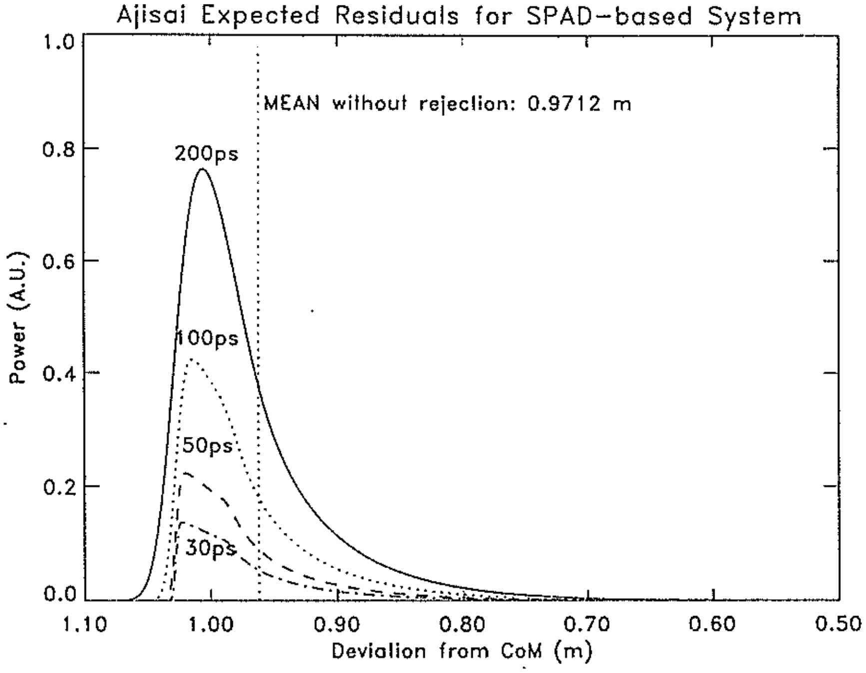

Figure 8. Ajisai's residual distribution for an ideal single-photon system.

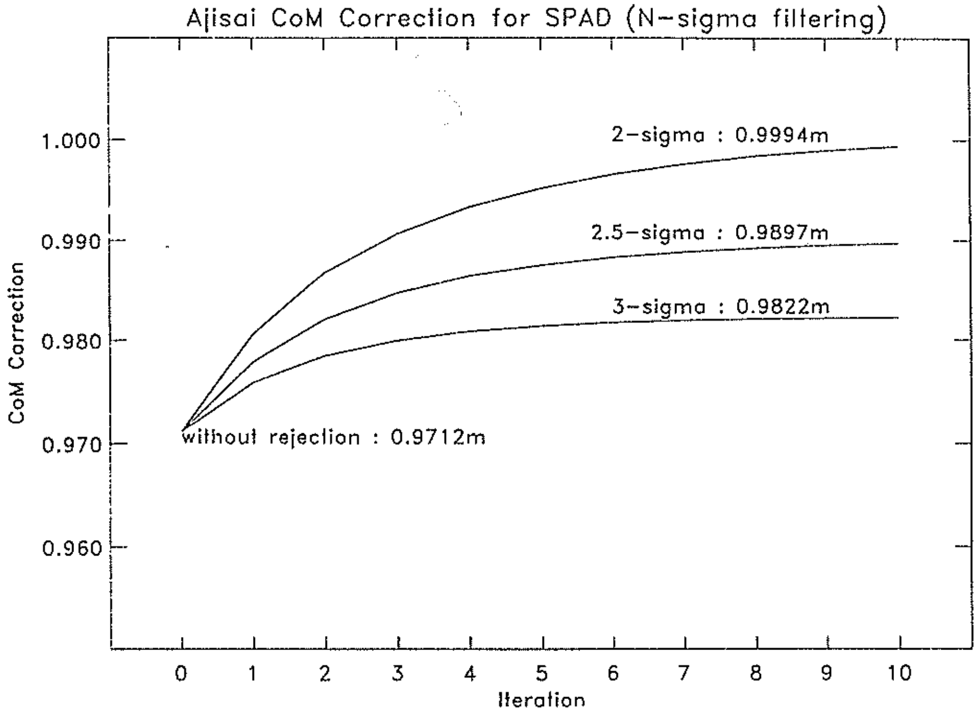

Figure 9. Shift of Ajisai's center-of-mass correction for a single-photon system with respect to the noise rejection criteria.

convergence value (Figure 9). A bias of about 2 cm would appear between a 2.0 x rms clipping and 3.0 x rms according to the graph. Ajisai's center-of-mass correction for single-photon detection is robust with respect to the incident laser pulse width, but sensitive on the noise rejection procedure.

4. Range bias estimation – preliminary results

Using the laser ranging data analysis software CONCERTO (Otsubo, 1994), a series of short-arc analysis was performed between September 1995 and August 1996. The on-site normal point data set is taken from the NASA CDDIS QL directory, and the standard value 1.01 m is used as Ajisai's center-of-mass correction. The station coordinates and the range bias are estimated every 15 days whereas the orbital elements and force coefficients (C_R and C_D) are estimated every day.

The range bias for a multi-photon system with a 100 ps laser should be -6.6 mm and that for a single-photon system with a 3 x rms clipping should be +27.8 mm, according to the discussion in the previous section.

The estimated range biases are plotted in Figure 10 (a) and (b). A sample of multi-photon system, Quincy 7109, is shown in figure (a) and that of Herstmonceux 7840 representing a single-photon system is given in (b). The range bias of Quincy scatters around zero, so the standard value

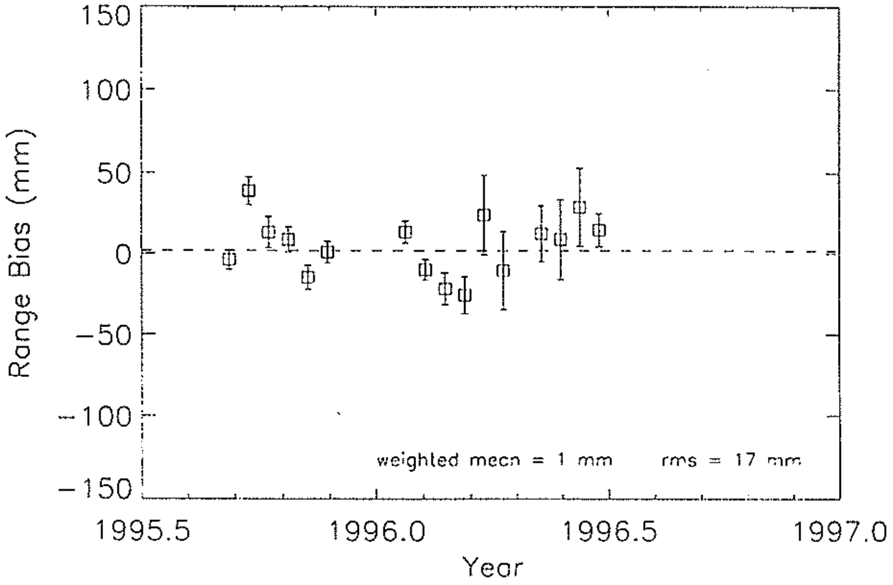

(a) Quincy 7109

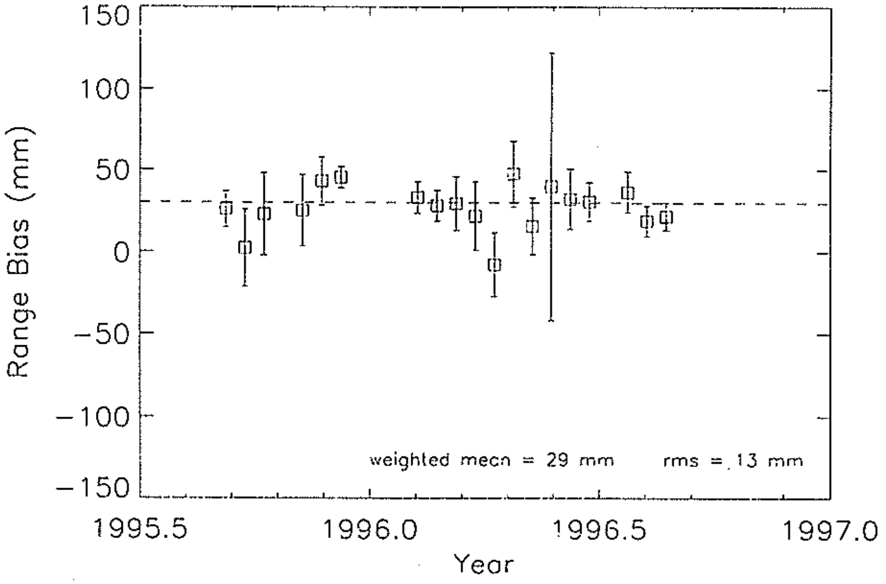

(b) Herstmonceux 7840

Figure 10. The Ajisai's range bias estimated by CONCERTO.

1.01 m seems appropriate. On the other hand, the mean of Herstmonceux's range bias is +29 mm agreeing well with our model.

We cannot conclude yet that the system dependence of center-of-mass correction is detected from orbital analysis. This is firstly because the range bias results above are not separated from the system bias, and secondly because the data set is preliminary without the error correction (such as that listed in DATA BITS AND BYTES in "CDDIS BULLETIN").

5. Conclusion

Ajisai's center-of-mass correction should be treated as a *variable* not a constant. To determine the value accurately, we must take account of

☐ The laser pulse width and the timing response of detector (for a multi-photon system)

☐ The data clipping criteria (for a single-photon system)

for each laser ranging station. The correction values are derived with the following new viewpoints compared to the pre-launch analysis:

☐ The azimuth angle dependence of each CCR's reflectance is considered.

☐ Short pulse width lasers are extended up to 30 ps.

☐ Single-photon system is modeled with a variety of noise rejection criteria.

The range bias estimation of Ajisai is promising for detecting the system dependence of its center-of-mass correction.

In future work, the relation between the center-of-mass correction and Ajisai's spin motion will be researched. The simultaneous detection by an MCP and a SPAD will help our research. The study here can also be applied to smaller satellites.

Acknowledgment

We would like to thank Mr. H. Hashimoto, National Space Development Agency of Japan, and Mr. A. Sengoku, Hydrographic Department of Japan, for the supply of Ajisai specification data and a many stimulating discussions. We would also like to thank Dr. G. M. Appleby, Royal Greenwich Observatory, UK, and Dr. Georg Kirchner, Institut fuer Weltraumforshung Austria and Mr. A. Willing, AUSLIG, Australia for the information on the SPAD ranging configuration at Herstmonceux, Graz and Orroral, respectively.

References

G. M. Appleby, P. Gibbs, "Monitoring potential range biases in single-photon SLR systems," Proceedings of 9th International Workshop on Laser Ranging Instumentation, 1, 92-102, 1994.

G. M. Appleby, "Centre of mass corrections for Lageos and Etalon for single-photon ranging systems," Proceedings of Annual EUROLAS meeting, 18-26, 1995.

P. O. Minott, T. W. Zagwodzki, T. Varghese, M. Seldon, "Prelaunch optical characterization of the Laser Geodynamic Satellite (LAGEOS 2)," NASA Technical Paper, 3400, 1993.

R. Neubert, "An analytical model of satellite signature effects," Proceedings of 9th International Workshop on Laser Ranging Instumentation, 1, 82-91, 1994.

T. Otsubo, H. Kunimori, B. Engelkemier, F. Takahashi, "Error control of numerical integration in SLR analysis software CONCERTO," Journal of Geodetic society of Japan, 40, 4, 347-355, 1994.

M. Sasaki, H. Hashimoto, "Launch and observation program of the experimental geodetic satellite of Japan," IEEE Tranactions on Geoscience and Remote Sensing, 25, 5, 526-533, 1987.

A. T. Sinclair, R. Neubert, G. M. Appleby, "The Lageos centre of mass correction for different detection techniques," Proceedings of Annual EUROLAS meeting, 31-36, 1995.

Remote Sensing of Atmospheric Parameters

Ulrich Schreiber, Birgit Bardorf, Stefan Riepl
Forschungseinrichtung Satellitengeodäsie
Fundamentalstation Wettzell
D - 93444 Kötzting
Germany

Karl Heinz Haufe
Institut für Angewandte Geodäsie
Fundamentalstation Wettzell
D-93444 Kötzting
Germany

Abstract

A model for the refractive index of the atmosphere along the line of sight is used [1] to reduce the measurements to real ranges. However, these corrections are based on model assumptions dependent on values for pressure, temperature and humidity, taken on the ground in the vicinity of the ranging station. From dispersion measurements of the atmosphere by simultaneous dualcolor ranging some evidence for small model errors was found [2]. It is assumed, that these errors arise from inadequate modelling of the water vapor content. This content is measured by a meteorological sensor close to the ground and might not be representative for the lower troposphere around the station. Meteorological temperature inversion effects are also not properly been accounted for. Remote sensing techniques promise to fill a gap. Instantaneous profiles of the water vapor content in the troposphere in the vicinity of the tracking stations can be obtained using Raman scattering from the water vapor. This paper reports the technology employed and the results obtained.

1. INTRODUCTION

Laser Ranging in general can be considered as a special form of a lidar application. One would like to use the existing backscattered light from the ranging laser pulse for the determination of the atmospheric parameter of interest. Since water vapor was identified as being the important parameter to determine [2], a profile of the water vapor content of up to 5 km around the tracking station could ultimately allow the model of refraction correction to be refined by replacing profile assumptions with real data. A Raman scattering experiment [3] serves this purpose. The outgoing laser pulse of $\lambda = 532nm$ interacts elasically, as well as inelastically with the water vapor in the atmosphere. The Raman shifted echo then can be detected at the wavelength $\lambda = 660nm$. The amplitude and shape of the detected lidar echo reflects the amount and distribution of the water contained in the atmosphere. A Raman lidar presents a few specific experimental difficulties which need to be overcome.

- The Raman echo is very weak, therefore it needs a very sensitive detection scheme. This is not unlike the LLR application
- The elastic backscattered Rayleigh- and Mie- signal is theoretically between 4 and 8 orders of magnitude higher. This requires efficient optical blocking of the laser frequency at the detection unit of the lidar experiment.

Laser ranging in general is a very demanding technology, operating on extremely low signal levels depending on the distance and structure of the target. Any additional experiment hooked to the existing setup therefore must not interfere with the primary ranging task. Since there was no extra funding for this experiment, the setup described had to be fitted to the existing instrumentation and is far from optimal.

2. THE LIDAR EXPERIMENT USING SINGLE STOP DETECTION

The telescope of the WLRS [4, 5] has a guiding station, which assists tracking mainly during the lunar ranging application. This guiding station uses the same telescope as the ranging equipment. The light which is guided from the telescope to the receiver passes through an interference filter. The laser frequency is reflected towards the ranging detector, while the other spectral components pass through this filter and enter the guiding station. Since the Raman shifted backscattered laser echo lies within the passband of the interference filter, the detector for the lidar experiment must go to the guiding station during the Raman experiments. A narrowband spectral filter together with an edge filter was used to ensure total blocking of the elastic backscatter components, the attenuation being more than 9 orders of magnitudes. The complete setup was discussed in detail in [4], however Figure 1 shows the block diagram of the electronic part. An avalanche diode detected the firing of the laser on the optical bench and started a Time Interval Counter. A delay generator switched an avalanche photodiode into the geiger mode after the laser pulse left the telescope. Any backscattered Raman shifted photon causing a breakdown in the detector stops the Counter again. From the time elapsed one can take the distance of the scatterer, before the measurement is repeated on the next shot of the laser 100 ms later. The advantage of this technique is the fact, that the full sensitivity of avalanche photodiodes can be used. However a drawback is the slow repetition rate for this statistical approach, due to limitations in the laser and the high dark count rate caused by the intrinsic noise of silicon avalanche photodiodes. Cooling this device down to $-32^{o}C$ helps, but does not eliminate the problem. Lidar experiments were carried out for both Rayleigh and Raman scattering, in order to analyse the properties of this experimental setup. Figure 2 summarises this work. The plot of countrates versus range in the Rayleigh scattered case should be at least 4 orders of magnitude greater than in the Raman scattered case. For reasons that are still unknown, it was found that the elastic scattering experiment was roughly 4 orders of magnitude weaker than expected. This does not seem to be a general property of the experimental setup, since the inelastic scattering case yielded the expected results. It is interesting to note that the count rate increases for long ranges in this experiment. This was attributed to a high concentration of water vapor in a higher layer of the atmosphere, because clouds formed rapidly, shortly after the measurement. A general drawback of this approach is the fact that a measurement, integrating over 10 000 shots, takes roughly 15 minutes to be carried out. This is to long to be of practical value.

3. THE LIDAR EXPERIMENT USING MULTI STOP DETECTION

In order to increase the data yield, the setup was modified so that the avalanche diode was gated on and off rapidly. A direct negative consequence is in addition to the thermally induced noise counts, the contribution coming from afterpulsing of the detector. On the other hand more than one echo can be collected per laser shot. When an avalanche process occurs, it is passively quenched due to the design of the driving circuit. However it still takes time for the electrons to disappear from the avalanche region. If the gate is switched on before all carriers have left this avalanche regime, another breakdown is generated. Since this additional source for noise counts must be avoided, the recovery time of the avalanche diode was estimated experimentally. A comparatively short gate of $1\mu s$ and a off- time of the same duration were a good compromise. The short gate keeps the thermally induced dark count rate low, while $1\mu s$ is just enough for the diode to quench properly and avoid afterpulsing. Time Interval Counters are not suitable for this multigate application. Since exact timing is not an issue in lidar applications, the following approach has been chosen. Every 250 ns one out of 4 Flipflops is activated. When a pulse from the breakdown of the lidar detector reaches this circuit, the currently active Flipflop reverses its logical state, to mark a bin. This information in turn is stored in a shift register before the next gate of the sequence comes on. After a total of 250 gates, the shift register content is analysed by a computer and the recorded events are converted to a range information again. Figure 3 sketches the principle of this approach.

This concept was tested in a Rayleigh type of lidar experiment by pointing the telescope at a cloud layer. Figure 4 shows a plot of the ranges obtained versus the time interval over which the experiment was carried out. One can clearly see the lower cloud boundary at a range of about $5\mu s$. The clear section below $3\mu s$ is devoid of counts as it is within the dead time of of this experiment. This plot gives a good impression of the cloud movements during this measurement, since the lower boundary changed a lot with time. Converting these measurements to countrates and plotting them together with the theoretically calculated lidar equation show a very good agreement as one can see from figure 5 when the low sensitivity of the WLRS as a Rayleigh lidar system is taken into account by a constant scaling factor of 3×10^{-4} for all ranges. The hump, where measurement and lidar equation disagree is caused by the lower cloud boundary. The presence of clouds of course was not included in the calculations.

The data from the Raman scattering experiment was treated in similiar fashion. Figure 6 also shows a comparision between a measurement and the lidar equation. Again a constant scaling factor was required to match measurement and calculation, thus accounting for a lack of sensitivity. However for the Raman case this factor is only 0.15 as opposed to 3×10^{-4} for the Rayleigh case. Apart from this general lack of sensitivity a good agreement between model and measurement is evident. These scaling factors remain about constant, when different datasets are compared to the lidar model.

Some other datasets however do not agree so well with the model. Figure 7 gives an example of such a measurement. At around a distance of 500 m the lidar equation and the measured profile match quite well again. However for shorter ranges, one can see a significant discrepancy due to a countrate which is in excess of the usual values. A situation like this was not met very often, however it did happen from time to time. ~~In~~ some cases the disagreement was larger for short ranges as in the example above, while in other cases the discrepancy showed up at the far end. (See also figure 2 for this effect.)

4. CONCLUSIONS

Dualcolor laser ranging measurements have indicated that the water vapor content of the atmosphere is not sufficiently well modelled by using an assumed atmospheric profile and a value from a ground measurement which, for various reasons, is not representative for the atmosphere around the tracking station for various reasons. The basic idea is to use remote sensing techniques to obtain a full water vapor profile simultaneously with the range measurements to satellite. The temperature profile can be assessed likewise if it turns out to be of importance. As far as it is understood today, the atmospheric pressure profile does not require additional attention, since it is easier to model at the the resolution currently required.

In order to transform the measured countrate into a vertical water vapor profile the rescaled countrates were put into the lidar equation, which was solved for the parameter water vapor. Figures 8 and 9 show such profiles. The WLRS was firing to the bottom of a cloud during this measurement. Clearly one can see how the humidity increases, when the laser hits the cloud. This effect is even more pronounced when the same profile is converted to partial pressure of water vapor. Although this result was surprisingly good, the whole technique is far from being calibrated and routine. However, it could be shown that this approach is successful, specially under the circumstances. that no extra funding was available to support the work.

The goal behind the experiment reported here was to demonstrate, that lidar capabilities can be added to a ranging station and that it makes sense to do so. It made use of the telescope, the high power Nd:YAG laser system and the high detector sensitivity available from avalanche photodiodes operated in the geiger mode. Advantage was taken of the large amount of effort that went into the design of highly sensitive detection devices, suitable for lunar ranging. A big disadvantage for this work however was the fact, that the WLRS is operated in a monostatic configuration. This caused a lot of problems for the detection section, because direct backreflections of the transmit laser beam from parts of the telescope were many orders of magnitude brighter, than the atmospheric backscatter. It is expected that for the more common bistatic tracking stations a far better sensitivity will be achieved.

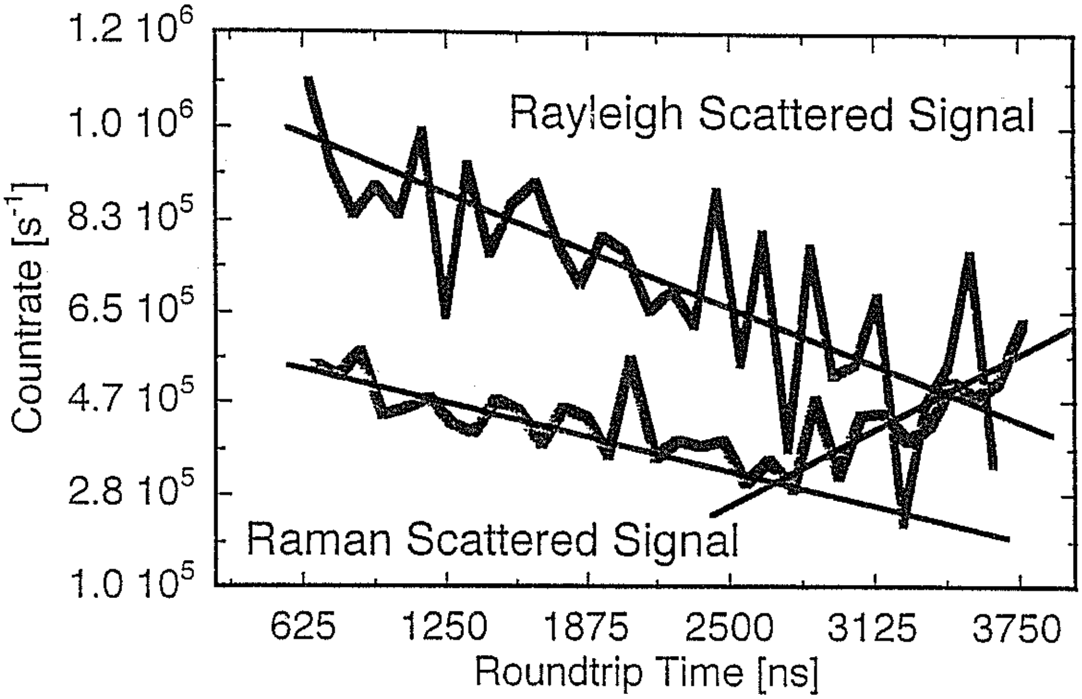

Figure 2: Histogram of countrates versus range of both a Rayleigh- (Mie-) and a Raman-scattering experiment. The elastic echo rate is roughly 4 magnitudes weaker than theoretically expected. The inelastic scattered signal is close to the expectations. The increase in the countrate towards long distances can be attributed to water vapor, since clouds formed rapidly shortly after this measurement

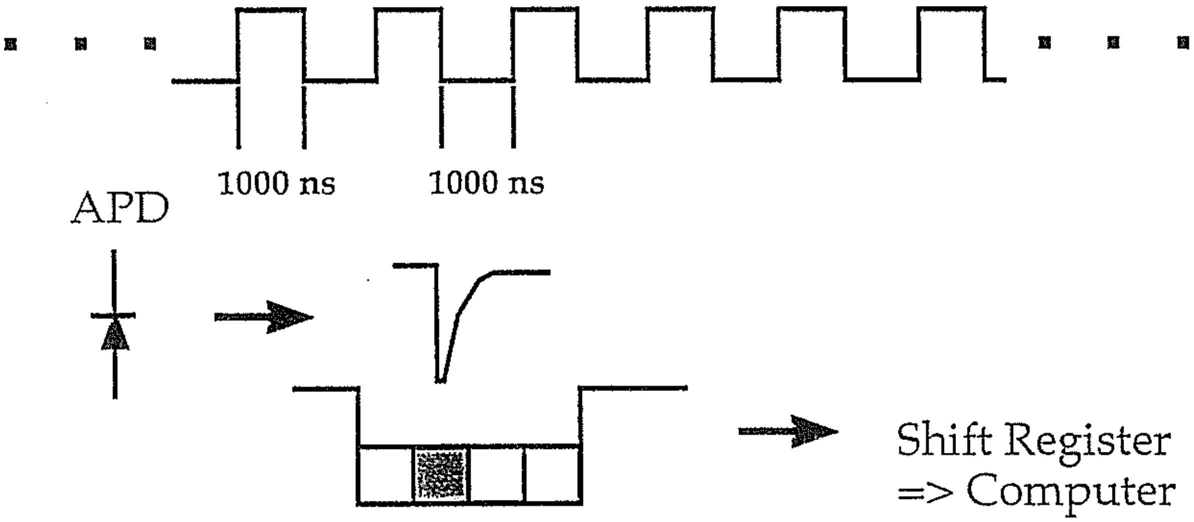

Figure 3: Rough sketch of the operating principle of the multigate detection scheme. Per laser shot there are 250 gates of $1\mu s$ width. Each gate is subdivided by 4 giving a range resolution of approximately 10 m

References

[1] J. W. Marini, C. W. Murray Jr.; *Correction of satellite tracking data for atmospheric refraction at elevations above 10 degrees*; NASA-TM-X-70555,(1973)

[2] U. Schreiber, St. Riepl; "Measuring atmospheric dispersion employing avalanche photo diodes", *Lidar Techniques for Remote Sensing, Chr. Werner, Editor*, Proc. SPIE 2310, **25**, (1994)

[3] A. Ansmann, M. Riebesell. U. Wandinger, C Weitcamp, E. Voss, W. Lahmann, W. Michaelis; "Combined Raman elastic- backscatter lidar for vertical profiling of moisture, aerosol extinction, backscatter and lidar ratio", *Appl. Phys. B* **55**, 18-28, (1992)

[4] U. Schreiber, R. Mayer, S. Riepl, K. H. Haufe; "Integrating LIDAR capabilities into Satellite Laser Ranging Operation", *Lidar Techniques for Remote Sensing, Chr. Werner, Editor*, Proc. SPIE 2581, (1995)

[5] R. Dassing, W. Schlüter, U. Schreiber; "Status Report on The New Wettzell Laser Ranging System (WLRS)", *Proceedings Of 7th International Workshop on Laser Ranging Instrumentation*, Matera. 1989

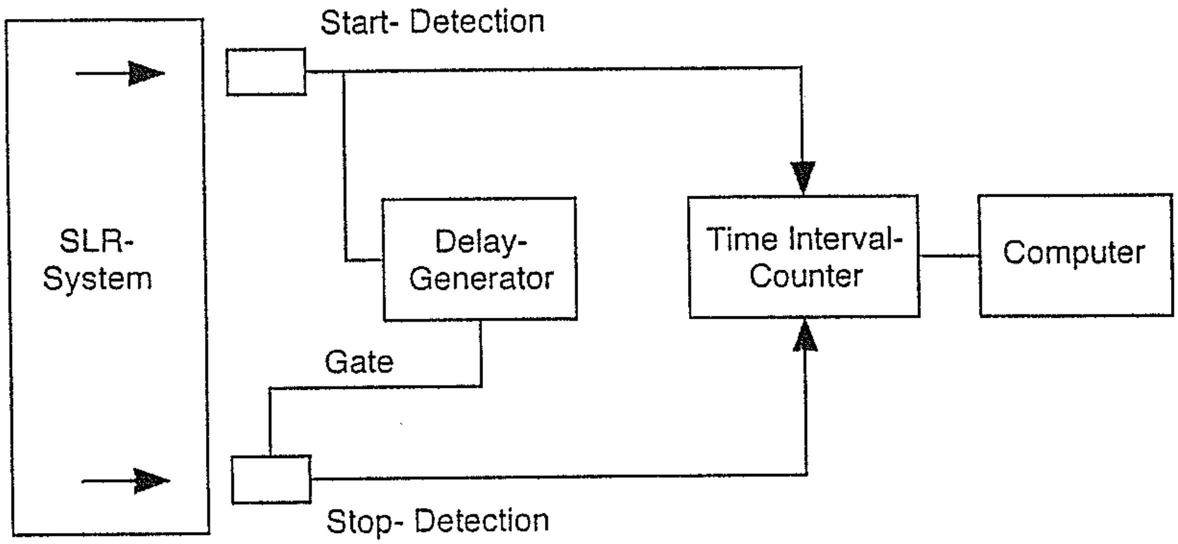

Figure 1: The block diagram of the experimental setup employed. The firing of the laser was detected by a photodiode and started the Time Interval Counter.The stop event was taken from the lidar detector. A delay generator avoided the recording of spurious reflections of the laser beam inside the telescope

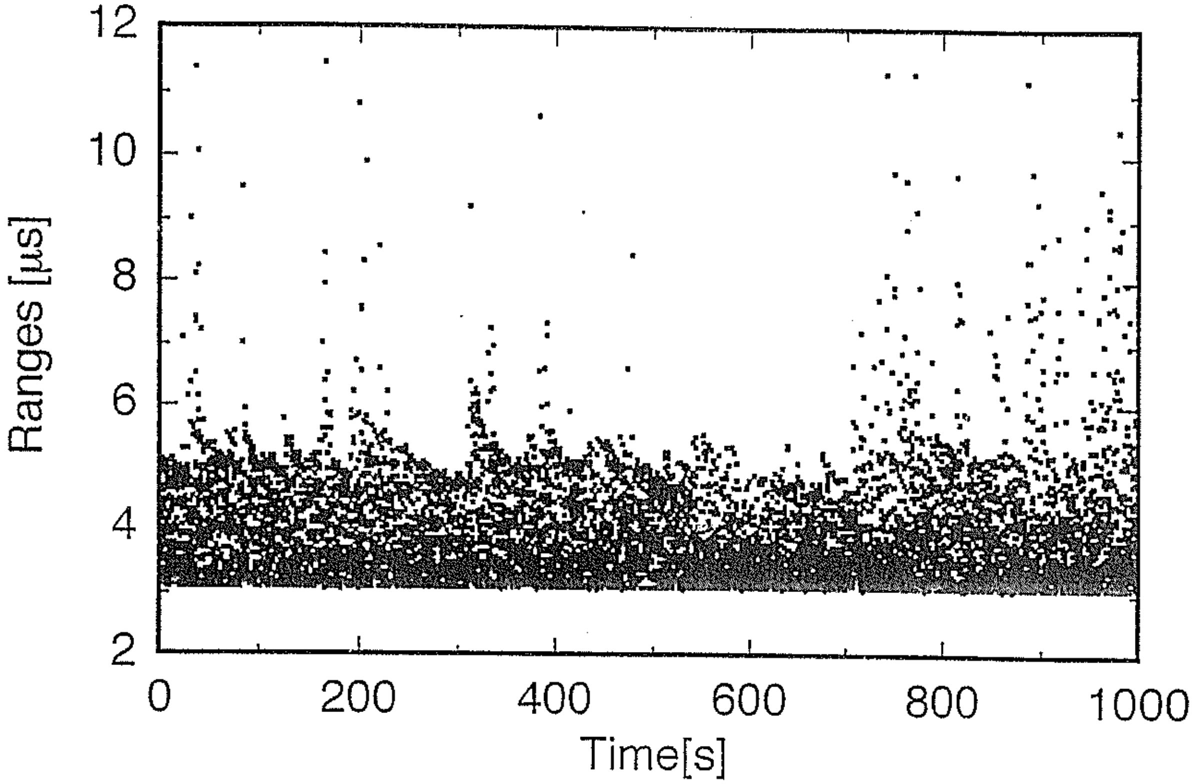

Figure 4: Plot of ranges versus time in the experiment, for an elastic backscatter lidar measurement. The telescope is pointing to a lower cloud boundary, which can be clearly identified at a range at around $5\mu s$. The dynamic changes of the cloud structure are also obvious

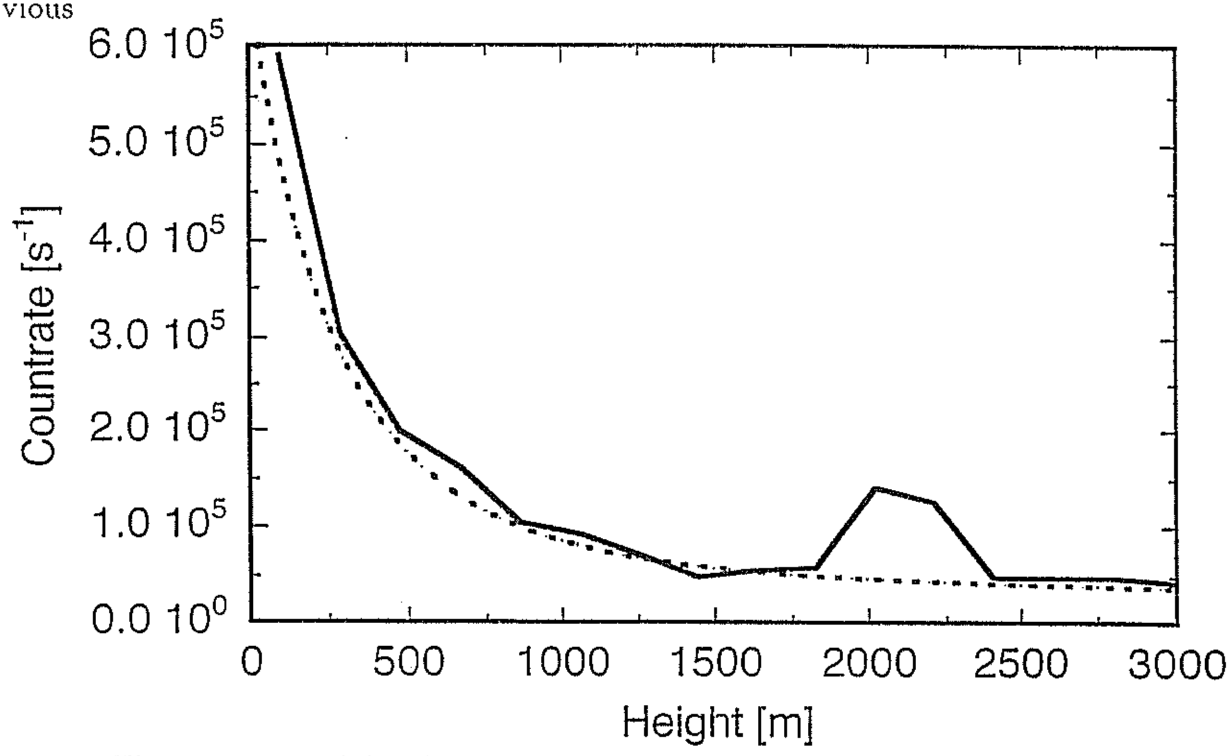

Figure 5: The countrate of the above shown measurement over range along with the calculated contribution from the lidar equation. There is a good agreement between measurement and model. The hump, which does not show up in the calculations is caused by the lower cloud boundary

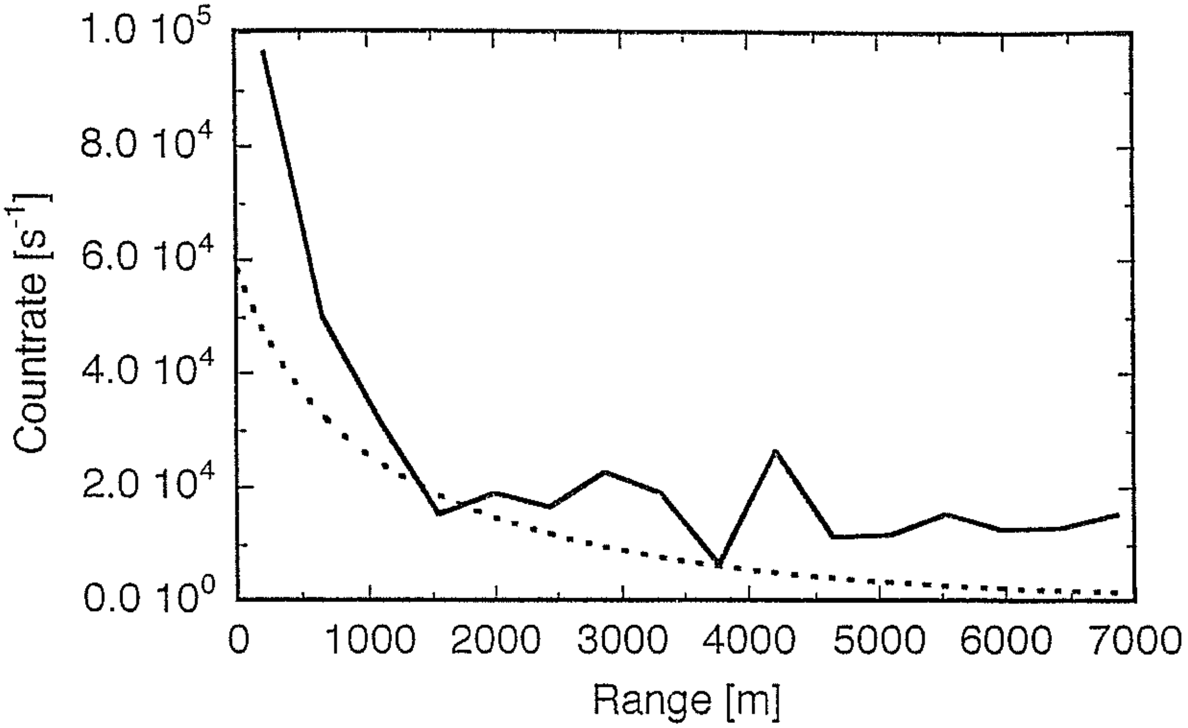

Figure 6: The countrate of a Raman measurement over range along with the calculated contribution from the lidar equation. There is a good agreement between measurement and model

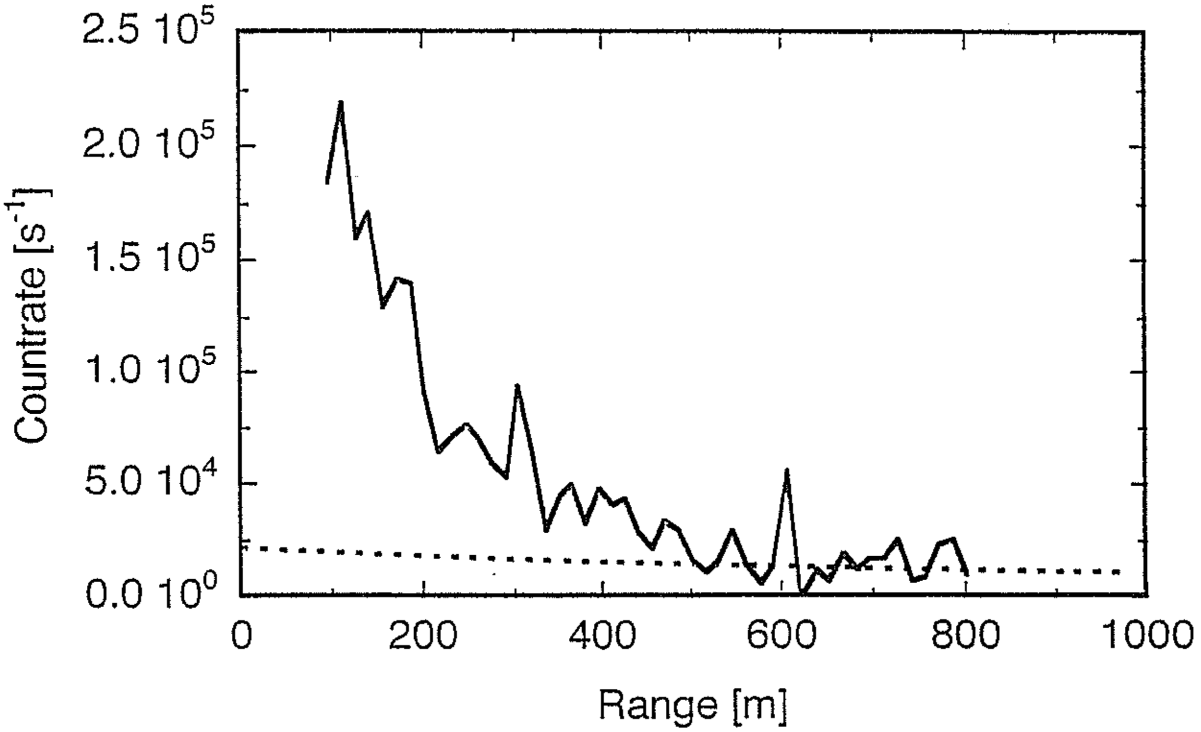

Figure 7: The countrate of another Raman measurement over range along with the calculated contribution from the lidar equation. The agreement between measurement and model is poor for short ranges

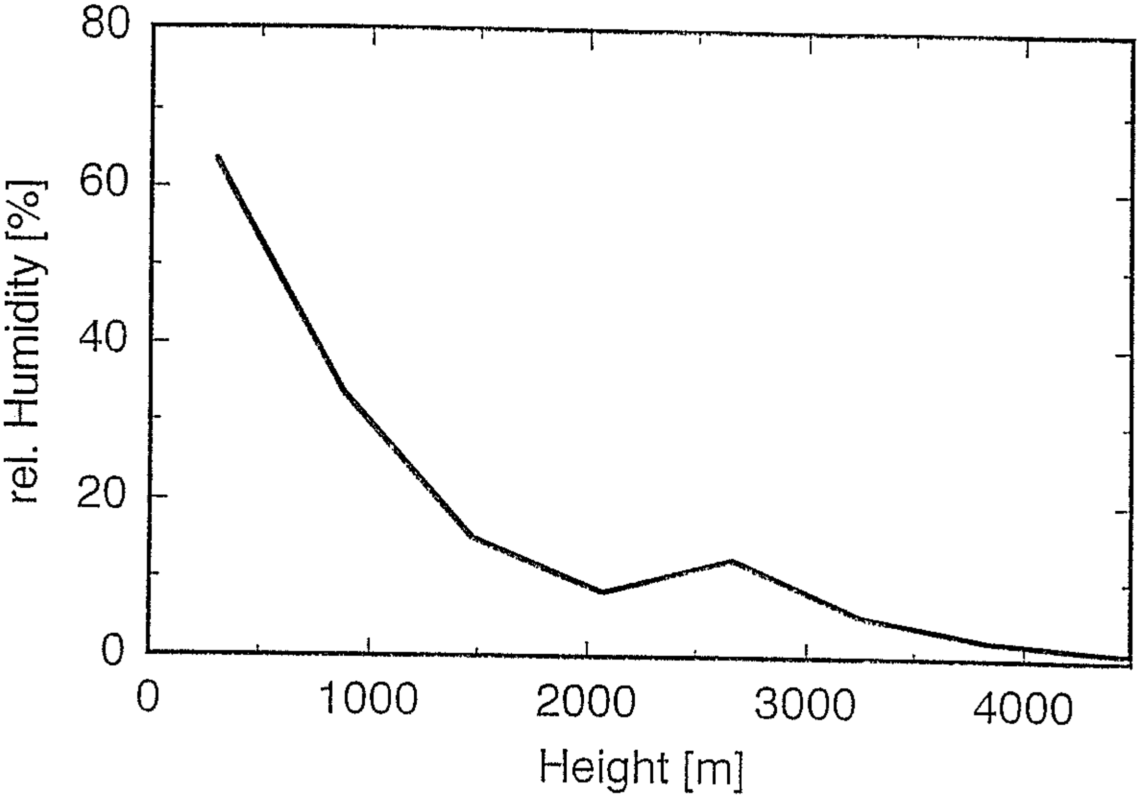

Figure 8: A vertical profile of relative Humidity around the WLRS for this given experiment. The telescope was pointing into a cloud, which showes up as a source of additional water at a distinct range

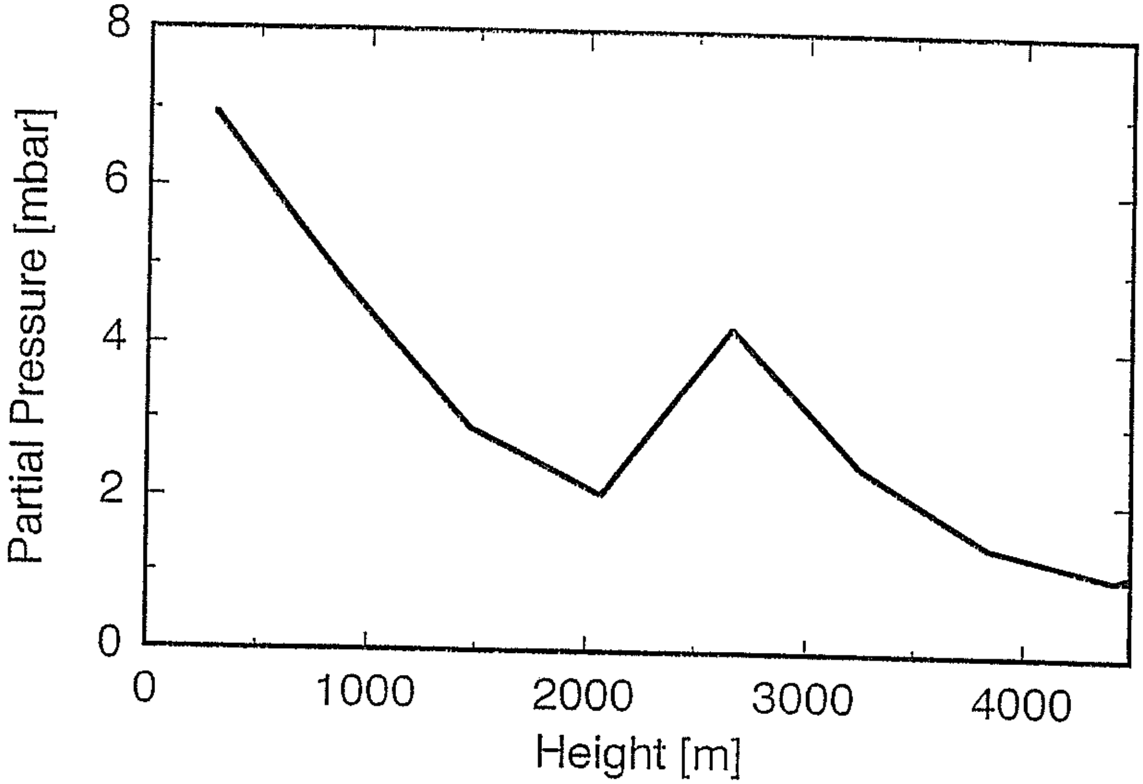

Figure 9: The same vertical profile of Humidity around the WLRS, converted into partial pressure of water vapor. In this plot the cloud shows up more dramatically

ON-ORBIT MEASUREMENT OF TOPEX IMPULSE RESPONSE: ASSESSMENT OF COHERENT INTERACTION AND VERIFICATION OF RANGE CORRECTION

THOMAS VARGHESE*, THOMAS W. ZAGWODZKI, JAN F. MCGARRY, JOHN J. DEGNAN.
BRION CONKLIN*
NASA/Goddard Space Flight Center, Greenbelt, Maryland 20771, USA.
*AlliedSignal, 7515 Mission Drive, Lanham, Maryland 20706, USA.
e-mail: varghet@thorin.atsc.allied.com.

The orbit precision of Topex is at the level of ~3cm. This is a remarkable accomplishment considering the fact that Topex is an active satellite with a large laser retroreflector array (LRA). If the observed station range biases (0.5 -1.5 cm) can be eliminated or reduced to the level of a few millimeters (mm), the accuracy of the Topex orbit can be improved substantially. Indeed, it can be made comparable to that of Lageos. The accurate knowledge or verification of the satellite center of mass (CM) is thus critical to resolving any questions concerning the range biases and the accuracy of the orbit.

The CM correction is deduced from the impulse response (IR) of the satellite and is estimated using far field diffraction theory. The Topex Precision Orbit Determination (POD) team (JPL, NASA GSFC, SAO, AlliedSignal) for the CM determination decided to use the incoherent superposition approach to compute the satellite response. This is for reasons of computational ease for deducing the satellite response for various laser and receiver configurations. The coherent case would have entailed computing the individual satellite impulse response for a large number of random phases and then deducing a mean IR from these instantaneous responses of the satellite. In fact, the incoherent case is a limiting case of the coherent superposition when the pulse width and the contributing number of cubes are large.

The coherent interaction of short laser pulses can generate fairly complex waveforms from a satellite that has a large LRA with close spacing. Short picosecond (<30 ps) pulses are capable of mapping this characteristic when used in conjunction with a high resolution (~2 ps) streak camera receiver system. Such a capability allows accurate on-orbit temporal mapping of the satellite and thereby the determination of the satellite IR. It will also allow to verify the impact of coherent interaction and its effect on the magnitude of the range correction to the CM of the satellite.

It was proposed to the JPL project office in 1992 that it would be extremely beneficial to have a direct on-orbit measurement to verify the actual performance. This will help to alleviate any concerns or questions regarding the accuracy of the FFDP model and make the model robust by validating it with experimental data. This activity was not funded and was pursued by NASA Space Geodesy project office within the constraints of its fiscal budget.

NASA GSFC 48 inch telescope facility has the infrastructure to support these measurements. The optically calibrated streak camera based receiver system in this facility has a resolution of ~ 1.5 ps and an accuracy of ~ 1 ps. This allows to determine the temporal variations accurately. A number of measurements at 532 nm were conducted in the past to collect the data to support this investigation. This paper highlights the initial results of this ongoing measurement and analysis.

The preliminary results show that the satellite return pulse temporal structure varied considerably for short laser pulse width such as 30 ps. For a short input pulse, the number of cubes contributing to the resulting pulse envelope is quite small. The composite waveform thus generated, does not enjoy the benefit of the statistical averaging for the various temporal locations defining the pulse envelope, unlike a wide pulse. The phase variations from shot to shot will, therefore, produce varying temporal and amplitude structure. The features illustrated in several slides indicate the variability seen in the experimental waveforms and is indicative of the coherent interaction.

These measurements can also provide insight into the actual on-orbit LRA thermal conditions. There may be an impact on CM correction from the variations in the FFDP resulting from the thermal gradients due to the partial solar loading / shading of the LRA. We expect to collect more data in the future to make further investigation of this interesting problem and discern the behavior of the FFDP under different solar loading conditions..

TOPEX TEMPORAL RESPONSE:
ON-ORBIT MEASUREMENT

Background:

- Topex **LRA model** (and CM correction) is quite **complex.**
- Model is built on the **incoherent superposition** of the computed intensities of the FFDP of 192 single cubes. Coherent model may change the CM correction.
- **No Integrated experimental measurement** was possible in the laboratory for the LRA due to its large diameter.
- **Laboratory FFDP** measurement of a number of cubes and trays were performed at GSFC. **Variability of the FFDP** was observed experimentally among the trays and the cubes.
- **On-orbit behavior** may be different due to the space environment <low temp, selective sunloading,...>

TOPEX: COMPUTED IMPULSE RESPONSE
Inc. Ang. (angle wrto nadir) = 10 Degree

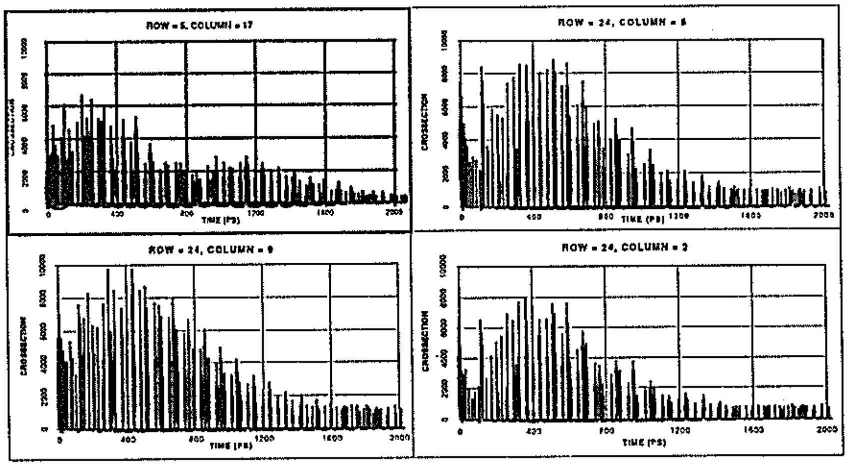

TOPEX TEMPORAL RESPONSE:
COHERENT INTERACTION

- The **coherent interaction** between short pulses depends on the **spatio-temporal overlap** between the pulses.
- Coherent interaction results in the **vector addition** of the amplitudes.
- The **resultant amplitude** (and therefore the intensity) depends on the **phase characteristics** and the number of pulses contributing to the process.
- The **resultant temporal structure** can be quite **complex** depending on the number of pulses and spacing.
- **Shot-to-shot variability** can be significant depending on the above factors.

TOPEX TEMPORAL RESPONSE:
COHERENT INTERACTION

"A(t) " is the instantaneous amplitude of the reflected pulse from a cube. "σ" is the gaussian half width of the pulse. "φ" is the resultant phase on reflection from the cube. "δt " is the temporal offset of the reflection plane of the cube with respect to the cube closest to the source of the wavefront. "I" is the resultant intensity from the entire array computed using coherent or incoherent superposition. "m" is the index for the discrete time and "j" that for the cubes.

$$A_1(t) = |a_1| \exp(-(t + \delta t_0)^2 / 2\sigma^2) \exp(\pm i \phi_1)$$

$$A_2(t) = |a_2| \exp(-(t + \delta t_1)^2 / 2\sigma^2) \exp(\pm i \phi_2)$$

.....

$$A_n(t) = |a_n| \exp(-(t + \delta t_{n-1})^2 / 2\sigma^2) \exp(\pm i \phi_n)$$

$$I_{coh} = \left\| \sum_{m=1}^{n} [\sum_{j=1}^{k} \{ |a_j| \exp(-(t_m + \delta t_{j-1})^2 / 2\sigma^2) \exp(\pm i \phi_j) \}] \right\|^2$$

$$I_{incoh} = \sum_{m=1}^{n} [\sum_{j=1}^{k} \left\| \, |a_j| \exp(-(t_m + \delta t_{j-1})^2 / 2\sigma^2) \right\|^2$$

TOPEX TEMPORAL RESPONSE:
FACTORS AFFECTING LRA COHERENT INTERACTION

- The **diffracted outputs** from the cubes of the Topex LRA can produce a **complex temporal structure** to the waveforms.
- **Satellite** motion is essentially **frozen** during the time of a picosecond pulse.
- **Pulse to Pulse variability** from the satellite is a function of several key parameters:
  - **number of contributing cubes**
  - **effective separation between the cubes wrto a plane wave.**
  - **laser pulse temporal characteristics**
  - **FFDP of the individual cubes.**

TOPEX TEMPORAL RESPONSE:
Computed vs Measurement

OBJECTIVES:

- Examine the **differences between computed and measured waveforms** for various azimuths and elevation.
- Assess the Impact if any on the the range correction to the CM of the satellite.
- Verify and validate or modify the current CM correction values.
- Examine the differences between coherent and incoherent superposition.

TOPEX: Computation of the Temporal Response

- Determine the "Location" in the FFDP for the observing station based on the **orbit from "Geodyn"** and and the **spacecraft attitude from spacecraft telemetry data.**
- Compute the **LRA impulse response** based on that location.
- **Compute the Az, El angles** corresponding to the intensities at specific nadir angle values for the LRA <0,5,10,....55>
- **Generate pulses with random phases** and assign the phases using a random number generator.
- Assuming a randomly phased array, determine the **integrated response of the LRA using coherent superposition** of the intensities of 192 cubes.
- Compute an **average waveform.**

TOPEX: COMPUTED WAVEFORM:
Inc. Ang. = 10 Degree; Laser Pulse= 30ps; Incoherent Superposition

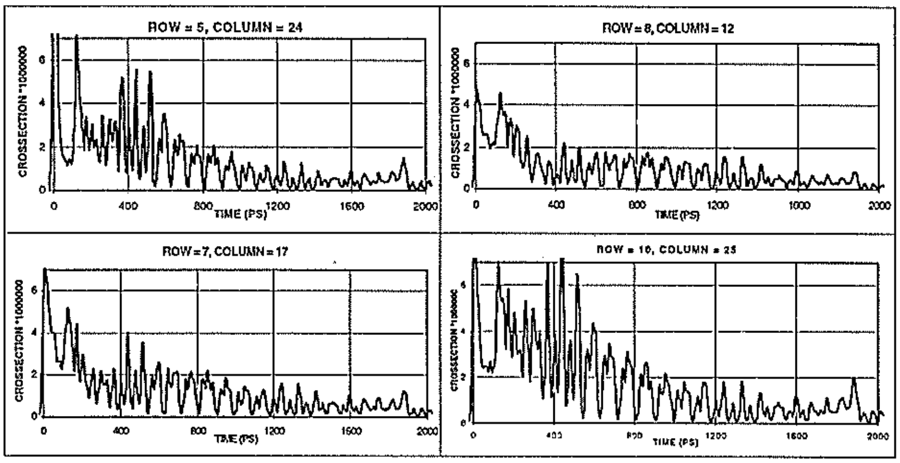

TOPEX: : Analysis of the Temporal Response

- Compute the **Average Experimental Waveform.** Time interval to be detrmined based on the pulse to pulse variations and the amount of data.
- **Compare and Contrast** the **average experimental waveforms** at different Azimuth And Elevation Angles With That Deduced From the **theoretical** Model.
- Compute the response of the tracking stations by **convolving the experimental waveforms** with the temporal response of the Ranging detectors employed.
- Compute the **range correction differences.**

TOPEX: : Measurement of the Temporal Response

- **Measure** the on-orbit **"impulse response"** of the satellite.
- Ideally, one would like to have a very short laser pulse, e.g., <10 picosecond laser for a satellite like Topex.
- Short **picosecond (<30ps) laser pulses** in conjunction with a **high resolution (~2 ps) streak camera** receiver system can resolve the temporal response fairly well.
- **Recently improved data rate** from the NASA 48-Inch Telescope Facility allows to examine this problem.

TOPEX: Experimental Waveforms

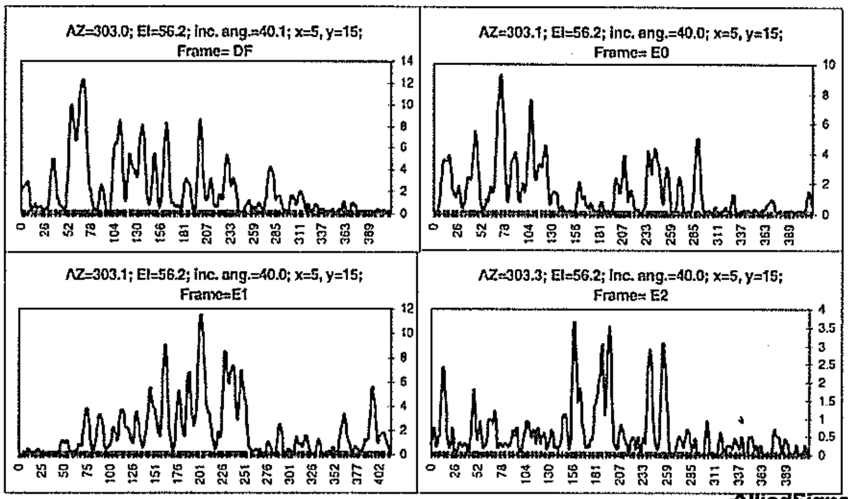

TOPEX: Experimental Waveforms

Shot to shot Variability of the pulse amplitude and temporal structure is indicative of coherent interaction.

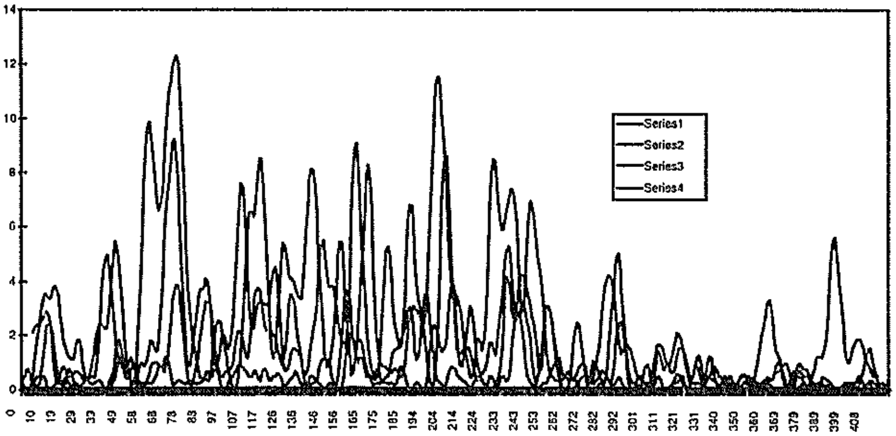

TOPEX: Experimental Measurement

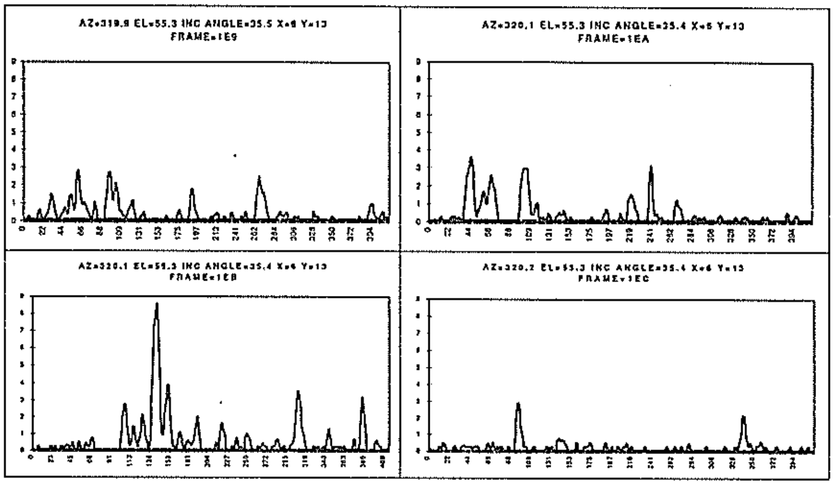

TOPEX TEMPORAL RESPONSE: Preliminary Results

- **Preliminary results indicate that the shot-to-shot variations are significant**
  - –When the **input laser pulsewidth is quite short** such as 30 ps, the temporal overlap is quite small and hence the number of pulses contributing to the coherent interaction is small. This will naturally lead to large variations.
  - –If the **pulsewidth were larger (>150ps)**, there will be a substantial number of pulses contributing to the resulting pulse envelope and possibly less variations from shot-to-shot.
- A **rigorous computational and measurement framework** is being established to verify the on-orbit performance of the LRA.
- **More experimental data** is needed to **examine and validate the model.**

Refined mathematical model of satellite WPLTN-1-FIZEAU.

Eng.V.Burmistrov, Prof.V. Shargorodsky, Prof. V. Vassiliev, Dr.N.Soyuzova
Russian Institute for Space Device Engineering

Summary

Corrected results are presented of an analysis of the efficiency and accuracy parameters for the passive laser satellite WPLTN-1-Fizeau aimed for submillimeter-accuracy SLR technology demonstration. The satellite has been designed using the "one direction--one retroreflector" technology. The analysis has been done using a corrected model taking into account the slant beam incidence at the retroreflector, the mutual orientation of the velocity abberration direction and prism, as well as the reflected signal level used as weighting function.

The analysis has shown that the reflected signal level at the wavelenght of 0.532 μm in the case of the Fizeau effect presence will be 5 to 15 times (depending on the satellite angular position during observation) higher than in the case of its absence. The RMS difference between the satellite mass center and the measurement point defined by its design should not exceed 0.5 mm.

- For spherical passive spacecraft designed in a way that a few retroreflectors take part in reflection of laser light, as a rule major part of light is reflected by those retroreflectors on which light comes with angles close to normal. That is why optimization of width and shape of reflection pattern of retroreflectors of such spacecraft is usually performed for normal light incidence on a retroreflector.
- For satellites designed basing on principle "one direction-one retroreflector" each retroreflector serves some range of angles of light incidence on a satellite, in each such range all directions (including normal incidence) have the same probability. In this case optimization of retroreflector pattern should be done not for normal incidence, but in a way to provide maximum number of reflected signals within all field of view of a reflector.
- This consideration used for mathematical model of satellite WPLTN-1-FIZEAU designed basing on the principle "one direction-one retroreflector" and equipped with retroreflectors with reflection patterns optimal for Fizeau effect action, allowed to specify its energy and accuracy parameters both for classical interpretation of velocity aberration phenomenon, and for case of Fizeau effect influence.
- Energy efficiency of retroreflector within its field of view (1), which functionally depends on width and shape of reflection pattern is calculated to perform energy and accuracy estimations. Width and shape of reflection pattern, in their turn, are defined by size and direction of the beam inclination relative to velocity aberration vector.
- Systematic correction (3) and RMS of link of range measurements to the spacecraft's center of mass (4) are defined by averaging of weighted random values of systematic correction and squares of deviations within retroreflector's field of view. Normalized energy efficiency of retroreflector is used as weight function (2).
- As a main parameter for evaluation of correctness of selection of basic width and shape of reflection pattern there is used level of reflected signal averaged within

working field of view of the spacecraft (5). Maximization of this parameter by predefined accuracy, mass-dimension or other basic parameters can be a criterion for optimum design. It also can be a criterion for evaluation of different technical solutions or hypotheses, in particular this criterion is supposed to be used for testing of Fizeau effect influence on reflection of laser radiation from the spacecraft WPLTN-1-FIZEAU.

- We performed experimental studies of reflection patterns of retroreflectors with baffles from which it was seen that even with sloped light incidence (to 0°) there can be considerable (doubled) widening of reflection patten in the direction of beams slope (fig.1, fig.2).
- For evaluation of degree of influence of Fizeau effect on quantity of signals reflected from the spacecraft WPLTN-1-FIZEAU, we calculated energy efficiency of retroreflectors depending on angle of beams slope, for case of Fizeau effect influence (solid line) and classical interpretation (dotted line) during range measurements at wavelength 0.532 μm. Dependencies are calculated for position of a spacecraft in zenith (velocity aberration is maximal) and at zenith dinstance 70° (velocity aberration is minimal) (fig.3, fig.4).
- Dependencies are calculated for case of beams slope in direct and orthogonal direction relative to velocity aberration vector. From them it is seen that at slope angles 5-8 degrees in the plane of velocity aberration vector, there is considerable increase of retroreflector's efficiency.
- Table 1 contains maximal and average level of reflected signal at wavelength 0.532 μm in absence and in presence of Fizeau effect. From analysis of given values one can make a decision that accounting increase of efficiency of retroreflector at sloped light incidence reduces difference of levels of reflected signal in case of presence or absence of Fizeau effect influence from 500-100 to 10-15 times. Accounting sloped light incidence for ranging at wavelength 1.54 μm does not lead to drastic changes of this ratio (table 2).
- Tables 3 and 4 contain averaged RMS errors and systematic corrections at wavelengths 0.532 and 1.54 μm. Accounting sloped light incidence leaded to insufficient increase of RMS error with classical interpretation of velocity aberration. Accounting sloped light incidence discovered slight dependence of systematic correction on velocity aberration value which depends on spacecraft zenith distance. This dependence needs to be taken into account during processing of laser ranging measurements of spacecraft WPLTN-1-FIZEAU.

BASIC PROPORTIONS

* Energy efficiency of retroreflector within its field of view:

$$S_{eff} = f(\Psi(\varepsilon,\alpha),\overline{\Theta},\alpha,\varepsilon) \qquad (1)$$

where : $\overline{\Theta}$ - velocity aberration vector;
ε - angle of light incidence on retroreflector;
α - angle of light incidence relative to velocity aberration vector;
Ψ(ε,α) - retroreflector's pattern

* Normalized energy efficiency (weight function):

$$P = \frac{S_{eff}(\Psi(\varepsilon,\alpha),\overline{\Theta},\alpha,\varepsilon)}{\int^{\Omega_r} S_{eff}(\Psi(\varepsilon,\alpha)\overline{\Theta},\alpha,\varepsilon)d\Omega} \qquad (2)$$

where: Ω_r=f(ε,α) - reteroreflector field of view.

* Averaged weighted systematic correction:

$$\overline{L} = \int^{\Omega_r} P(\Psi(\varepsilon,\alpha),\overline{\Theta},\alpha,\varepsilon)L(\varepsilon)d\Omega \qquad (3)$$

where L(ε) - dependence of current value of systematic correction from the angle of light incidence on retroreflector

* Root mean square deviation of link of measurements to the spacecraft center of mass:

$$\overline{\sigma} = \sqrt{\int^{\Omega_r} P(\Psi(\varepsilon,\alpha),\overline{\Theta},\alpha,\varepsilon)(\overline{L} - L(\varepsilon))^2 d\Omega} \qquad (4)$$

* Average statistical level of signal reflected from a spacecraft:

$$n = \frac{\sum\Omega_r}{4\pi}\frac{1}{\Omega_r}n_0\int^{\Omega_r} S_{eff}(\Psi(\varepsilon,\alpha),\overline{\Theta},\alpha,\varepsilon)d\Omega \qquad (5)$$

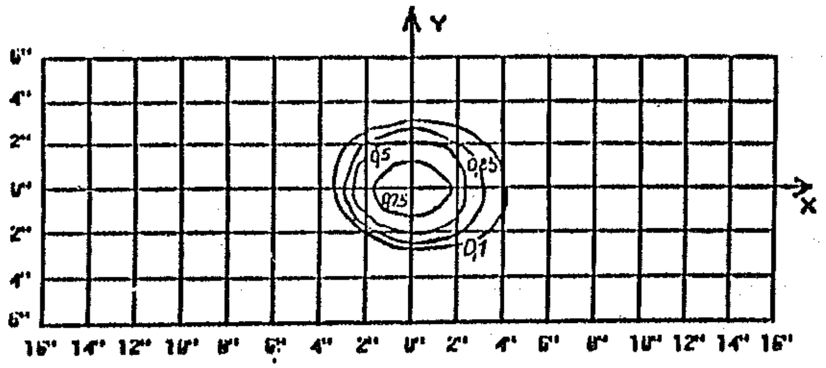

Fig.1 Reflection pattrn of a diffraction-limited retroreflector D_{RR}=28 mm at normal light incidence.

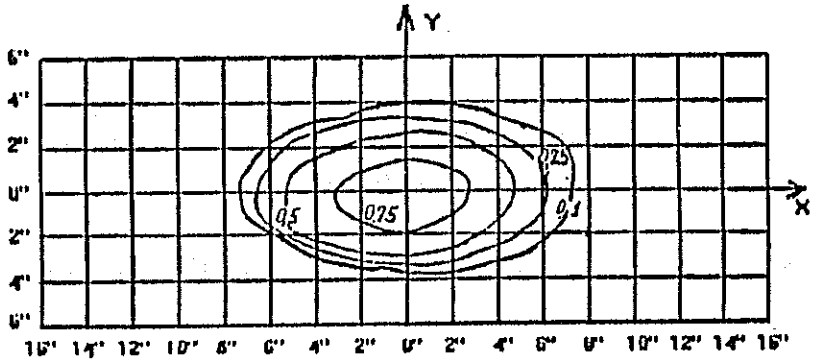

Fig.2. Reflection pattern of a diffraction-limited retroreflector with baffles H=26 mm, D_{RR}=28 mm with light incidence angle 10°.

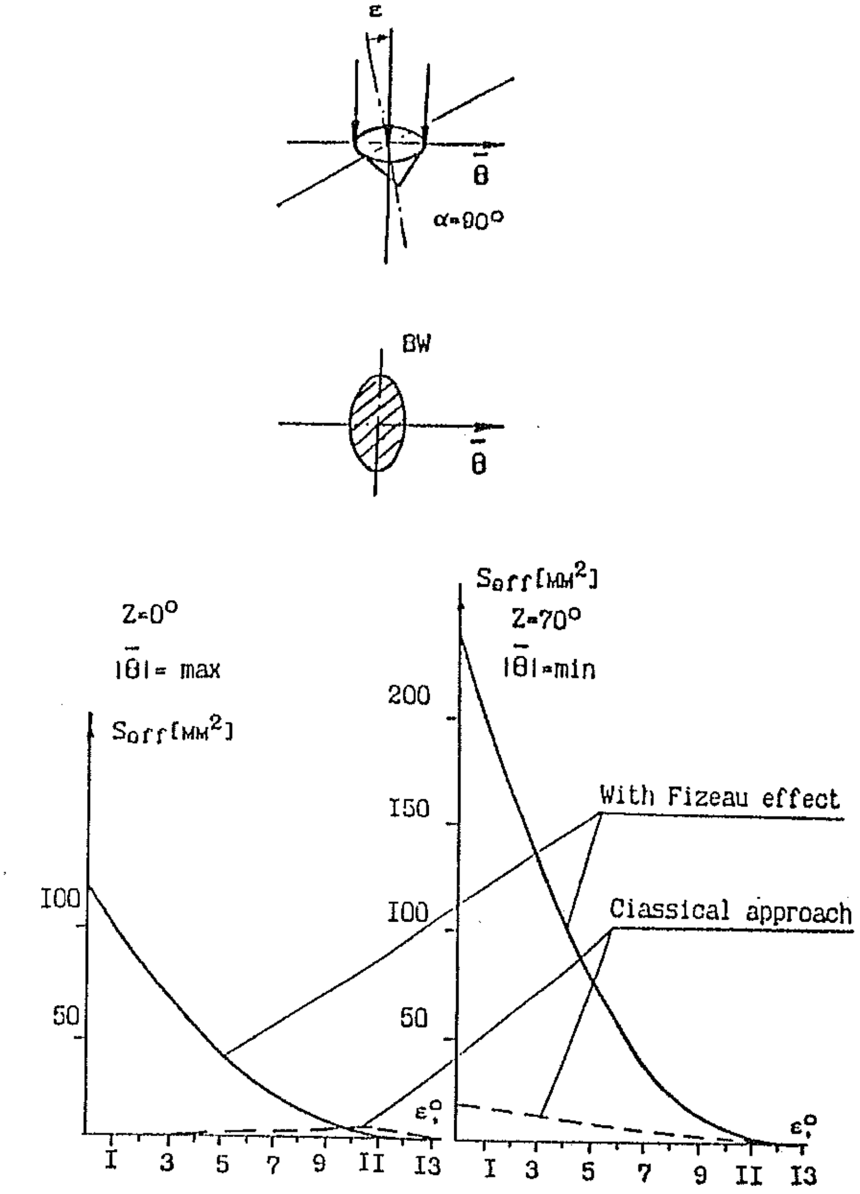

Fig.3. Energy efficiency of retroreflector with parallel direction of retroreflector's inclination relative to velocity aberration vector.

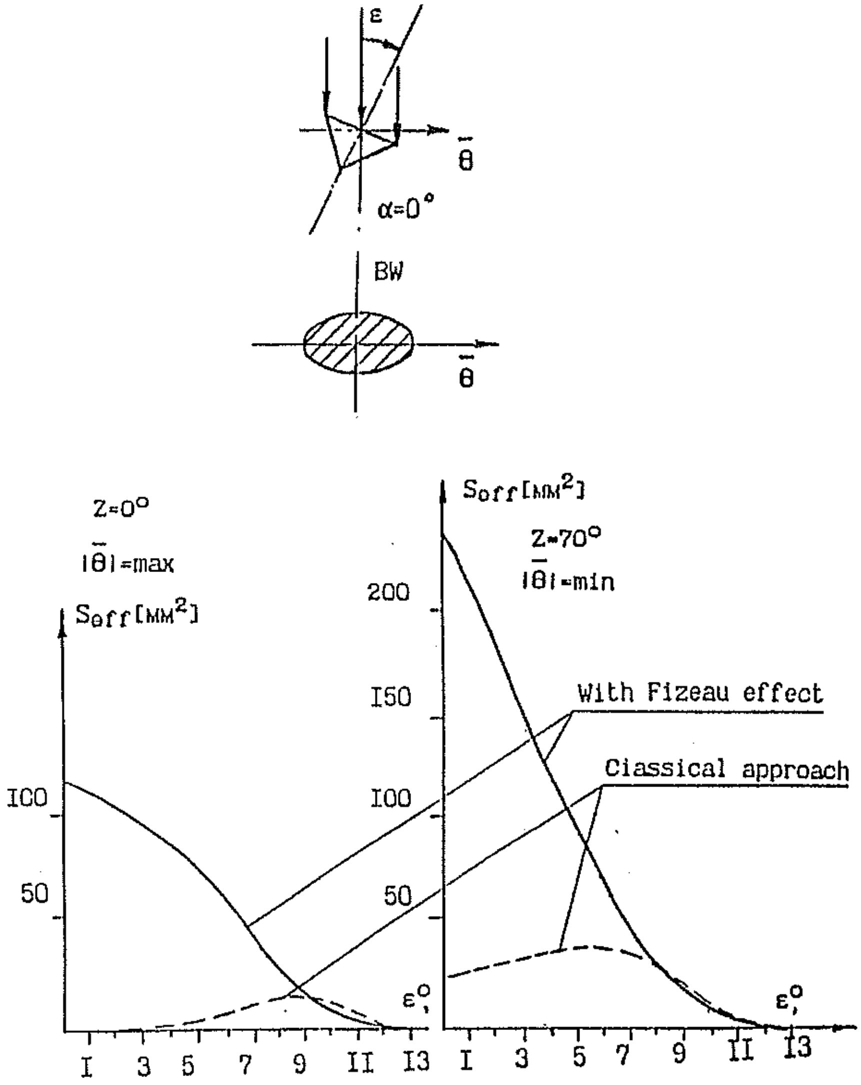

Fig.4. Energy efficiency of retroreflector with orthogonal direction of retroreflector’s inclination relative to velocity aberration vector.

Energy potential of "WPLTN-1- FIZEAU" satellite during laser ranging at wavelength 0.532μm.

Table 1.

Zenith distance, arc degrees	Compensation of velocity aberration				Classical velocity aberration			
	Zenith pass		Parameter pass		Zenith pass		Parameter pass	
	n_S^*	$n_{S\max}$	n_S^*	$n_{S\max}$	n_S^*	$n_{S\max}$	n_S^*	$n_{S\max}$
0	13.3	64.8	13.3	64.8	0.91	4.0	0.91	4.0
10	12.7	62.2	12.5	60.7	0.87	3.9	0.85	3.7
20	10.9	54.5	10.2	49.7	0.85	3.5	0.7	3.1
30	8.1	42.8	7.2	35.2	0.7	2.9	0.49	2.2
40	5.2	29.2	4.3	20.9	0.6	2.2	0.29	1.3
50	2.7	16.1	2.1	10.0	0.4	1.4	0.14	0.6
60	1.0	6.5	0.7	3.5	0.2	0.7	0.05	0.2
70	0.22	1.46	0.15	0.7	0.06	0.21	0.01	0.04

Energy potential of "WPLTN-1- FIZEAU" satellite during laser ranging at wavelength 1.54μm.

Table 2.

Zenith distance, arc degrees	Compensation of velocity aberration				Classical velocity aberration			
	Zenith pass		Parameter pass		Zenith pass		Parameter pass	
	n_S^*	$n_{S\max}$	n_S^*	$n_{S\max}$	n_S^*	$n_{S\max}$	n_S^*	$n_{S\max}$
0	63.3	457.2	63.3	457.2	36.2	166.7	36.2	166.7
10	59.8	432.3	59.6	430.8	34.7	161.4	34.1	157.1
20	50.4	365.6	49.8	359.9	30.5	145.6	28.5	131.2
30	37.2	271.7	36.5	263.7	23.5	120.6	20.9	96.1
40	23.7	174.7	23.0	166.4	16.2	88.2	13.2	60.7
50	12.6	93.8	12.1	87.6	9.2	54.4	6.9	32.0
60	5.3	39.7	5.04	36.4	4.1	26.1	2.9	13.3
70	1.6	11.8	1.5	10.6	1.3	8.6	0.8	3.9

Accuracy characteristics of "WPLTN-1-FIZEAU" satellite during ranging at wavelength 0.532 μm.

Table 3

Zenith distance, arc degrees	Compensation of velocity aberration				Classical velocity aberration			
	Zenith pass		Parameter pass		Zenith pass		Parameter pass	
	δ	Δ_c	δ	Δ_c	δ	Δ_c	δ	Δ_c
0	0.429	62.574	0.429	62.574	0459	61.928	0.459	61.928
10	0.428	62.576	0.429	62.574	0.460	61.937	0.459	61.928
20	0.425	62.583	0.429	62.574	0.467	61.977	0.459	61.928
30	0.422	62.591	0.429	62.574	0.473	62.029	0.459	61.928
40	0.418	62.602	0.429	62.574	0.483	62.113	0.459	61.928
50	0.413	62.613	0.429	62.574	0.488	62.209	0.459	61.928
60	0.409	62.622	0.429	62.574	0.486	62.312	0.459	61.928
70	0.405	62.632	0.429	62.574	0.476	62.403	0.459	61.928

Accuracy characteristics of "WPLTN-1-FIZEAU" satellite during ranging at wavelength 1.54 μm.

Table 4

Zenith distance, arc degrees	Compensation of velocity aberration				Classical velocity aberration			
	Zenith pass		Parameter pass		Zenith pass		Parameter pass	
	δ	Δ_c	δ	Δ_c	δ	Δ_c	δ	Δ_c
0	0.3966	62.970	0.3966	62.970	0430	62.889	0.430	62.889
10	0.3965	62.970	0.3966	62.970	0.429	62.891	0.430	62.889
20	0.3961	62.971	0.3966	62.970	0.426	62.900	0.430	62.889
30	0.3956	62.972	0.3966	62.970	0.423	62.908	0.430	62.889
40	0.3938	62.974	0.3966	62.970	0.418	62.920	0.430	62.889
50	0.3942	62.975	0.3966	62.970	0.413	62.933	0.430	62.889
60	0.3936	62.976	0.3966	62.970	0.408	62.944	0.430	62.889
70	0.3930	62.978	0.3966	62.970	0.404	62.954	0.430	62.889

Study of retroreflectors with two-spot reflection pattern at sloped light incidence.

Eng.V.Burmistrov, Prof.V.Shargorodsky, Prof.V.Vassiliev, Dr.N.Soyuzova

Russian Institute for Space Device Engineering

Summary

Results are presented of experimental investigation of the two-lobe reflection pattern variations depending on the beam incidence angle for prism retroreflectors with a limited field of view in retroreflector systems using the technology "one direction--one retroreflector". As follows from the experimental data, with the increasing beam incidence angle the shape of the reflection pattern becomes unacceptably distorted, changing from a two-lobe one to a single-lobe one. Therefore by designing laser retroreflector systems with two-lobe retroreflectors the beam incidence angle at the retroreflector should not exceed 13 deg.

- Optical retroreflec tor antennas (ORA), designed basing on retroreflectors (RR) with two-spot reflection pattern (RP) used for compensation of classical velocity aberration, have 5-10 times higher energy efficiency. As it is known, ORA with such design was successfully tested on spacecraft METEOR-3 during in-flight laser testing of PRARE system.
- Upon request of Potsdam Geodesy Center (GFZ), we studied possibility of use of RR with two-spot RP on ORA consisting of four retroreflectors which GFZ plans to install on CHAMP spacecraft. Specific feature of this design is that in order to reduce cost, it is proposed to provide all field of view of ORA by minimal quantity (four) retroreflectors. With such design, retroreflectors are operating at considerable angles of light incidence- up to 45 arc degrees.
- We performed detailed measurements of change of two-spot reflection pattern with increasing angle of light incidence to RR. For the experiment there was selected a RP optimal for CHAMP orbit height with distance 13.7 arc seconds between center of spots at normal light incidence. We measured five reflection patterns for incidence angles 0, 13,20,30 and 40 degrees which are shown in fig. 1,2, 3, 4, 5, respectively.
- Analysis of measurements result showed that at big incidence angles two-spot reflection pattern turns into one-spot and at the distance of about 7 arc seconds from the center of RP efficiency of RR is:

at	3°	0.47
	20°	0.147
	30°	0.055
	40°	0.02

- This means that in design of ORA basing on RR with two-spot RR, one shall take measures so as number of reflectors is such that angle of light incidence on RR is not more than 13 arc degrees. With larger incidence angles reflection patterns becomes ineffective and, as a consequence, efficiency of ORA becomes intolerably small and insufficient for reliable registration of reflected signal in considerable part of satellite visibility zone.

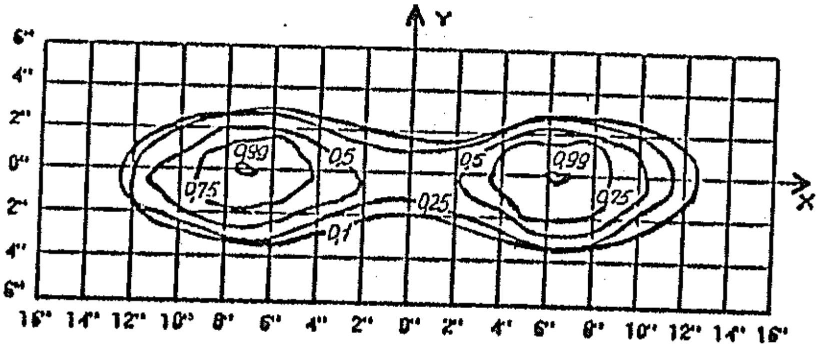

Fig.1. Retroreflector's reflection pattern at normal light incidence. Reflection efficiency in maximum is 1.00.

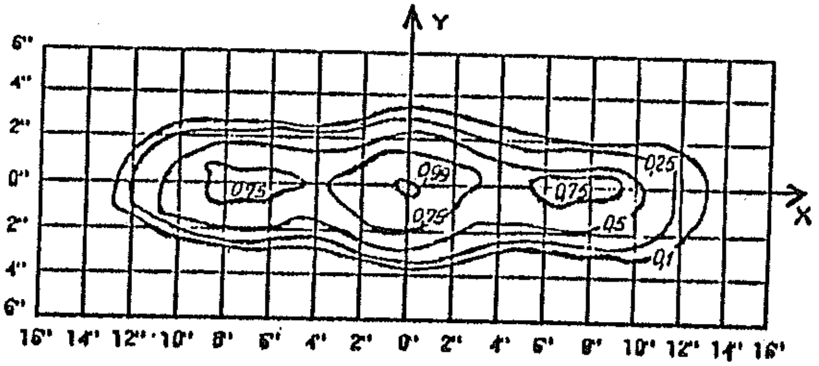

Fig.2. Retroreflector's reflection pattern at 13° light incidence. Reflection efficincy in maximum is 0.63.

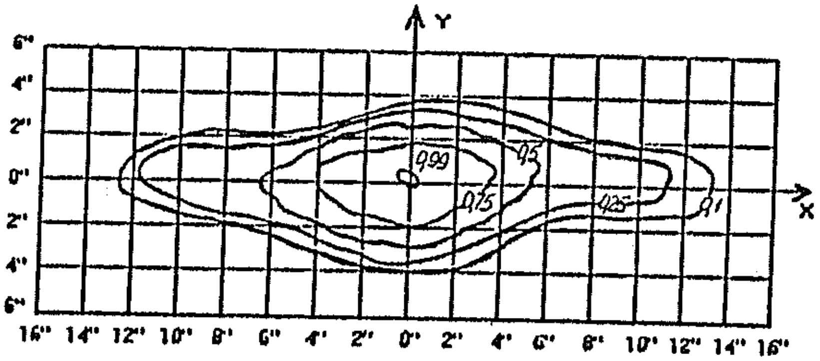

Fig.3. Retroreflector's reflection pattern at 20° light incidence. Reflection efficiency in maximum is 0.42.

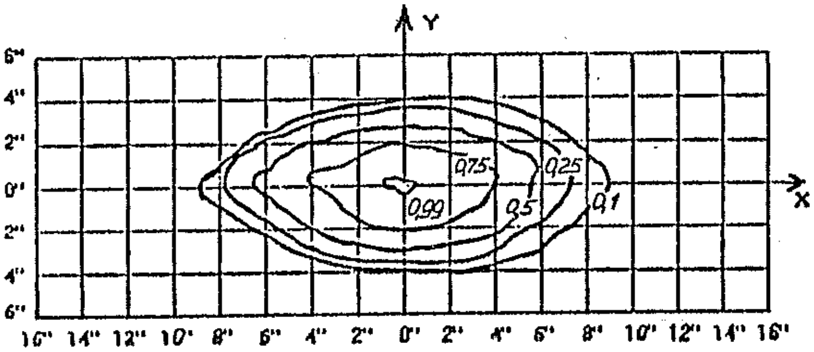

Fig.4. Retroreflector's reflection pattern at 30° light incidence. Reflection efficiency in maximum is 0.22.

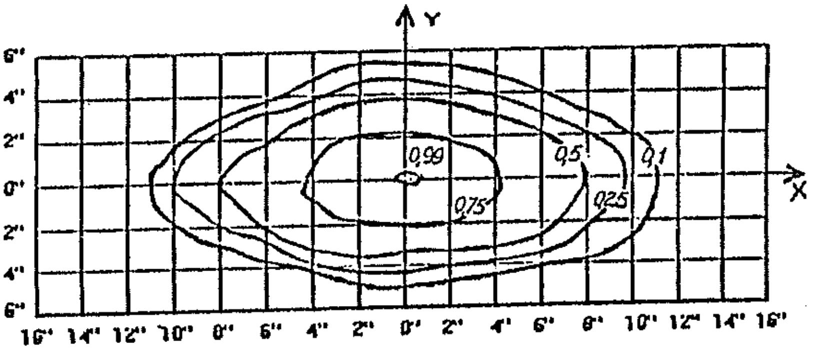

Fig.5. Retroreflector's reflection pattern at 40° light incidence. Reflection efficiency in maximum is 0.04.

Tenth International Workshop On Laser Ranging Instrumentation, 11-15 November 1996, ShangaV, China

THE POLARIZATION BEHAVIOUR OF CUBE CORNER RETROREFLECTORS USED IN SLR SATELLITES

M. Kasser, ESGT / CNAM, 18 Allée Jean Rostand, 91 025 EVRY Cedex, France
Fax : +331 69 36 74 21
B. Goupil, LOEMI / IGN, BP 68, 94 160 Saint-Mandé, France

INTRODUCTION

We have investigated new techniques to perform distance measurements between the SLR station and a satellite, and among them one requires to know the change of polarization of a laser beam due to the reflection on a cube corner retroreflector (CCR). This paper relates the results, both theoretical and experimental, that may help to understand the effect of CCR. The situation is considerably complicated by the fact that the CCR used in geodetic satellites have no reflecting coating on the back faces, so as to avoid CCR whose front face are far from the laser direction (typically more than 20E) of being active. In this case, the successive reflections on a dioptre not far from the limit angle induce a strong additional ellipticity (which is not the case with metallic coatings). Thus we have computed what happens for (i) a linear polarization and (ii) a circular polarization at various incidence angles, and we have checked some results with limited experimentations : The discrepancies are very limited, but we have not been able to find a good explanation for them.

POLARIZATION OF THE LIGHT AND TOTAL REFLEXION ON A DIOPTRE

If we consider the electric field **E** of an electromagnetic wave, **E** is perpendicular to the direction of propagation, and for its components E_x and E_y, a comprehensive way to describe the polarisation will be to use the 4 Stokes parameters (2) :

$$\begin{aligned} s_1 &= E_{ox}^2 + E_{oy}^2 \\ s_2 &= E_{ox}^2 - E_{oy}^2 \\ s_3 &= 2\, E_{ox}\, E_{oy} \cos(\Delta_y - \Delta_x) \\ s_4 &= 2\, E_{ox}\, E_{oy} \sin(\Delta_y - \Delta_x) \end{aligned}$$

with :

$$\begin{aligned} E_x &= E_{ox} \,.\, \cos(\omega t - \Delta_x) \\ E_y &= E_{oy} \,.\, \sin(\omega t - \Delta_y) \end{aligned}$$

The interaction with a dioptre may be modelled by the so-called Mueller matrix (ref. 1 et 2), acting on the Stokes parameters, the main computation problem being to check carefully the reference frame changes between each reflection. We have chosen to display the results on the Poincaré sphere, on which :

- The latitude angle is the Arctg of the ellipticity.

- The longitude is the orientation of the main axis of the ellipse.

For example the two circular polarisations are the two poles, and on the equator we find linear polarisations.

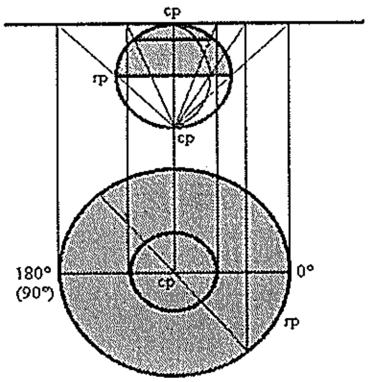

cp: circular polarization
rp: rectilinear polarization

Figure 1 : Polar stereographic projection of the Poincaré sphere

The results of our computations are displayed using a polar stereographic projection, generally limited to the upper hemisphere : the largest circle represents the equator and thus, linear polarisations, and the central point represents the upper ("North") pole and thus a circular polarisation.

THEORETICAL COMPUTATIONS

We have first defined a reference frame linked to the RCC, each of the Ox, Oy and Oz axis being the intersection of two reflecting faces. The optical problems due to the crossing of the front dioptre have been neglected, as the incidence angles are low and the induced additional ellipticity seems very small.

The direction of the incident ray is provided through 2 angles :

- The angle between the incidence plane, normal to the front dioptre, and a reference plane (including Ox) also normal to the front dioptre : the azimuth.

- The angle, within this incidence plane, between the incident ray and the normal to the front dioptre : the angle of incidence.

For each situation, we have six possible enchainments of faces, that are never commutative. The only simplifications of a systematic analysis of all directions are, in circular polarisation :

- a 120E rotation on the azimuth reproduces the same pattern,

- a symmetry relative to each of the three planes normal to the front dioptre and containing Ox, Oy or Oz provides a symmetric pattern.

The computations have been performed in C language, on a workstation, and some experiments have been performed in order to check the results. The one presented here (Fig. 3) is with a zero "incidence" and "azimuth" angles, in linear polarisation with the polarisation plane at 45E, 65E, 90E and 135E from the incidence plane. The experimental and theoretical curves (obtained by rotating a polarizing plate from 0 to 360E on the exit ray, the abscissa of the plot) show a small discrepancy that we could not explain completely, but which is not critical. The experimental device is the following (Fig. 2) :

Figure 2 : Experimental device for a null incidence over the front plane of a glass CCR

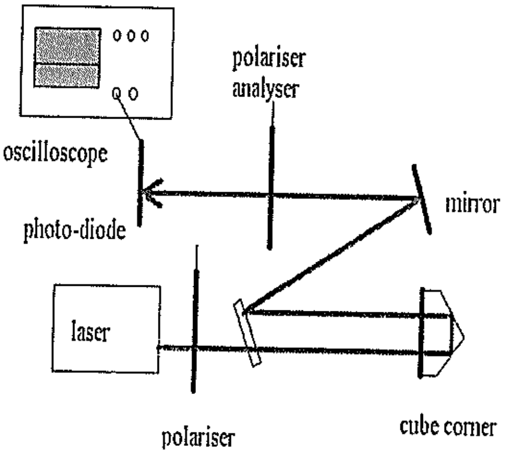

We present here the curves for 45° (Figure 3) :

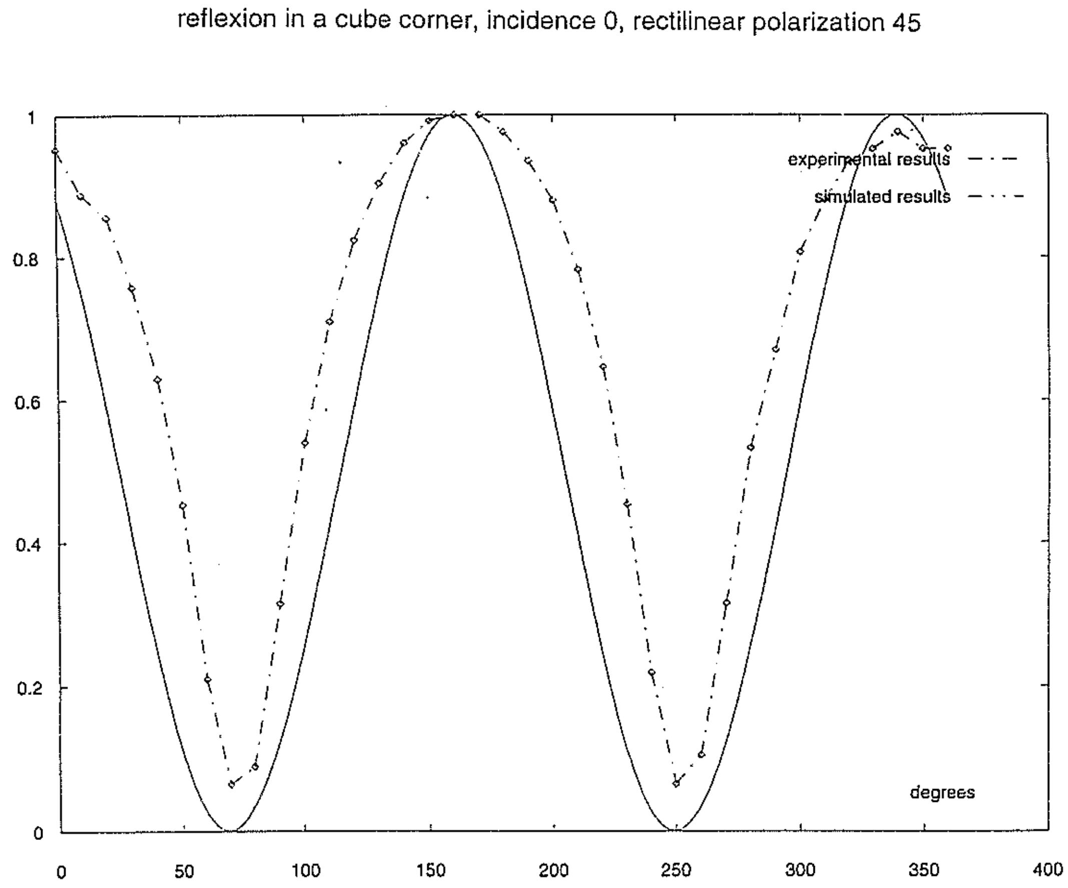

reflexion in a cube corner, incidence 0, rectilinear polarization 45

RESULTS, AND CONCLUSIONS

Two series of results are proposed (next page), the first for an entering ray in circular polarisation, the second with linear polarisation. In each case the azimuth is given, the incidence angle varies from +13° to -13° (larger angles are useless because one of the reflections is no longer total).

The six enchainments of faces are always presented, but one has to remember that with SLR, in order to cancel the aberration due to the relative movement of the satellite and the station, all CCR are spoiled so that only one enchainment of faces is used at a time, for applications where the far field only is useful. But it is clear that in static applications, the six enchainments of faces produce a set of six different images where it generally does not exist any pair having exactly the same polarisation. This is an interesting optical situation as, on another hand, these six images are theoretically in the same wave plane.

When the incidence angle is low, the major conclusion is that **one enchainment of faces behaves not far from a quarter-wave plate**. But this is just a coarse approximation, and everyone may see that results vary very quickly in some geometric configurations.

We present here a large number of representations, under various situations. The main conclusion is that not metalled CCR are providing extremely complicated polarisation patterns in general. For SLR applications, we are lucky that only one enchainment of faces is simultaneously active. Nevertheless our results mean that it is not advisable to use laser modulation based upon polarisation modulation, as just a small variation of the incidence (which is impossible to control) creates strong modifications of the resulting polarisation.

Thus we propose to continue experiments with long laser pulses, modulated at a very high frequency, in a quasi-continuous mode, but with devices where polarisation of the return beam is not critical.

BIBLIOGRAPHY

(1) **Born M., Wolf E., 1965**. Principles of optics, Pergamon press

(2) **Clarke D., Grainger J.-F. 1971**. Polarised light and optical measurement, Pergamon press

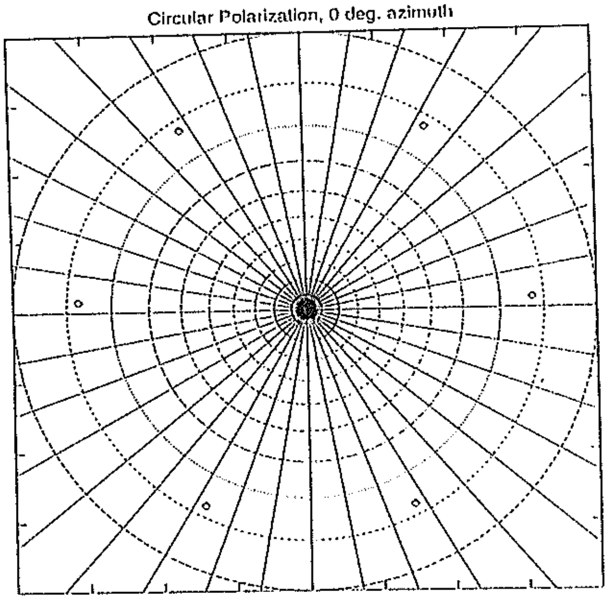
Circular Polarization, 0 deg. azimuth

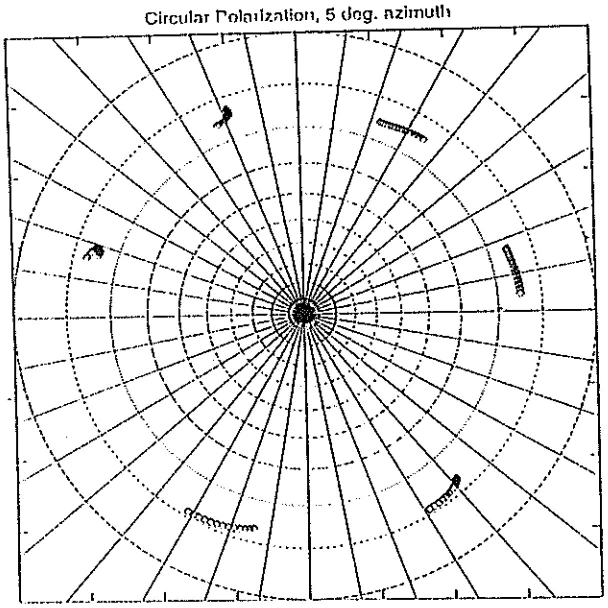
Circular Polarization, 5 deg. azimuth

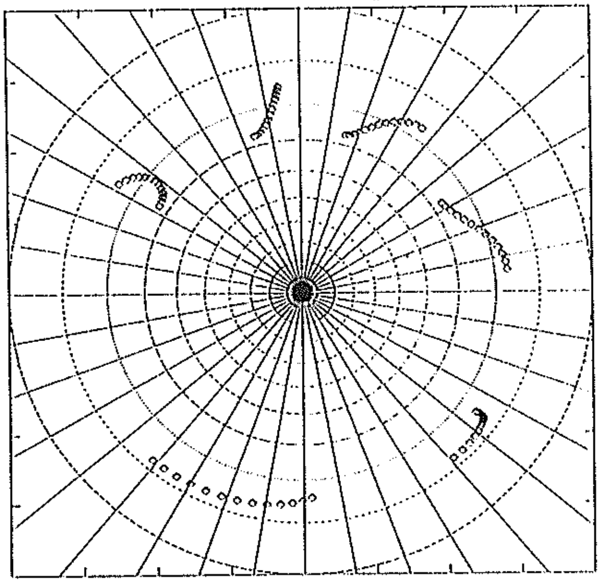
Circular Polarization, 10 deg. azimuth

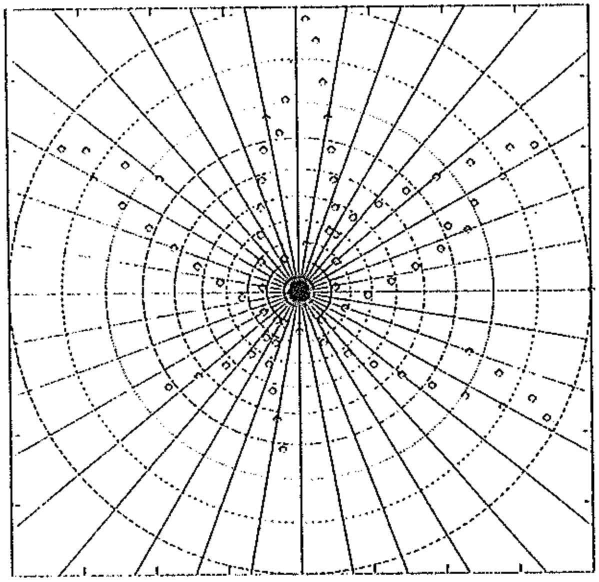
Vertical Polarization, 0 deg. azimuth

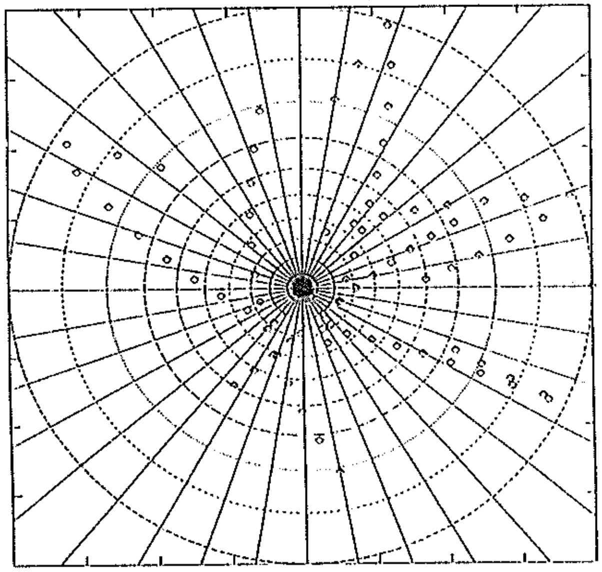
Vertical Polarization, 5 deg. azimuth

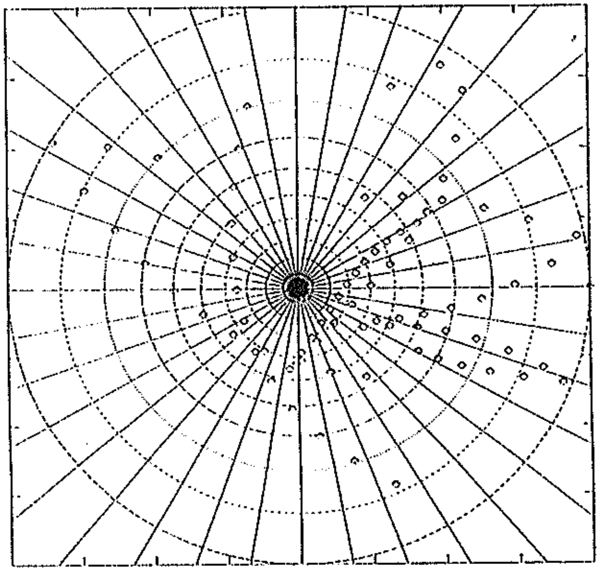
Vertical Polarization, 10 deg. azimuth

EUROLAS Cluster Stations

Bias Workshop Results

G. Kirchner, F. Koidl
Institute for Space Research / Austrian Academy of Sciences
Observatory Lustbühel; A-8042 GRAZ / AUSTRIA

1.0 Introduction

During an EUROLAS meeting in spring 1996 at RGO, a small bias workshop in Graz was initiated, where

- all possible sources of SLR measurement biases should be discussed;
- tests and experiments should be initiated to detect/verify biases;
- methods should be suggested to ensure that all participating SLR stations deliver high quality, bias-free data products.

We tried to include all possible error sources, including calibration, start pulse detection, stop pulse detection, counters, air condition problems, meteorology, software etc.; this paper does not contain a complete list of all these items, but will show a few selected results only.

2.0 Meteorology

The most critical - and most difficult to calibrate - meteorological item is the barometric measurement; air temperature and humidity are of much less importance, or easy to verify. To enable an absolute calibration/comparison of barometric measurements, we suggested to send a calibrated, electronic barometer with remarkable accuracy and resolution on a round trip to the stations, for comparison with the local standards.

We organized a ParoScientific 740 Laboratory Standard - as a Demo device - from a German company (Althen), and sent it to RGO, Potsdam and Wettzell; all comparisons at these stations and in Graz resulted in maximum differences of below 0.1 hP.

Most stations use only one set of meteorolgical values, taken somewhere before or after a pass, which is applied then to all returns of the full pass; reaching now sub-cm accuracies, it is recommanded to take meteorological values more often (e.g. before AND after the pass) and to interpolate between these points for each range measurement.

Meteorological sensors should be read by computer only, to avoid observer errors; if possible, all meteorological values should be checked at least for plausibility, continuity etc.

3.0 Counters

Most counter problems can be detected easily with a MultiCounter system, as it is operational in Graz [1]; as a conclusion, we strongly recommand the use of at least a second counter for control/verification/improvement of the main counter.

As stated in [1], do not daisy-chain the external reference frequency for multiple counters; this might cause additional, hardly detectable biases.

Most counters have significant temperature problems (our HP5370A shows a drift of about 40 ps/°C of the cooling air; the cooling air temperature might be quite different from the air condition temperature [1]); besides using counters in stabilized environment only, never switch off counters, to avoid warm-up problems, which might last for more than 1 hour.

4.0 Receiver

The main error source for SPAD systems is time walk due to different received energy; the best way to avoid this error is the use of time walk compensation circuits [2]; another way is to keep the return rate below the quantum efficiency (e.g. 20%); although this is an easy solution, it has some significant disadvantages:

- It reduces the amount of possible measurements by at least a factor of 5;
- Only the average return energy is at single photon-electron level; due to fluctuations there are still considerable multi photon-electrons present (although the major part of time walk will be cancelled out if calibration uses the same return energy);
- At single photon-electron level, the full satellite signature is present, and decreases single shot accuracy.

5.0 Calibration

It was recommanded to use short distance targets only (a few meters maximum) for calibration [3]; it is much easier to measure short distances to the mm-level or below; any meteorological influence is virtually eliminated (for a few 100 m target distance, this could be up to a few mm).

It was also recommanded to use at least 2 different targets, to avoid any specifics of a single target; any bias introduced by a single target could thus be detected easily; examples for such target specifics are target distance, one single, selected time only (Counter problems, HF-noise at that time etc.), direction dependence, fixed gate/return pulse relationships etc.

Any changes of the configuration between calibration and ranging should be avoided (like insertion of attenuation filters etc.).

6.0 Post-Processing Software Checks and Comparisons

Most of the EUROLAS stations use their own software for post-processing, Normal-Point calculations etc.; we wanted to make sure that these different software packages really produce the same results. Graz offered therefore to recalculate the Normal Points of various stations, using the Graz software, and compare the results with the NPs calculated at the stations (Fig. 1). If both calculations give similar numbers, this should be a good indication that both the stations software and the Graz software work correctly.

For all stations, we performed this comparisons for the raw data sets (as read from counters) and for MERIT-2 data sets; we have extended now also - on request - such comparisons for other stations outside EUROLAS, and we are offering such a quick check to anybody who is interested.

Fig. 2 shows a typical result of such a NP comparison with Potsdam Lageos data; the differences are typically far below 1 mm (6.6 ps), with no systematic offsets; due to complete diffferent methods (Graz uses e.g. polynomial fitting to residuals only, without any orbit analysis), the results cannot coincide exactly within the ps, but show that both methods deliver NP's coinciding to sub-mm. Slightly higher deviations at begin and end of the pass are usually due to small oscillations of polynomial fitting procedures of the Graz software.

Fig. 3 shows comparisons with RGO Normal Points; the slope is due to a difference of 40 ps between pre- and post-calibration: The RGO software uses the mean value, while the Graz software interpolates linearly between pre- and post-calibration for each return epoch. Besides this slope, the NP's coincide very well, except at begin and end, due to the Graz polynomial fitting procedures, and due to low number of points per NP here.

The MTLRS-1 data set (Fig. 4) shows the strong influence of the SPAD data skew; without any editing, the NP's coincide quite well, but the Peak-Minus-Mean of the data set is high (-8.9 mm); using a 2.2-sigma editing, this is reduced to -4.2 mm, but the mean values of the NP's are shifted now by more than -7 mm; to reduce this effect, it is important to handle both ranging and calibration data in exactly the same way; to eliminate it completely, the SPAD should be operated with higher Voltage above break (10 V instead of 2.5 V), using Time Walk Compensation Circuits; it is then possible to get Zero Peak-Minus-Mean [3]. MTLRS-1 will therefore consequently be upgraded with the full Graz Detection Package.

The Grasse Lageos-1 pass (Fig. 5) showed obvious problems; the NP differences were fluctuating randomly between +2 cm and -1 cm; the reason was an error in the Grasse software [4], which was detected and corrected; the comparison with the corrected data set shows that the error is eliminated completely now (Fig. 5).

References:

[1] MultiCounter Operation at SLR Graz. G. Kirchner, F. Koidl; in these Proceedings.
[2] Automatic SPAD Time Walk Compensation. G. Kirchner, F. Koidl; in these Proc.
[3] Short Distance Calibration. G. Kirchner, F. Koidl; in these Proceedings.
[4] F. Pierron, personal communication.

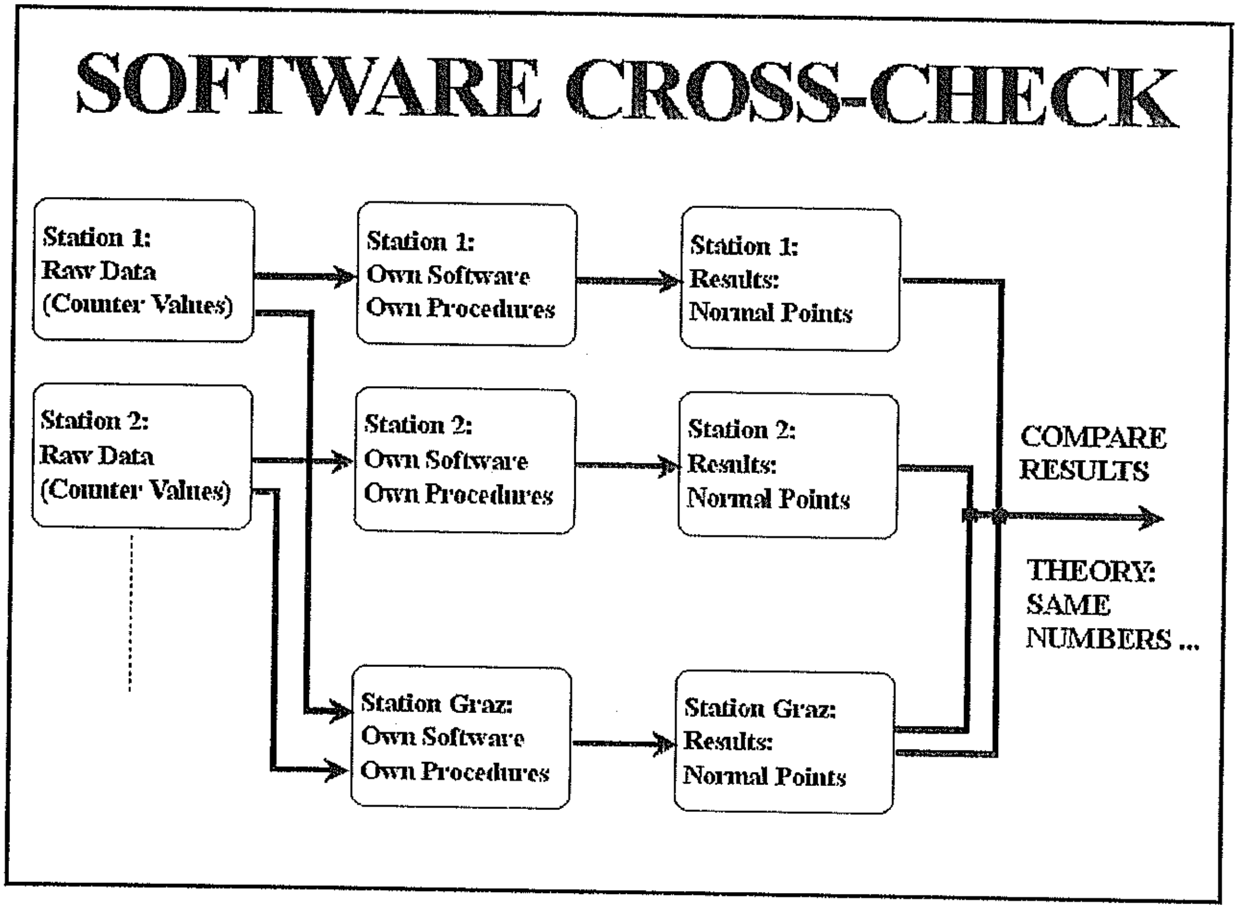

Fig. 1: Post-Processing Software Cross-Check Scheme

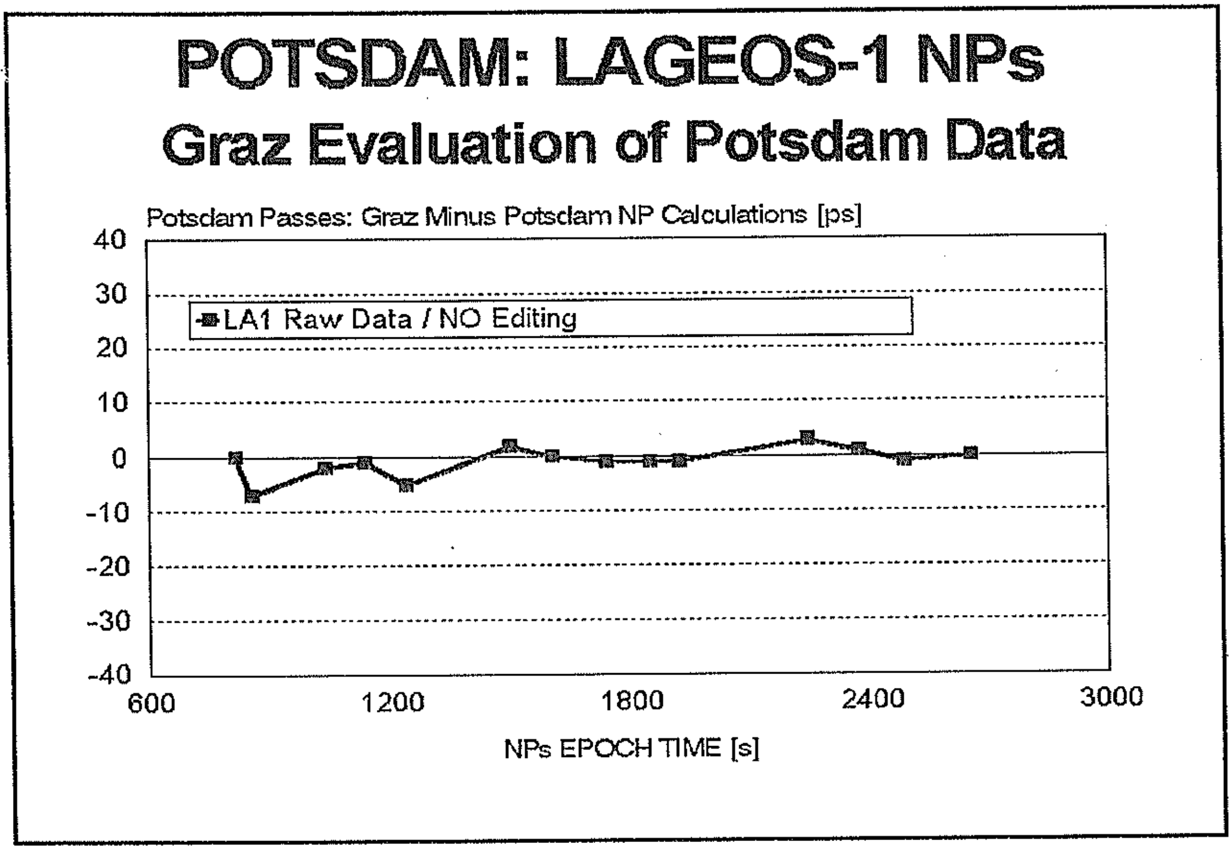

Fig. 2: Software Cross-Check: Potsdam LAGEOS-1 Raw Data

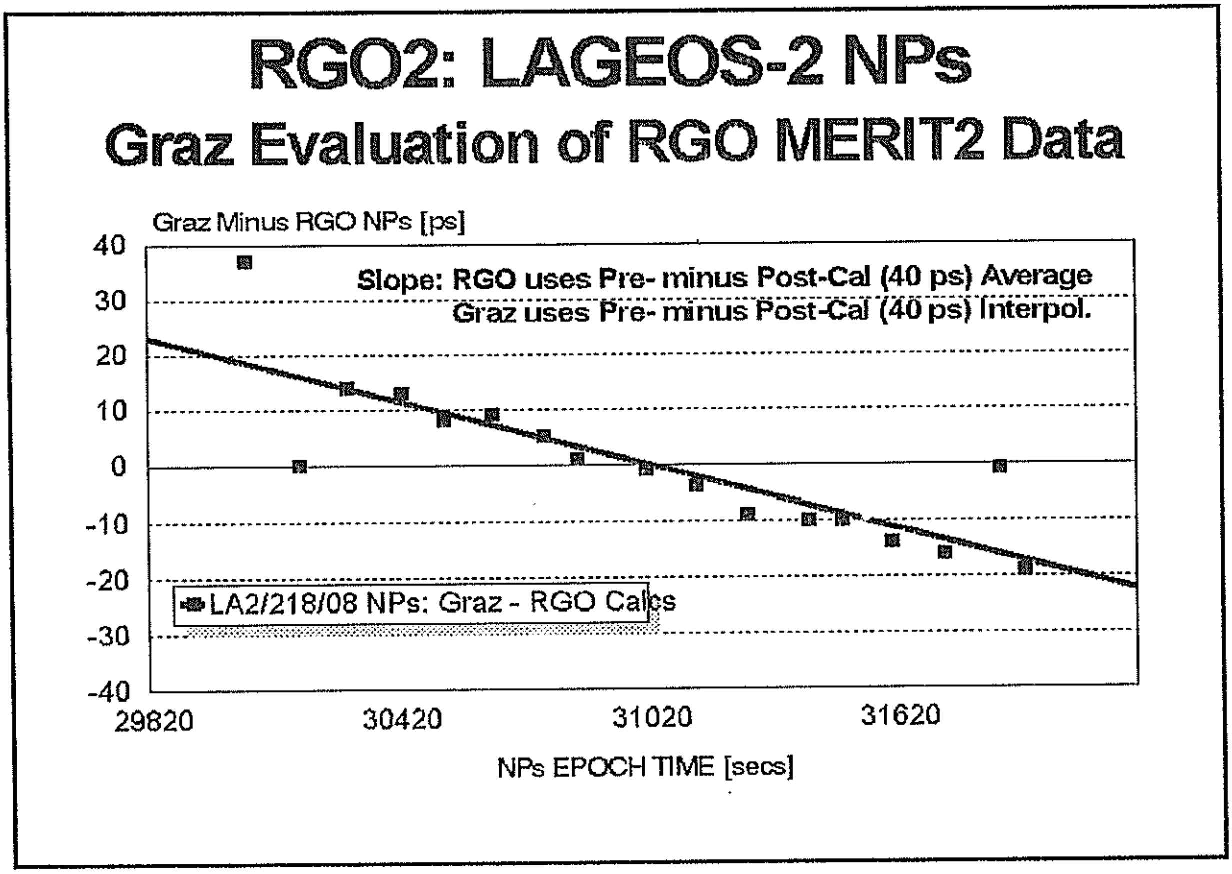

Fig. 3: Software Cross-Check: RGO LAGEOS-2 MERIT-2 Data

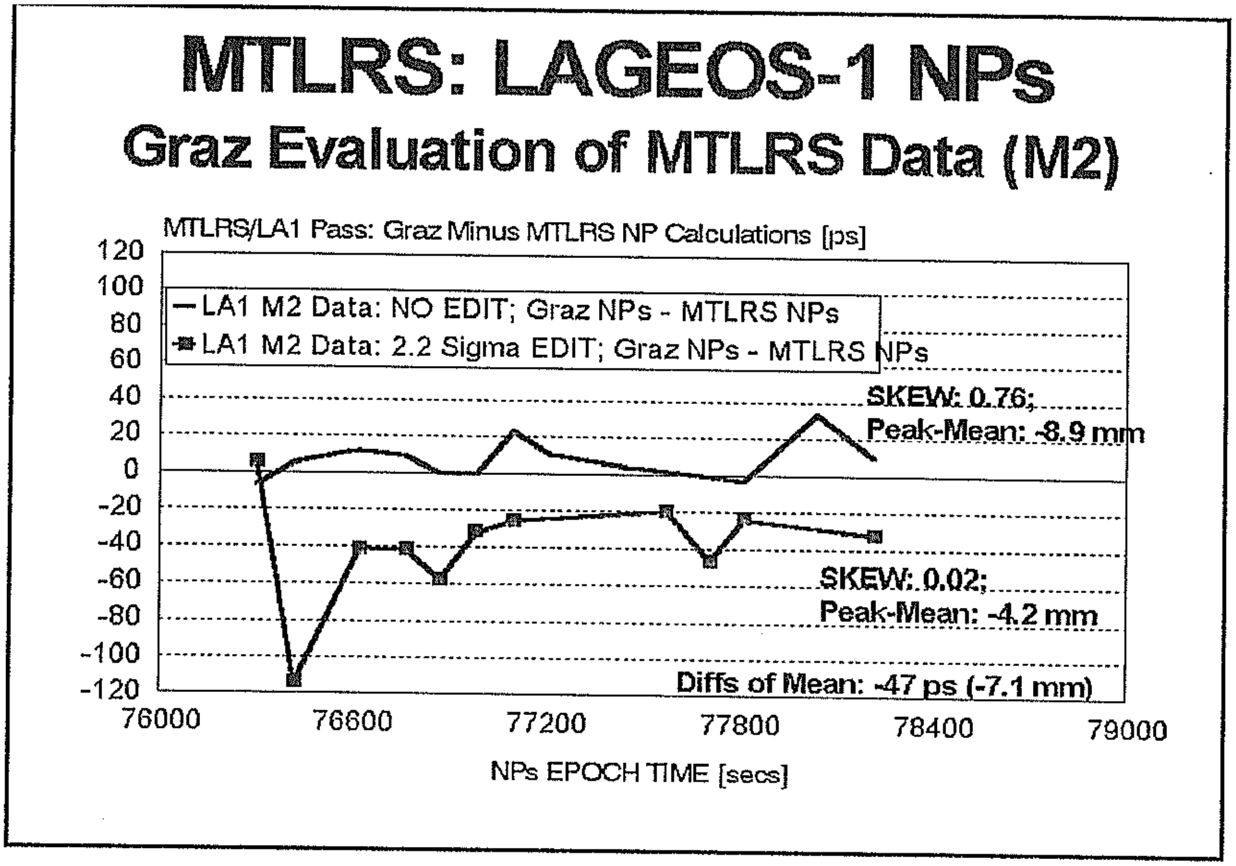

Fig. 4: Software Cross-Check: MTLRS-1 LAGEOS-1 MERIT-2 Data

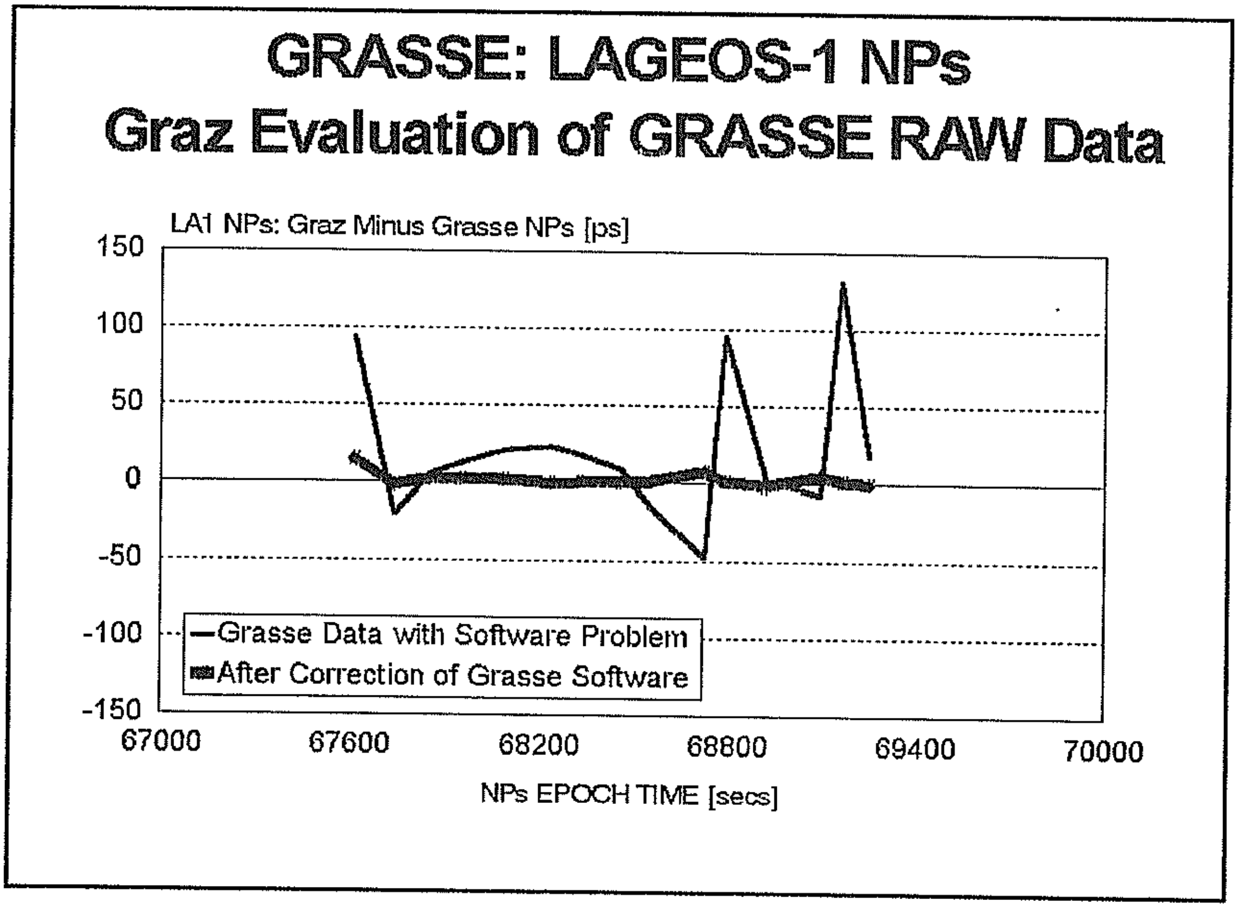

Fig. 5: Grasse LAGEOS-1 Raw Data, before / after Correction of Grasse Software

Detectors

and

Spectral Filters

The Performance Test of F4129f MCP-PMT in Changchun Station

Liu Zhi, Zhao You, Zhang Xinghua, Fan Cunbo
Changchun Artificial Satellite Observatory

The current paper presents the ranging results of both calibrating ground-target by using 3 different voltage dividers for F4129f MCP-PMT and ranging to satellites. The single shot range precision estimation is improved from 5-7cm (rms) to less than 3cm (rms).

1. Introduction

The single shot range precision of Changchun SLR was designed 5-7cm, and it has been this precision for many years. In order to follow the development of international SLR network, in 1994 we proposed a research plan to improve our SLR range precision, its target was: the single shot range precision to Lageos was better than 2cm. According to the situation of our SLR system, we chose the F4129 microchannel plate PMT, the product of ITT company, as photo-electronic detector, through more than one year test, we obtained the results of ranging to satellite.

The detector F4129 was the main device of this experiment, so we designed 3 kinds of voltage dividers which were suitable for F4129 device work ,and selected the best work condition for F4129 by ground target calibration. We chose voltage dividers and used it to range to satellites, the results of ranging to Lageos ware better than 2cm. The results of ranging to loworbit satellites were better than 2.5cm.

2. The Results of Ground Target Calibration

2.1 The principle diagram of calibration of ground target experiment

It is a simple and practicable way for us to select the best work condition of optic-electronic detector by calibration of ground target, simulating the strength of the satellite return signals, we drew up the calibration diagram, shown in Fig. 1.

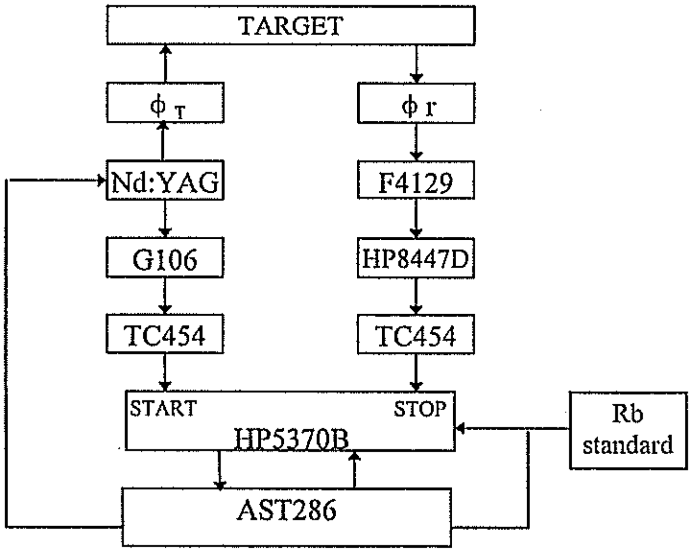

Fig.1 Scheme diagram of calibration

2.2 The structure and characteristics of 3 kinds of voltage divider

According to the characteristics of F4129, we designed 3 voltage dividers, whose structures and characteristics were as follows:

No.1 voltage divider:
structure: Pi pole connected to ground, powered by positive and negative voltage
characteristics: high gain

No.2 voltage divider:
structure: A pole connected to ground, powered by high negative voltage
characteristics: coupled directly, high gain

No.3 voltage divider:
structure: Pi pole connected to ground, powered by positive and negative voltage
characteristics: with negative feedback current, low gain

2.3 The condition for calibration ground target

The condition for calibration of ground target for 3 voltage dividers kept the same: the laser pulse width 220 ps; the laser output energy around 100 mj; the stability of rubidium standard 2×10^{-12} per day; the trigger level of 5370B counter -0.35v; the same constant fraction discriminator;

2.4 The results of calibration

The 3 voltage dividers were used to ground target calibration under above conditions, the results are shown in table 1, 2 and3. Table 4 is the calibration results of No.3 voltage divider simulating satellite dynamic echoes.

Table 1

OPE. Vol(v)	mean. (μs)	ξ (%)	rms (cm)	φ t	φ r	tem.(℃)
2900	8.588752	70	3.1	20	0.2	8
2950	8.588645	84	2.6	20	0.2	8
3000	8.588563	90	2.0	20	0.2	8
3100	8.588427	93	1.9	20	0.2	8
3200	8.588372	97	1.4	20	0.2	8

Table 2

OPE. Vol(v)	mean. (μs)	ξ (%)	rms (cm)	φ t	φ r	tem.(℃)
-2900	8.598611	20	4.0	20	0.2	10
-3000	8.589761	22	3.6	20	0.2	10
-3100	8.589214	30.1	3.0	20	0.2	10
-3200	8.588382	46.1	3.6	20	0.2	10

Table 3

OPE. Vol(v)	mean. (μs)	ξ (%)	rms (cm)	φ t	φ r	tem.(℃)
3100	8.589742	16	1.5	20	0.2	15
3100	8.589785	10	1.3	20	0.2	15
3200	8.589716	24.2	1.5	20	0.2	15
3200	8.589723	20.1	1.9	20	0.2	15
3300	8.589548	39.7	1.3	20	0.2	15
3300	8.589577	43.9	1.5	20	0.2	15

Table 4

OPE. Vol(v)	mean. (μs)	ξ (%)	rms (cm)	ϕ t	ϕ r	tem.(℃)
3200	8.582288	91.5	1.36	20	0.2	8
3200	8.582300	86.5	1.22	20	0.1	8
3200	8.582312	33.1	1.32	20	0.08	8
3200	8.582324	16.9	1.46	20×7	0.08	7
3200	8.582345	7.8	1.53	20×2	0.08	6

3. The Results of Satellite Ranging

According to the results shown in above tables, we selected No.3 voltage divider. In September 1995, we obtained some experimental data from satellites (in table 3). From table 3 we can see: the single shot range precision is better than 2cm to Lageos, and better than 2.5cm to loworbit satellites with No.3 voltage divider.

Table 3

LAGEOS-1		LAGEOS-2		ERS1		STARLETTE		AJISAI	
rms (cm)	obs	rms (cm)	obs	rms (cm)	obs	rms (cm)	obs	rms (cm)	obs
1.5	41	1.9	496	2.1	177	2.3	413	2.5	103
1.6	481	1.6	391			1.8	138		
		1.6	23						
		1.7	35						

4. Unsolved Problems

The gain and thermal noise problem of F4129 device

The data in table 3 show: the return rate of No.3 voltage divider is less than No.1 or No.2 voltage divider. When we use No.3 to satellite ranging, the work voltage of F4129 was close to its maximum work voltage; obviously, it is unacceptable for this device to work under its maximum voltage in long-term.

In order to improve the detector sensitivity, we tried to use two-stage amplifiers (HP8447D+HP8447E), but the noise increased, that is why we do not use it in our routine observation. We have ordered the pre-amplifier A-7 from No.13 Institute of Ministry of Electric Industry in China, its characteristics can meet our need. We hope the MCP-PMT receiver will be in operational in a few months.

References:

(1) ITT. Microchannel Plate Photomultiplier Tube Test Report Summary, 1991,1
(2) HP. 0.1-1300MHz Amplifier Operation and Service Manual
(3) The Products Manual of No.13 Institute of Ministry of Electronics Industry

Increasing System Sensitivity At LURE Observatory
or
How To Get GPS Data With A 400 mm (16 inch) Aperture Telescope

R. Zane, M. T. Maberry and D. J. O'Gara
University of Hawaii, Institute for Astronomy
LURE Observatory at Haleakala
P.O. Box 209
Kula, Maui, Hawaii, U.S.A.
E-Mail: zane@lure.ifa.hawaii.edu

Abstract: The overall system sensitivity was increased by modifying the Tennelec TC-454 discriminator to increase its input sensitivity and stability. An improved 532 NM narrow band filter with full width half maximum (FWHM) bandpass of 0.3 nm and 80% transmission was installed along with an adjustable field stop to regulate field of view. The resultant increase in system sensitivity allows regular acquisition of GPS satellites.

Introduction

Early attempts to increase system sensitivity involved using several different kinds of high speed pulse amplifiers to increase the pulse amplitude. No amplifiers were found which did not also introduce additional problems in the form of amplitude dependent phase shift or "time walk." It was also observed that amplification did not improve signal to noise ratio. It was then decided to approach the sensitivity problem by reducing losses, reducing noise while also increasing the input sensitivity of the TC-454 discriminator. Improvements were also made in the data acquisition software

Method

Constant Fraction Discriminators divide an input pulse into two components established by an attenuator network that has a fifty ohm impedance. One part is reduced by the fraction, F, while the other part is reduced by the fraction, (1-F). A typical value of F=0.2 is used in the Tennelec (Oxford Instruments) TC-454. In the TC-454, the fraction that is reduced by F is applied directly to the negative input of a fast, ECL, differential comparator (see schematic 4X038-S1). The fraction that is reduced by (1-F) is delayed slightly, so that its leading edge intersects the peak of the direct fraction, and applied to the positive input of the fast ECL differential comparator (see Figure 1). The difference appearing across the inputs of the comparator is shown in Figure 2. The comparator switches state when the difference passes through 0 volts. In principle the 0 volt crossing point is invariant in time as the input pulse amplitude changes. In practice, there are variations, both random and systematic, caused by noise, offsets in the comparator, and variations in the input pulse shape. Nonlinearities in the "timewalk" characteristic are especially noticeable for very low level pulses.

A Delayed Symmetry Discriminator applies the input pulse directly to the negative input of a fast ECL differential comparator. The same pulse is then delayed by the Full Width at Half Maximum (FWHM) of the input pulse and applied to the positive input of the differential comparator as shown in Figure 3. The difference appearing across the inputs of the comparator is shown in Figure 4. The comparator switches state when the difference passes through zero volts. The zero volt crossing occurs at the Half Maximum point on the trailing edge of the direct pulse and at the Half Maximum point on the leading edge of the delayed pulse. The improved time stability and resolution of the DSD technique are due to the higher amplitude and faster rate of change of the differential voltage at the input to the comparator.

It has been found that a slight modification to the standard TC-454 allows operation of the TC-454 in the DSD mode. The circuit changes are detailed in schematic 4X038-S2. It has also been found that disabling the "Z" adjustment, so that "Z" is always 0 volts, results in less variation in the timewalk characteristic of the TC-454. This is due to the fact that small changes in the power supply voltages in the NIBin result in changes of about 1 mV on the "Z" bias. The return pulse out of the MCP Photomultiplier is typically around 1 NS FWHM. Pulses of this width are approaching the response limit of ECL comparator circuits. The ECL comparator integrated circuit used in the TC-454 discriminator is manufactured by four companies. The specified response times of the four circuits are as follows:

Manufacturer	Part No.	Response Time
1. MAXIM	MAX9687	1.9 NS
2. Signal Processing Technologies	SPT9687	2.3 NS
3. Analog Devices	AD9687	2.7 NS
4. GEC Plessey	SP9687	3.0 NS

The MAXIM comparator integrated circuit was tested and found to produce lower rms error than the GEC Plessey or the Analog Devices circuits. The Signal Processing Technologies version of the comparator was not tested.

The DSD modified TC-454 discriminator has been operated for the past 11 months with a single discriminator section used for the "start" pulse and a single discriminator section used for the "stop" pulse. The single discriminator mode of operation results in a savings of about -6db in losses due to a splitter and delay cable. The "stop" discriminator threshold has been set at minimum adjustment, "T"= -50MV, which produces a measured threshold of approximately -20 millivolts. Figures' 5A and 5B illustrate the results of a calibration using the DSD modified discriminator for both the "start" and "stop" pulses. The linear "time walk" characteristic in the calibration has been corrected with software (see "Real Time Correction of SLR Range Measurements for the Return Amplitude Induced Bias of the Multi-Channel Plate PMT/TC-454 DSD Discriminator Receive System, D. J. O'Gara, et al).

The receive optics were redesigned in order to increase the transmission of the return pulse while at the same time reducing the amount of optical noise(see 4X038-L1 and 4X038-L2). A variable field stop (2 to 30 mm) was added at the focal plane of the +225 mm F.L. focusing lens to allow control of the field of view. A +25 mm recollimating lens produces a collimated beam of about 1.75 mm diameter. A turning mirror, of high reflectivity, then redirects the beam into a Barr Associates 0.3 nm FWHM narrow band 532.08 filter. The narrow band filter is rotated to a tilt angle of about 3.5 degrees in order to optimize transmission at 532.00 NM. The filter has a peak transmission of approximately 80%.

Great care was taken to reduce electrical noise throughout the system by implementing good grounding and shielding techniques wherever possible. It was found that unused sections of the TC-454 discriminator needed to be gated off with a terminator because if the gates were left open the discriminators oscillated. The NIBIN containing the TC-454 was moved to a point directly beneath the receiver in order to reduce cable lengths. The output of the MCP was terminated directly into a 50 ohm pulse splitter. One output of the splitter was connected through 1 meter of coaxial cable directly to the stop discriminator (DSD modified). The other output was connected through a long coaxial cable to an amplifier driving another splitter to provide a return pulse for the digitizing display and the pulse energy digitizer (REM).

Conclusions

The reduction in system noise sources and decreased signal loss produced a substantial increase in signal to noise ratio of the "stop" pulse from the MCP photomultiplier. The improved sensitivity and linearity of the DSD modified TC-454 also allowed operation of the "stop" discriminator at a minimum threshold voltage setting. The previous dynamic range of "stop" pulse, as measured at the TC-454 input, ranged from a maximum of 4.5 V-NS to a minimum of 0.25 V-NS (18 to 1). The current dynamic range is from a maximum of 4.5 V-Ns to a minimum of 0.03 V-NS (150 to 1). The increased sensitivity permits regular acquisition of the GPS satellites.

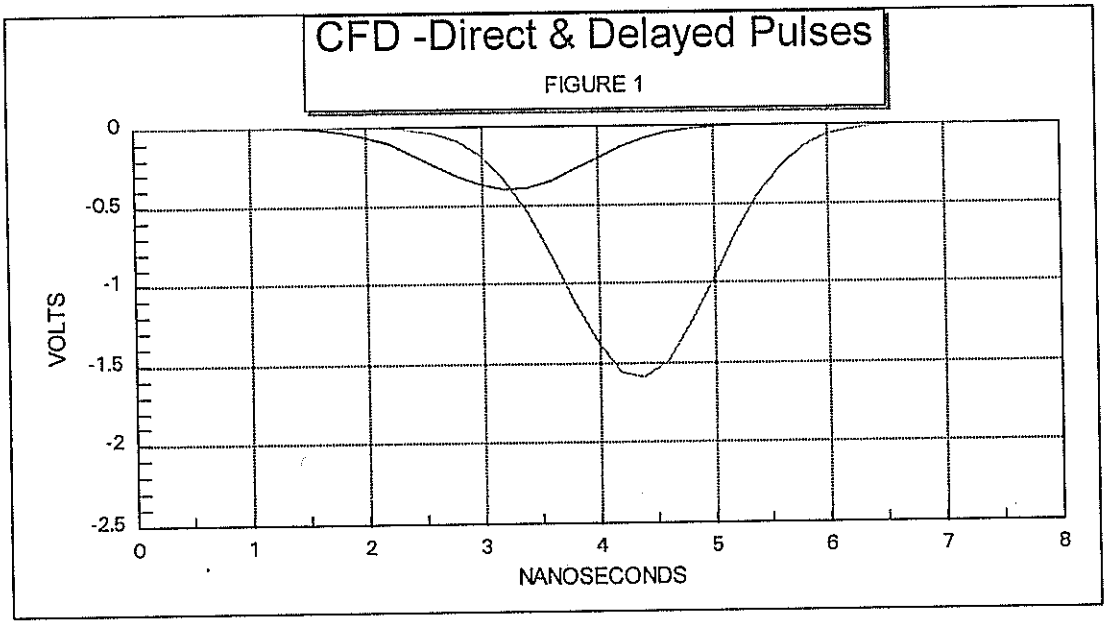

CFD -Direct & Delayed Pulses

FIGURE 1

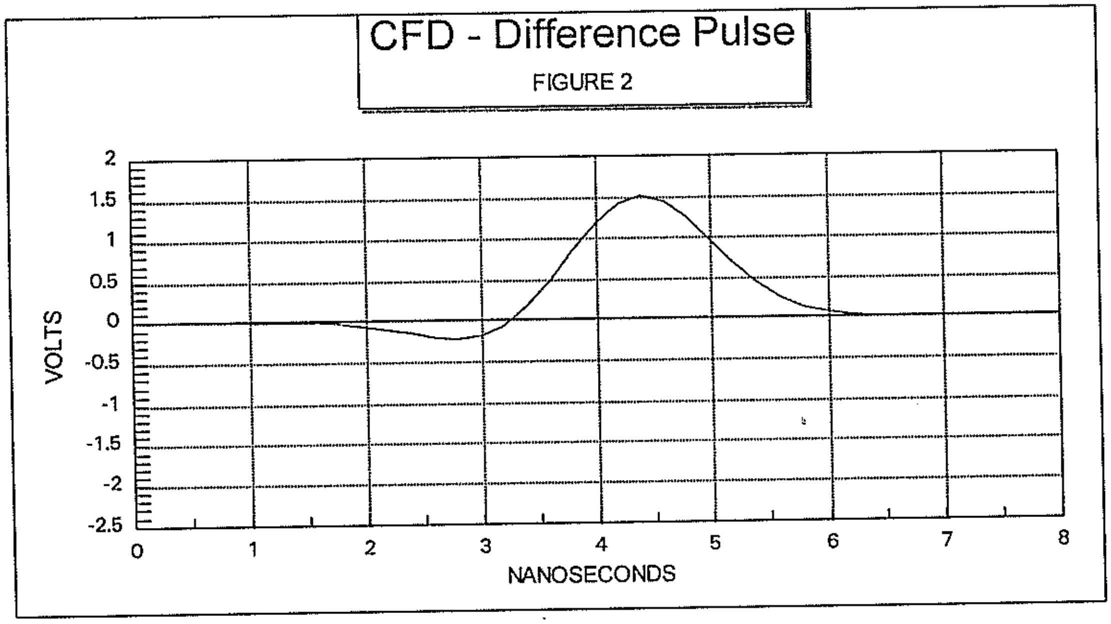

CFD - Difference Pulse

FIGURE 2

DSD - Direct & Delayed Pulses

FIGURE 3

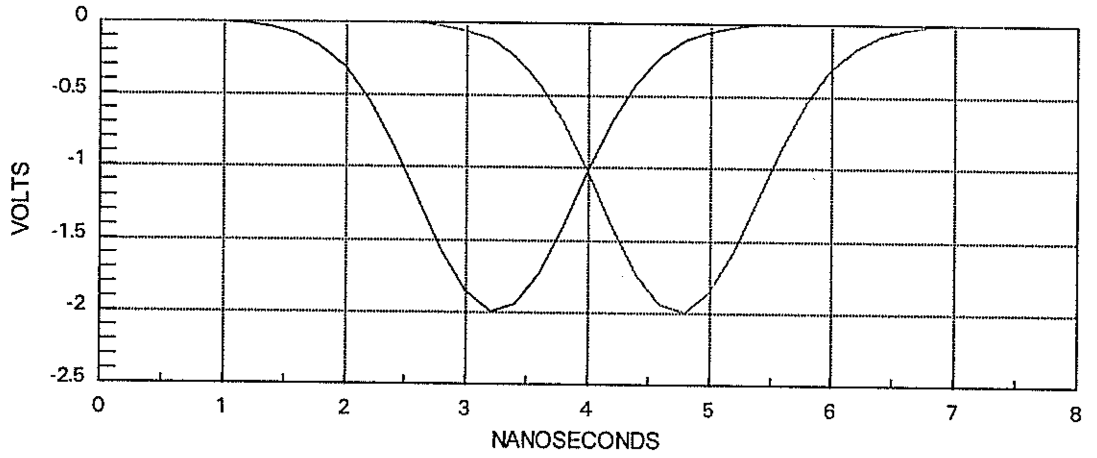

DSD - Difference Pulse

FIGURE 4

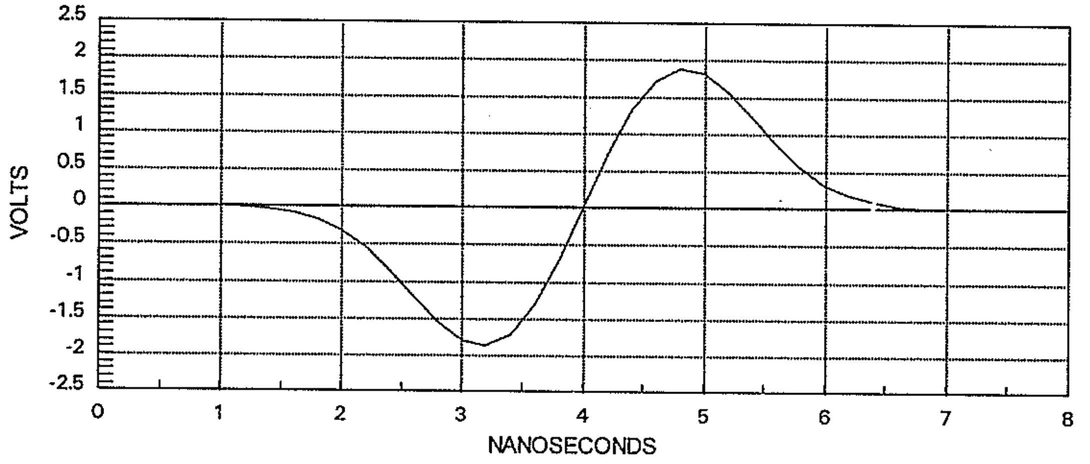

FIGURE: 5A
RESIDUAL VS REM# WITH LSQ FIT

INTERCEPT = 65.411 NS SLOPE =-2 PS/V*NS RMS = 6.27 MM

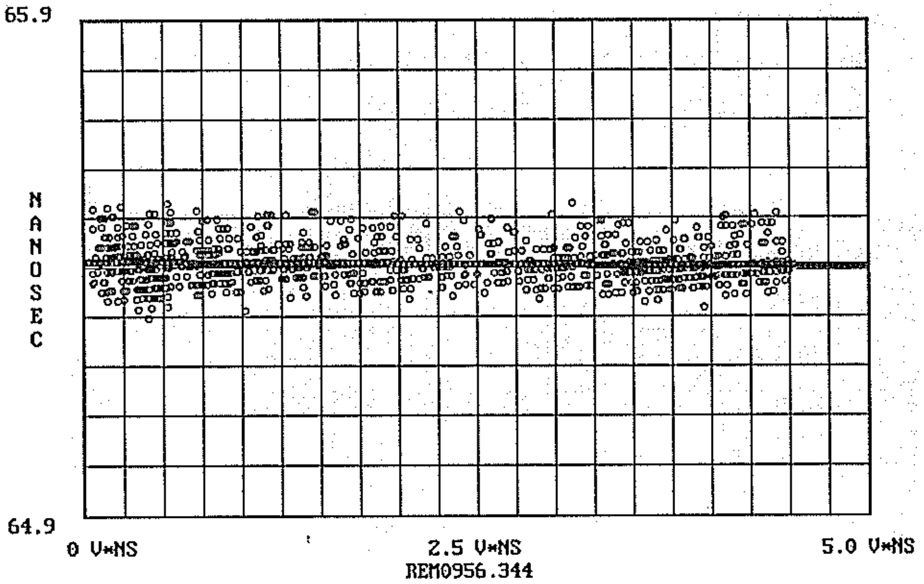

FIGURE: 5B
RESIDUAL VS REM# WITH LSQ FIT. MODULO 20

INTERCEPT = 65.411 NS SLOPE =-2 PS/V*NS RMS = 6.27 MM

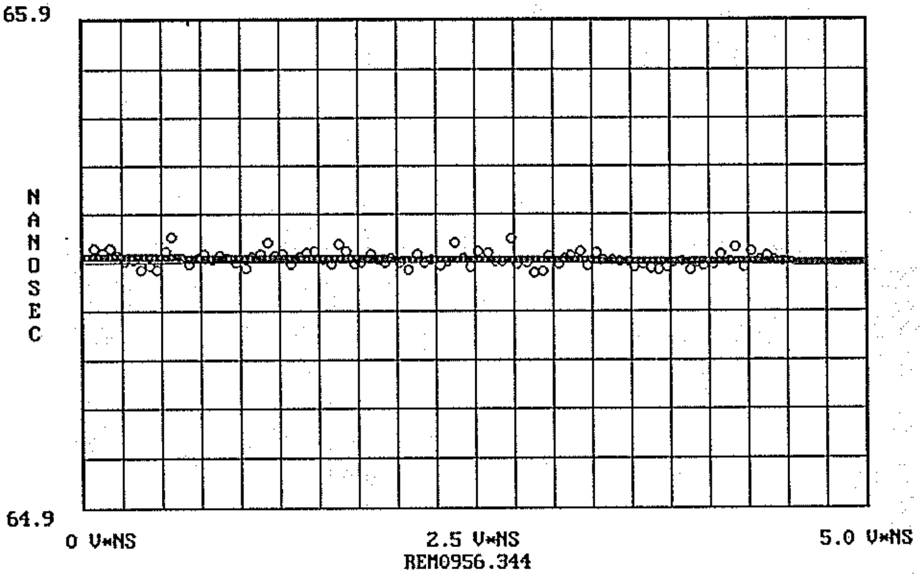

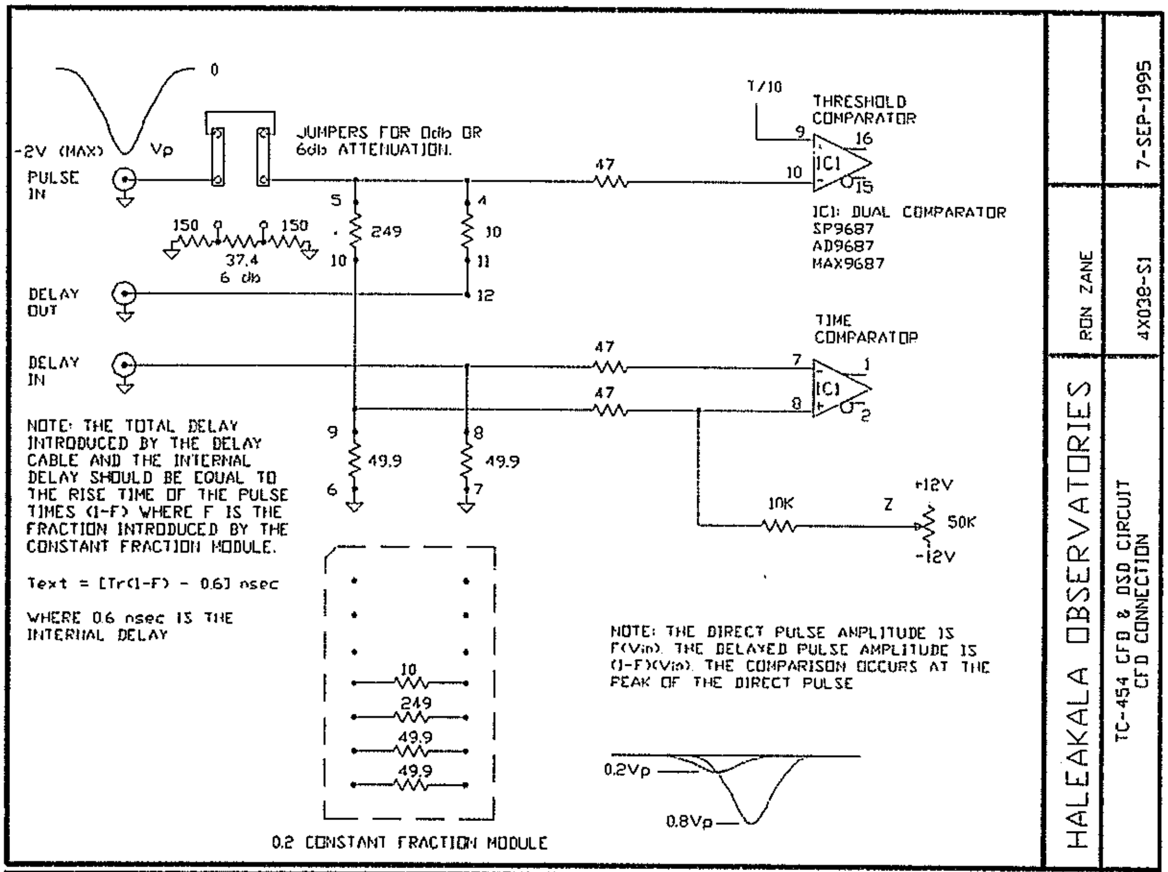

NOTE: THE TOTAL DELAY INTRODUCED BY THE DELAY CABLE AND THE INTERNAL DELAY SHOULD BE EQUAL TO THE RISE TIME OF THE PULSE TIMES (1-F) WHERE F IS THE FRACTION INTRODUCED BY THE CONSTANT FRACTION MODULE.

Text = [Tr(1-F) - 0.6] nsec

WHERE 0.6 nsec IS THE INTERNAL DELAY

NOTE: THE DIRECT PULSE AMPLITUDE IS F(Vin). THE DELAYED PULSE AMPLITUDE IS (1-F)(Vin). THE COMPARISON OCCURS AT THE PEAK OF THE DIRECT PULSE

HALEAKALA OBSERVATORIES

TC-454 CFD & OSD CIRCUIT
CFD CONNECTION

RON ZANE

4X038-S1

7-SEP-1995

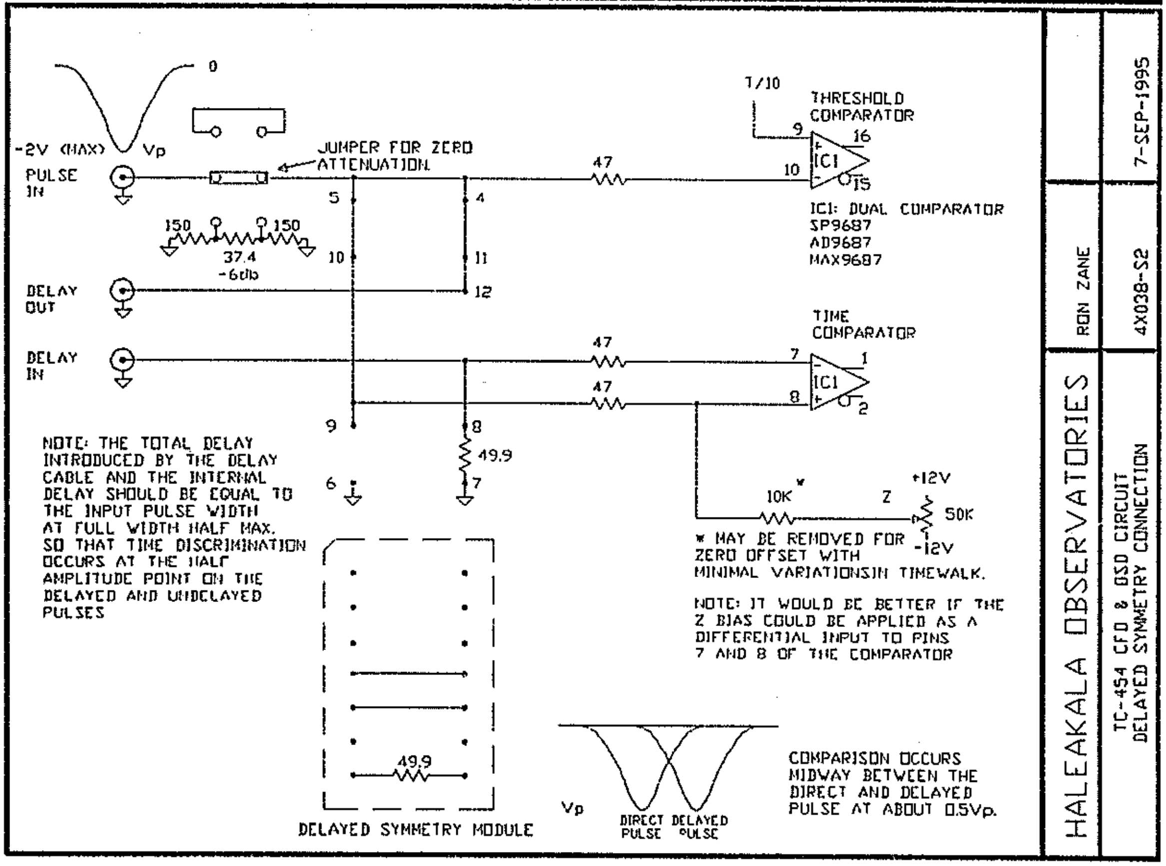

NOTE: THE TOTAL DELAY INTRODUCED BY THE DELAY CABLE AND THE INTERNAL DELAY SHOULD BE EQUAL TO THE INPUT PULSE WIDTH AT FULL WIDTH HALF MAX. SO THAT TIME DISCRIMINATION OCCURS AT THE HALF AMPLITUDE POINT ON THE DELAYED AND UNDELAYED PULSES

* MAY BE REMOVED FOR ZERO OFFSET WITH MINIMAL VARIATIONSIN TIMEWALK.

NOTE: IT WOULD BE BETTER IF THE Z BIAS COULD BE APPLIED AS A DIFFERENTIAL INPUT TO PINS 7 AND 8 OF THE COMPARATOR

COMPARISON OCCURS MIDWAY BETWEEN THE DIRECT AND DELAYED PULSE AT ABOUT 0.5Vp.

HALEAKALA OBSERVATORIES

TC-454 CFD & OSD CIRCUIT
DELAYED SYMMETRY CONNECTION

RON ZANE

4X038-S2

7-SEP-1995

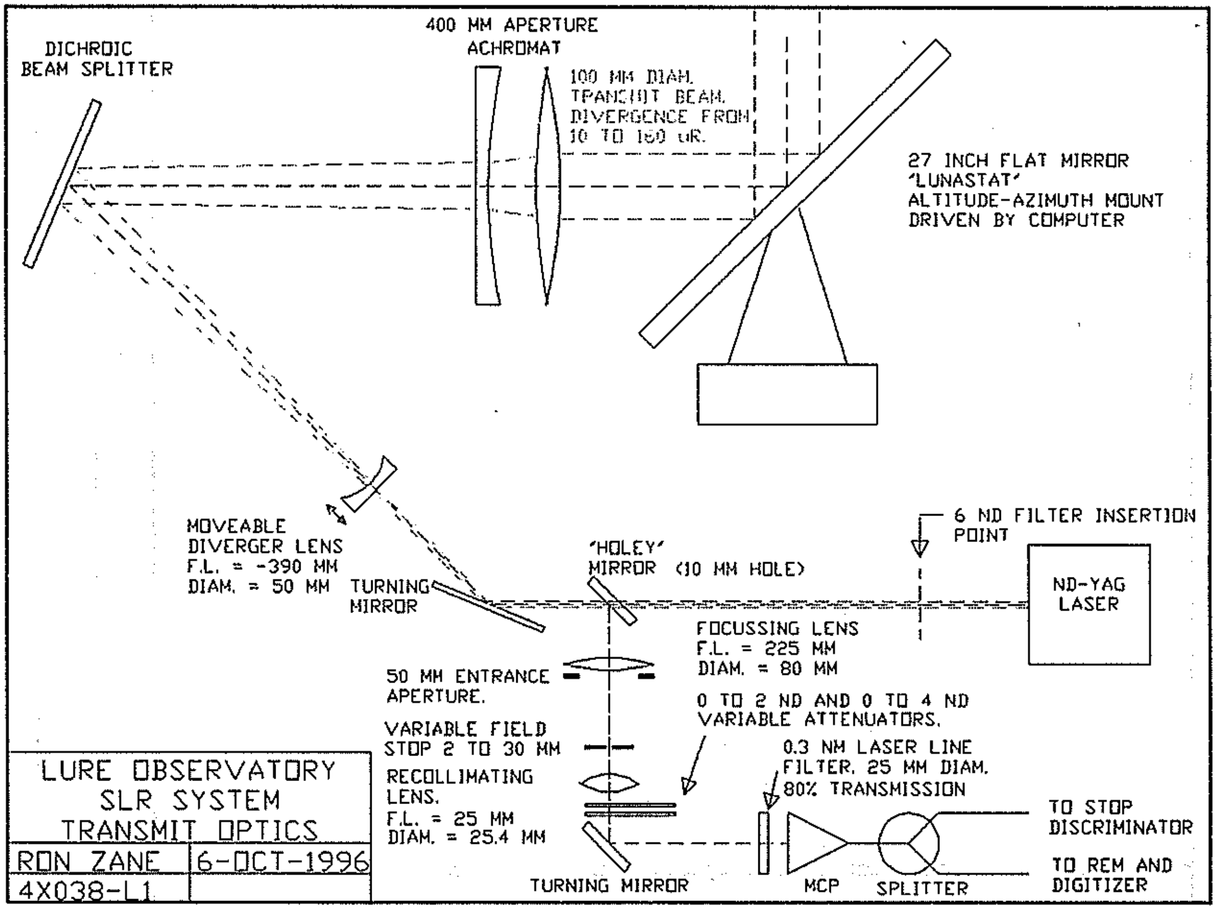

LURE OBSERVATORY
SLR SYSTEM
TRANSMIT OPTICS

RON ZANE	6-OCT-1996
4X038-L1	

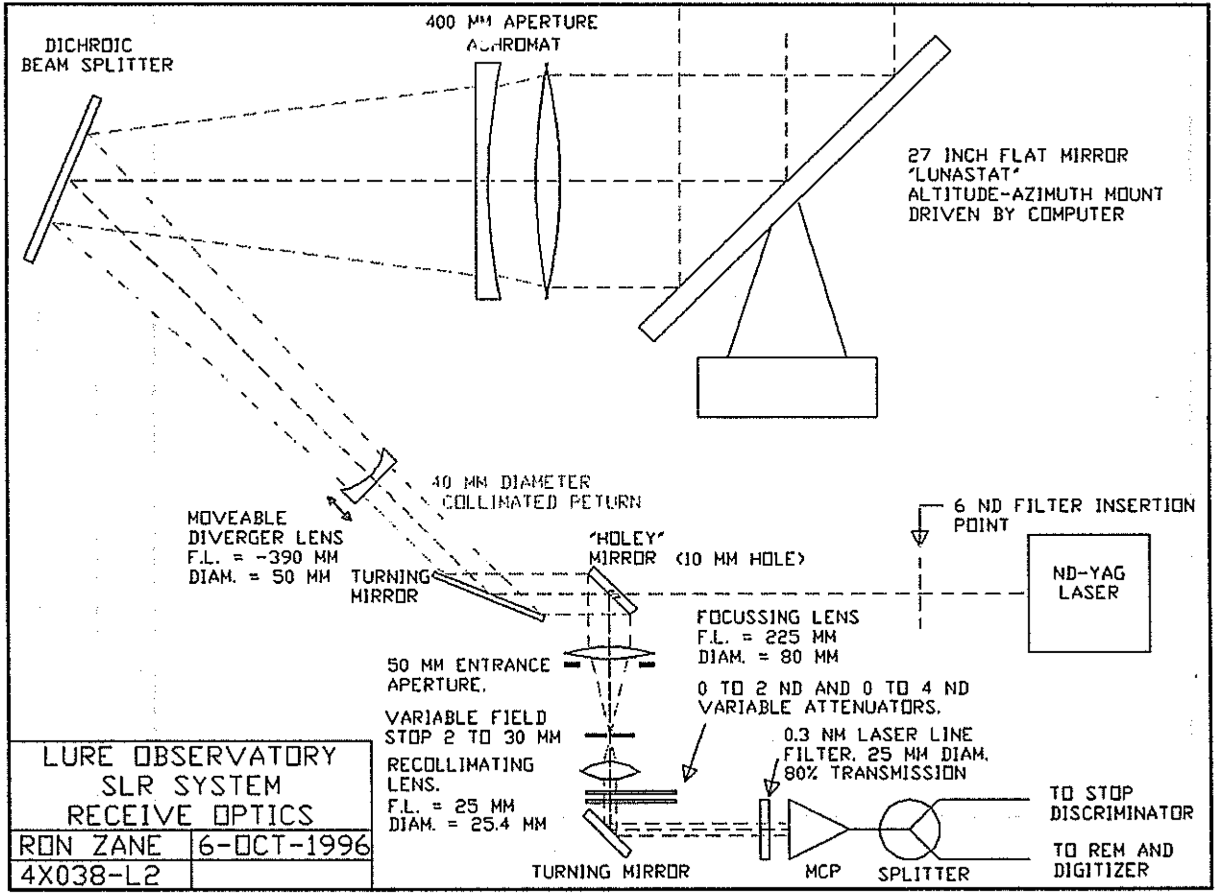

LURE OBSERVATORY
SLR SYSTEM
RECEIVE OPTICS

RON ZANE	6-OCT-1996
4X038-L2	

SPAD DETECTORS FOR RANGING WITH SUB-MILLIMETER BIAS

I.Prochazka, K.Hamal

Czech Technical University, Brehova 7
15 19 Prague 1, Czech Republic
fax +42 2 85762252, prochazk@mbox.cesnet.cz

B.Greene

Electro Optics Systems, PtyLtd, Queanbeyan,NSW, Australia

The SPAD detectors have proven to be the effective detectors for satellite laser ranging, principally because of the low bias obtainable in a single photo electron mode. The low bias property of the SPAD is a crucial feature, as bias reduction is the highest priority in global SLR. It is possible to obtain sub-millimeter bias in a SLR system using SPAD provided the return rate is low, under the standard ranging conditions not exceeding 10%.

However, the low return rate imposes some limitations on station performance also. In particular synchronous SLR data is valid only for occasions [shots] when four stations acquire a target simultaneously. It is obvious, that to obtain a realistic synchronous ranging data rate, the relatively high return rates at each station is needed. In addition, for non-synchronous SLR it is also an advantage to acquire a high number of valid return within a satellite pass, so that tracking efficiency is optimized.

Various techniques for operating a SPAD detector with a high single shot resolution and a low bias is discussed. The design of the new generation SPAD detectors which can be operated in low bias mode even at high return rate is given. The proposed devices have the advantage that they may be operated as a conventional SPAD, they use the same satellite optical depth models as for the conventional SPADs [ie it is backwards compatible] and raw , uncorrected, data is available for the corrected device.

10th Intenational Workshop on Laser Ranging Instrumentation, Shanghai, China, November '96

GOALS

Ranging on SPAD with sub-millimeter bias

- LOW DETECTOR INDUCED RANGE BIAS
- SUB-MILLIMETER BASELINE ACCURACY
- SINGLE SHOT RESOLUTION (rms)
  < 4 millimeters on terrestrial
  < 5 millimeters on satellite
- SYSTEM TEMPORAL STABILITY
  < 4 psec / hour half peak to peak
- PRODUCTIVITY AND DATA QUALITY
  dark count
  data rate (synchron. ranging)
  data distribution

I.Prochazka, K.Hamal, B.Greene, Shanghai,'96

RANGING ON SPAD JITTER STATUS QUO

application	site (laser)	calib. / ERS-1
SLR	RGO (100 psec)	9 mm / 10-12 mm
	SALRO (100 psec)	9 mm / 10-12 mm
	Helwan 2 (35 psec)	8 mm / 10 mm
	Graz old (35 psec)	8 mm / 10 mm
indoor	Prague (30 psec)	* 4 mm
spectroscopy	Berlin (fsec)	* 3 mm

Single photon ranging limit, 3V above
* FWHM = 2.4 * RMS

I.Prochazka, K.Hamal, B.Greene, Shanghai'96

SPAD TIMING RESOLUTION LIMITS

- voltage above break
  2.5 ..5 (11) Volts above break
- temperature
  +22 . -90 Centigrades
- data distribution
  new data processing procedures
  rms = fwhm / 2.4
- signal strenght dependence

I.Prochazka, K.Hamal, Prague, July '96

RANGING JITTER REDUCTION - POSSIBLE SOLUTIONS

- VERY LOW ECHO RETURN RATE
  The single photoelectron echoes may be guaranteed by an extremely low echo return rate, 2 % or less.
- TIME WALK COMPENSATION
  A fast analog circuit is used to monitor echo signal strength and to adjust the detector propagation delay to compensate for the time walk effect.
- SINGLE PHOTOELECTRON ECHOES SELECTION
  The echo signal strength is monitored, the multi PE echoes are ignored.
- SIGNAL STRENGTH MONITORING
  The echo signal strength is monitored, the time walk is software compensated

Under normal conditions, the echo signal strength is fluctuating typ. 1 : 100

I.Prochazka, K.Hamal, B.Greene, Shanghai '96

SPAD parameters vers. bias above break

Cooled 200um chip,30ps electr.32ps laser

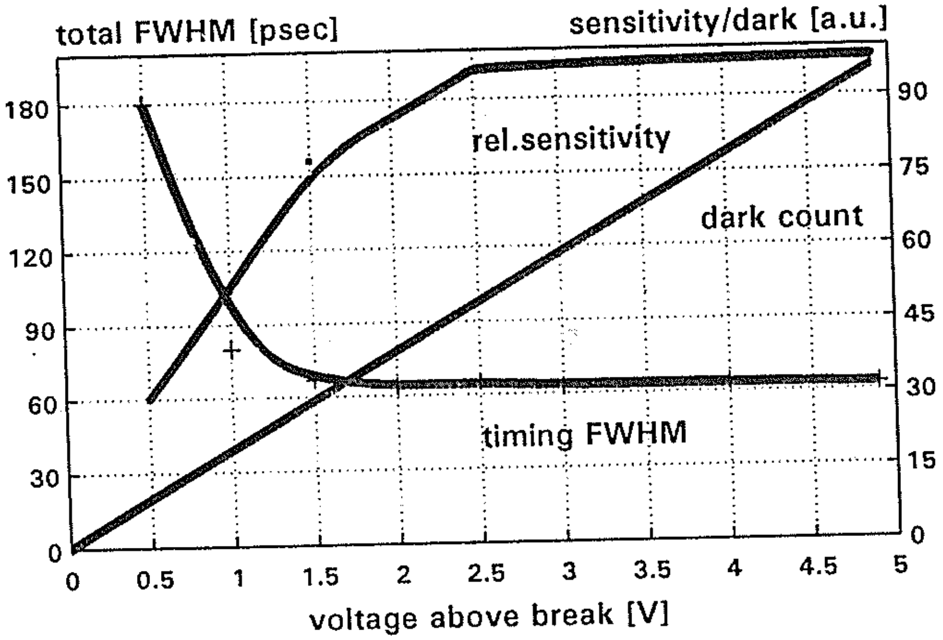

I.Prochazka, January, 95

SPAD timing jitter vers.cooling

Chip SN 23790,200um, comparator KP

Electronics&laser contrib. deconvoluted

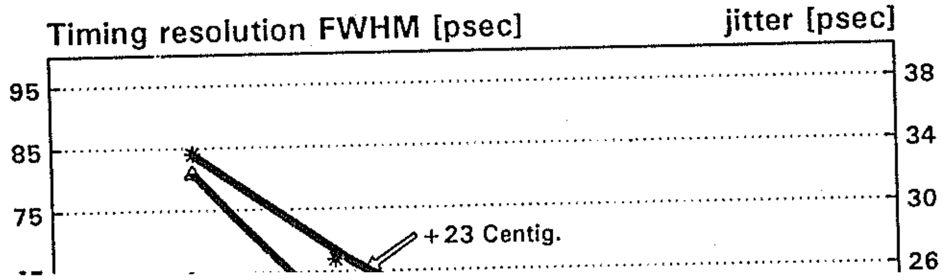

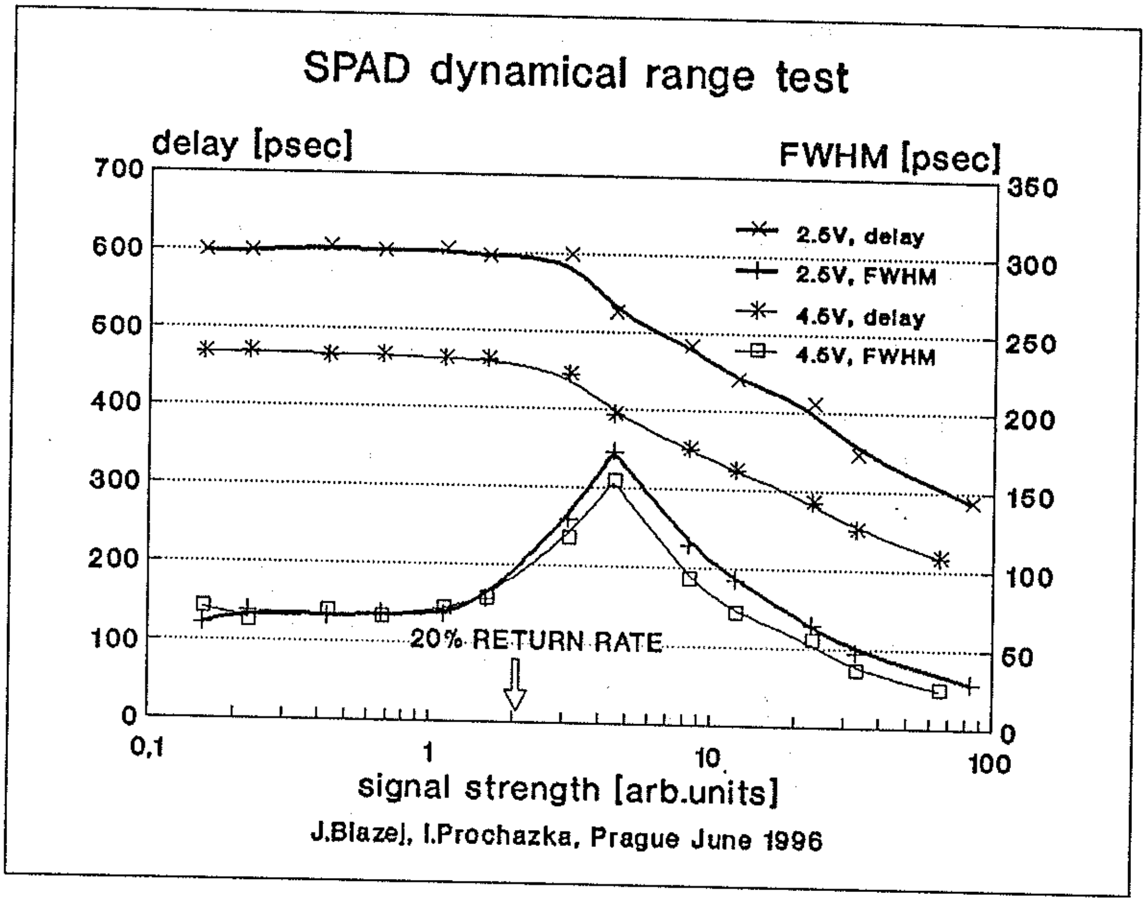
SPAD dynamical range test
delay [psec]
FWHM [psec]
700
600
500
400
300
200
100
0
350
300
250
200
150
100
50
0
2.5V, delay
2.5V, FWHM
4.5V, delay
4.5V, FWHM
20% RETURN RATE
0,1
1
10
100
signal strength [arb.units]
J.Blazej, I.Prochazka, Prague June 1996

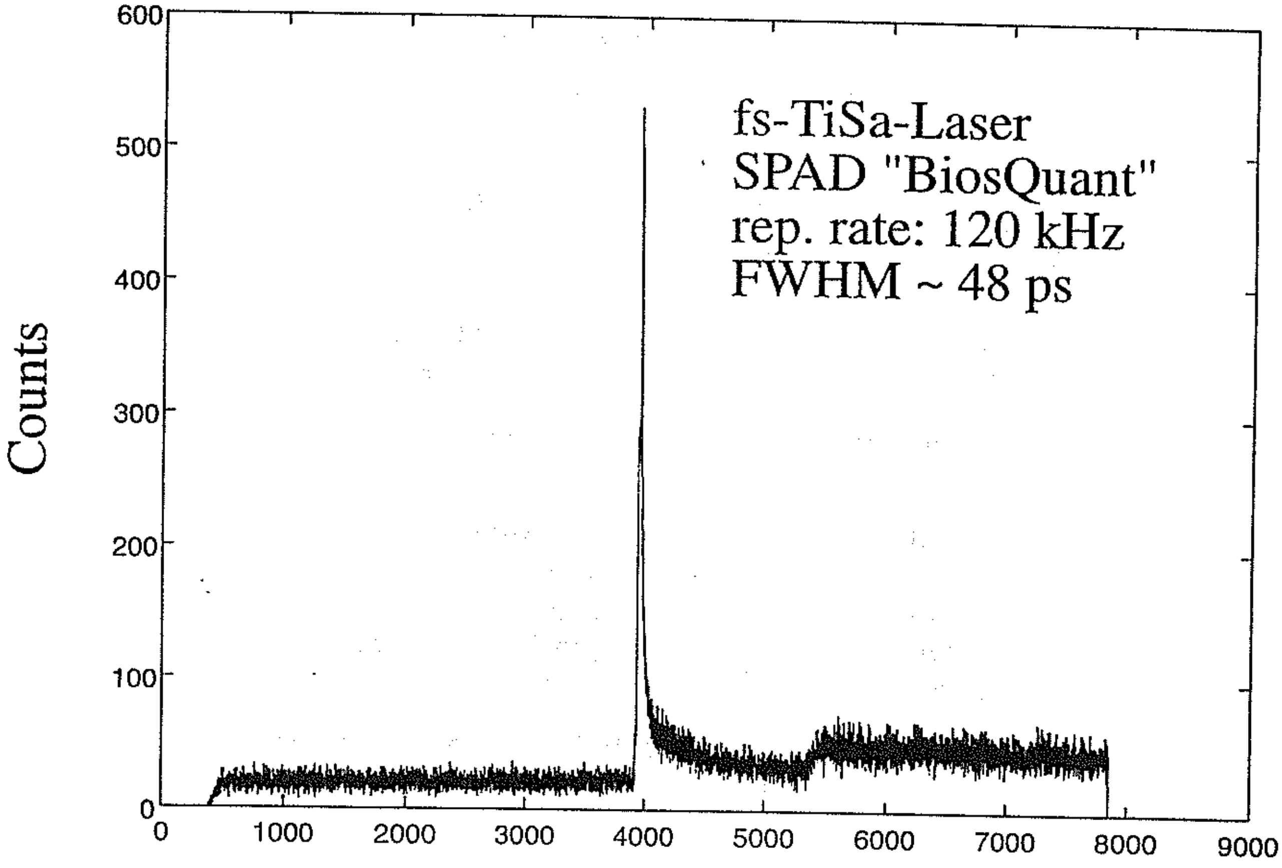
Counts
600
500
400
300
200
100
0
0
1000
2000
3000
4000
5000
6000
7000
8000
9000
fs-TiSa-Laser
SPAD "BiosQuant"
rep. rate: 120 kHz
FWHM ~ 48 ps

POSSIBLE SOLUTIONS COMPARISON

advantages	limitations
LOW RETURN RATE /RGO • simple,NO additional hardware • minimal range bias • satellite signature solved • high timing stability	• low return rate • synchron.ranging data rate -> 0 %
TIME WALK COMPENSATION /Graz • existing hardware • RMS < 4/5 mm demonstrated • return rate -> 99%	• timing stability ? • range biases to be solved • sat.signature to be solved
SINGLE PE ECHOES SELECT./Prague • minimal range bias • satellite signature solved • high timing stability • return rate -> 20%	• hardware under development (40 psec gate) • return rate < 20% • others ?
SIGNAL STRENGTH MONITORING /EOS • single/multi PE timing information available • return rate -> 99%	• harware under development (2 psec timing) • others ?

I.Prochazka, K.Hamal, B.Greene, Shanghai '96

CONCLUSION

SPAD detectors for ranging with sub-mm bias

- At the existing /non synchronous/ SLR systems sub-mm range biases are achievable using SPAD at strictly single photoelectron signal levels.
- The single shot resolution < 5 mm RMS is acheivable on standard SPADs 3V above at data rates < 2 %.
- Tha data rate 10% is the best trade off between normal point precision, single shot RMS, bias (RGO)
- For the single / multiple photoelectron ranging systems on SPAD, three schemes are investigated :
  a/ analog compensation of a time walk.
  b/ hardware selection of single PE echoes,only.
  c/ signal strength monitoring and delay correction.
- More experience from the field is needed before the schemes a/-c/ may be generally applied.

I.Prochazka,K.Hamal,B.Greene, Shanghai '96

Auto matic SPAD Time Walk Compensation

G. Kirchner, F. Koidl
Institute for Space Research / Austrian Academy of Sciences
Observatory Lustbühel; A-8042 GRAZ / AUSTRIA

1.0 Introduction

SPADs introduce measurable timewalk effects for varying SPAD input energy; [1]; this effect mainly depends on SPAD type, SPAD operating conditions (voltage above break), SPAD input energy, and laser pulse width; for the Graz SLR system (100 µm Prague SPAD, 10 V above break, 35-ps-laser, few mJ only per SemiTrain pulse) the worst case time walk can reach up to 200 ps when ranging with collimated beam to low satellites (which we have avoided anyway in the past!).

2.0 Measuring Avalanche Pulse Rise Time Differences

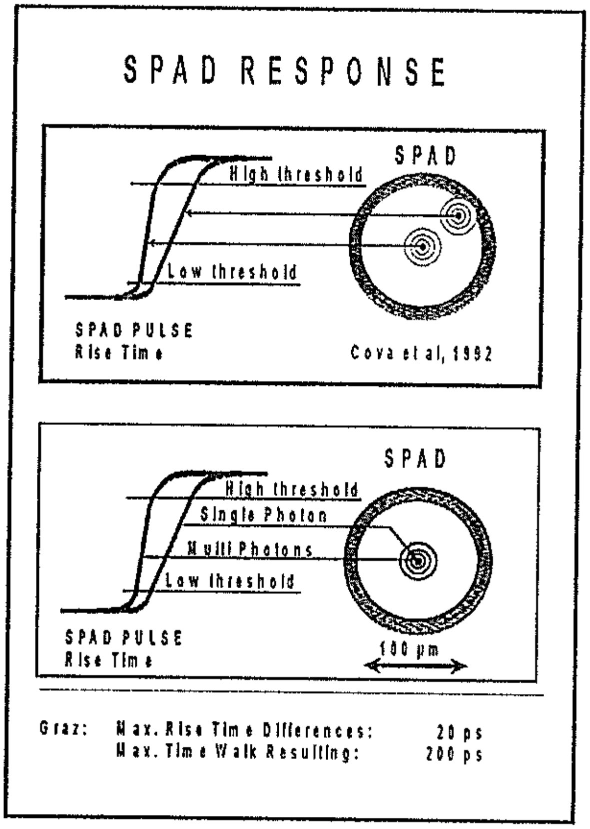

Fig. 1: SPAD Response dependence

In [2], some of the avalanche dynamics of silicon SPADs are explained; as a result, it is shown that the avalanche rise times vary slightly with different locations of the avalanche seed point; in addition, we have seen that this rise time also varies with input energy (Fig.1).

We have verified this already some time ago, and published the results in [3]; we used 2 fast comparators; one triggers near the start of the leading edge (about 10% of maximum amplitude) of the avalanche pulse (which itself is not easily accessible); the second triggers at a higher threshold (about 90% of maximum amplitude). Any differences in the measured delay between the two comparators thus are due to avalanche rise time differences.

The results show that the 200 ps time walk is correlated with a 20 ps rise time difference of the SPAD avalanche pulse.

3.0 Time Walk Compensation

Assuming a linear connection between rise time change and time walk effect, we built a circuit which measures these rise time differences, and uses them to compensate automatically the time walk; the main problem is that - positive - rise time differences of 1 ps have to be translated into - negative - time shifts of 10 ps, while any jitter in the measurement of rise time differences will also be amplified by the same factor of 10; this requires careful selection of circuit design, electronic component selection, PCB layout (e.g. full SMD technique) etc.

The circuits use ultrafast comparators (e.g. AD96687BR) for pulse discrimination, pulse forming and pulse time shifting (Fig.2); the electronics proved to be very stable, adding no measurable jitter to the system; but initial adjustment may be somewhat tricky and time-consuming. After verifying the proper operation and the stability, we installed the final version of the circuit at end of Feb. 1996 into the standard channel of SLR Graz, where it is running now for 9 months of routine ranging, without any need for re-adjustment.

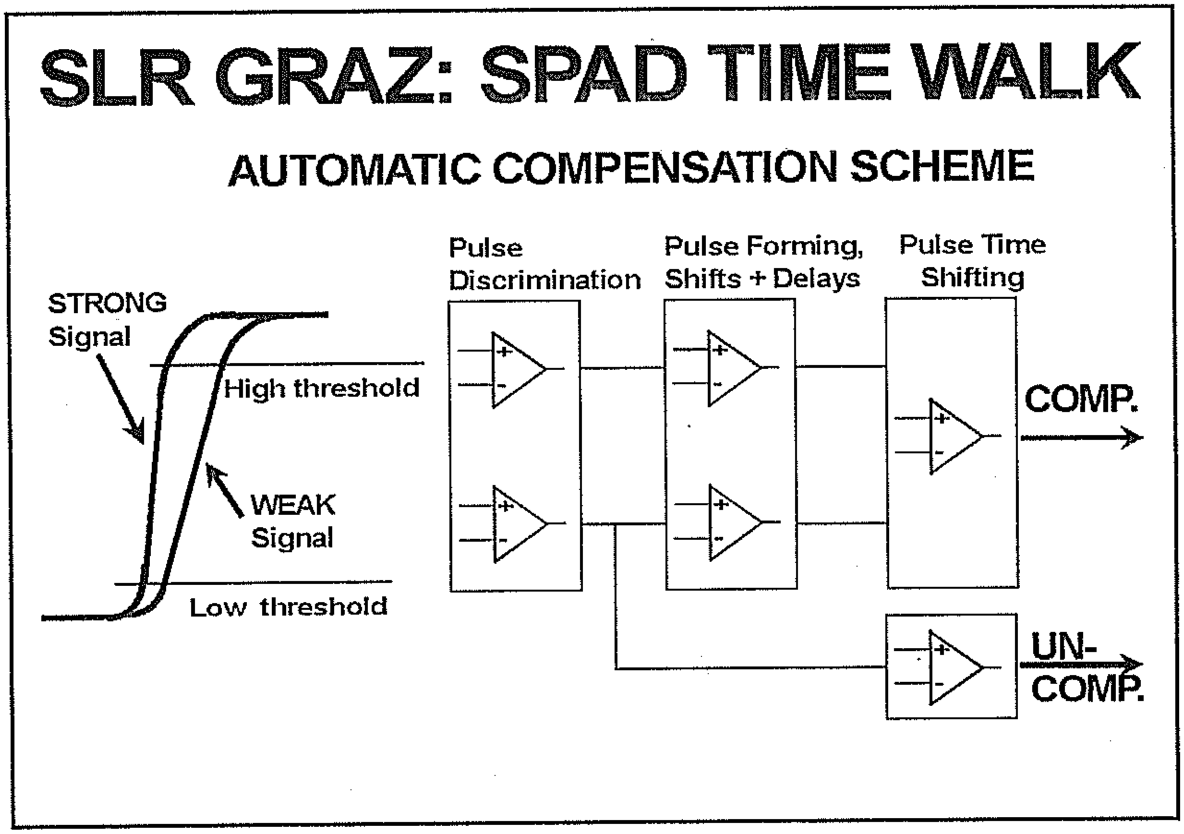

Fig.2: SPAD Time Walk Compensation Schematics

4.0 Results and Plans

The circuit now compensates the major part of the time walk effects (Fig. 3) of the SPAD (and the laser pulse rise time) during routine ranging of SLR station Graz; it reduces all possible time walk effects considerably (from Centimeters to Millimeters); e.g. for LAGEOS, the remaining time walk effects are below 2 mm; as return energy is kept within the tolerable limits by the automatic tracking software, the same results appear also for lower satellites.

There is not only no measurable contribution of the discrimination electronics to the overall system jitter; in contrast to that, the circuit improves significantly the system jitter, because the return signals from satellites and calibration targets always have significant random fluctuations, which had resulted up to now in time walk and therefore jitter; this jitter source is eliminated now completely by the time walk compensation circuit.

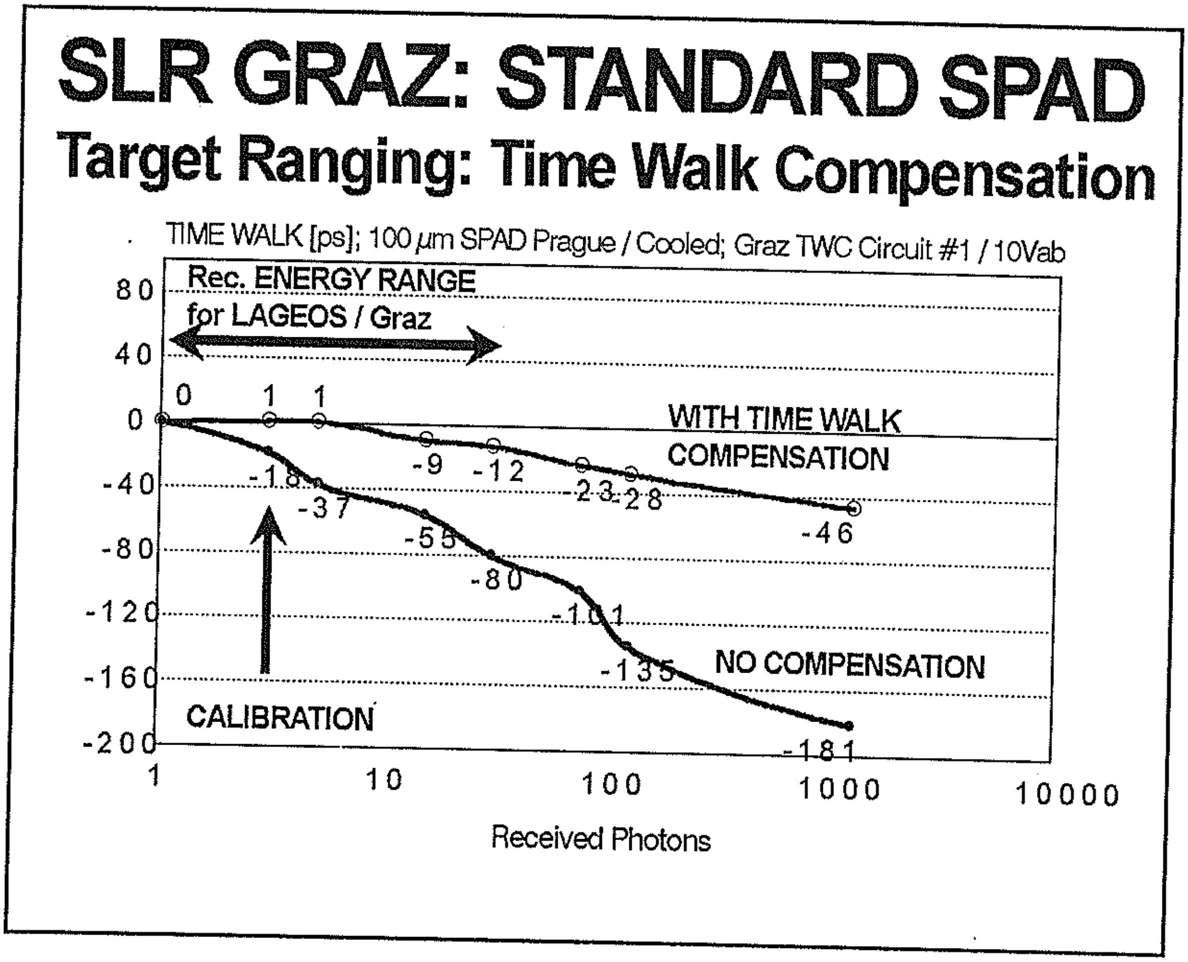

Fig 3: Graz Standard SPAD: Time Walk Compensation

The system now allows full use of a 100% return rate, which is desirable anyway for many obvious reasons, and is necessary also for our planned multi-color measurements. To keep return energy in the range allowed by the time walk compensation circuit, the automatic tracking program [4] identifies not only all valid returns, but checks also for pre-pulses (due to leakage of the pulse selector) indicating higher return signal level; the automatic tracking routines immediately perform some slight offset pointing in such a case, thus keeping return energy - reliably and independent from any observer action - within the tolerable limits [4].

To test the circuit under different conditions, a common project was initiated with the groups in Prague and Potsdam; Prague assembled a 200-µm SPAD, with 2-stage Peltier cooling, optics and housing; Graz built, integrated and adjusted the complete time walk compensation circuit, which also operates the SPAD at 10 Volts above break; adjustment was performed using the Graz laser (35 ps pulse width, similar to the Potsdam laser); for test and comparison purpose, an additional uncompensated output (Fig. 2) was added. Slightly different adjustments for this Potsdam setup were tested in Graz (Fig. 4), showing again possible time walk reduction to below ±1 mm for a range from 1 to more than 100 photons; or to below ±4 mm for a range from 1 to more than 1000 photons (limited by increasing pre-pulse numbers).

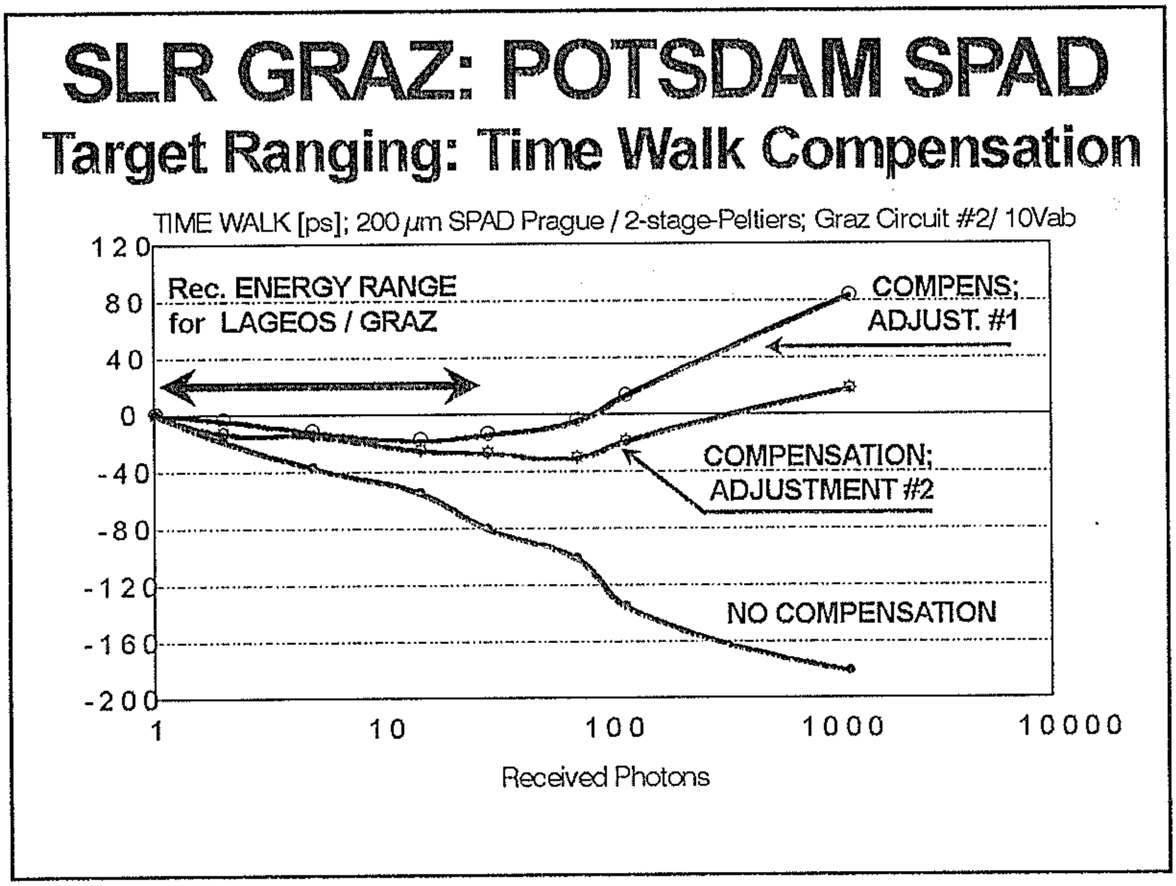

Fig. 4: SPAD Time Walk Compensation, Potsdam Test

The tests in Potsdam to the calibration target gave the same results, demonstrating the possible transfer of the technology to other SPAD stations. The unit is still in Potsdam, to make some more tests - including to satellites -, and will be made available than also for other interested groups for tests. In the mean time, we try to implement further improvements (e.g. faster comparators, now available).

We intend also to build such circuits for other types of APDs. In addition, we have started now to develop a circuit which just measures the rise time differences, makes it available to the computer, and will allow time walk compensation by software, as published by [5] in Shanghai.

References:

[1] Determination of Satellite Signatures and Time Walk Effects in Graz. G. Kirchner, F. Koidl; 9th International Workshop on Laser Ranging Instrumentation, Canberra, 1994; Proceedings, p. 107

[2] Tracking Capabilities of SPADs for Laser Ranging. Cova et al.; 8th International Workshop on Laser Ranging Instrumentation, Annapolis, 1992

[3] Proceedings of Annual Eurolas Meeting; G. Kirchner, F. Koidl; Munich, 3/1995; p 73

[4] Automatic Tracking Software at SLR Graz; G. Kirchner, F. Koidl; in these proceedings

[5] SPAD Detectors for Ranging with Sub-Millimetre Bias; K. Hamal, I. Prochazka, B. Greene; in these proceedings

Large-aperture germanium detector package for picosecond photon counting in the 0.5–1.6-μm range

I. Prochazka and K. Hamal

Czech Technical University, Brehova 7, 115 19 Prague 1, Czech Republic

B. Greene

Electro Optics Systems, Pty. Ltd., Queanbeyan, NSW, Australia

H. Kunimori

Communication Research Laboratory, 4-2-1 Nukui-Kitamachi, Koganei, 184 Tokyo, Japan

Received March 25, 1996

We report the design, construction, and parameters of a detector package based on a germanium avalanche photodiode operated in the Geiger mode cooled to 77 K. The new design of the active quenching circuit, proper diode structure, and cryogenic cooling setup permitted us to increase the detector's active area to 0.1-mm diameter while maintaining an acceptable dark-count rate, timing resolution, and photon-counting sensitivity at 1.54 μm. The active-area size and the compact design of the detector package permitted its application in satellite laser ranging at 0.532- and 1.543-μm wavelengths, yielding subcentimeter ranging precision. © 1996 Optical Society of America

The large-aperture germanium detector package is of general interest for several applications: time-resolved spectroscopy, laser-induced fluorescence, optical-time-domain reflectometry, laser ranging, and others aimed at developing a large-aperture single-photon counter for the near-infrared region. At present the most promising technique for detecting a single photon by use of a solid-state detector is the use of an avalanche photodiode (APD) operated in the Geiger mode. In this operation mode the diode is biased above its breakdown voltage; no current flows until an avalanche is triggered by an incoming photon or a thermally generated carrier. The current pulse rise time marks the photon's arrival time. An external electrical circuit, either passive or active, is used to quench the avalanche and to reapply the bias to the diode.[1]

Our previous research and development in the field of single-photon avalanche diodes resulted in a large-aperture silicon-APD-based detector package with an active quenching circuit, well adjusted for the applications mentioned above.[2] Recent developments have produced an APD with an active area 200 μm in diameter, a timing resolution of 44 ps FWHM, and a dark-count rate below 10 kHz. The APD is cooled by a three-stage thermoelectrical cooler enclosed in a vacuum package. These silicon-based APD's have been used to detect single photons in the near-infrared range up to 1.55 μm.[3] However, the quantum efficiency of such detectors at 1550 nm ($10^{-4}-10^{-6}$) is not considered adequate for most applications. We have made several attempts to increase the residual quantum efficiency of the silicon APD in the near infrared by replacing the silicon with GeSi as a starting material; although research continues, the results are not encouraging.

There are now two alternatives: germanium- and InGaAs-based diodes for photon counting in the near-infrared region for fiber optics at 1.3 and 1.55 μm, for spectroscopy and for laser ranging in the so-called 1.54-μm eye-safe window. The germanium detector-based on a commercially available APD of 30–50-μm diameter shows interesting results.[4,5] On the other hand, several applications including laser ranging require an active-area diameter of not less than 100 μm, as the small detector area limits the field of view of the system receiver. For example, a satellite laser ranging station using a 1.5-m-diameter telescope and a 100-μm diameter detector has a field of view of the entire receiver of 8 arcsec. This is the ultimate minimum for satellite laser ranging and optical communication applications as well.

InGaAs diodes manufactured by EG&G Judson, 100 μm in diameter at a 1.55-μm wavelength, have been tested for relative sensitivity, timing resolution, and dark-count rate at temperatures from 300 to 77 K. Photon-counting operation was achieved at temperatures below 240 K. The detector performance was not satisfactory for ranging applications, as the timing resolution was not better than 600 ps and the quantum efficiency did not exceed several percent at 1.55 μm.

Germanium has been the favored semiconductor material for APD structures for near-infrared detection. The typical spectral responsivity curve of a germanium APD is shown in Fig. 1. The solid curve represents the EG&G Judson data sheet; the dashed line is the extrapolation. There is strong demand for a single detector to detect photons in the spectral range 0.5–1.6 μm. Photon-counting detector parameters of interest are timing resolution, sensitivity, and dark count; all these depend on the diode bias above its breakdown. In general, photon-counting sensitivity increases with the bias above the breakdown and saturates at a certain level. The dark-count rate rises with the bias above the breakdown. The timing resolution improves with

0146-9592/96/171375-03$10.00/0

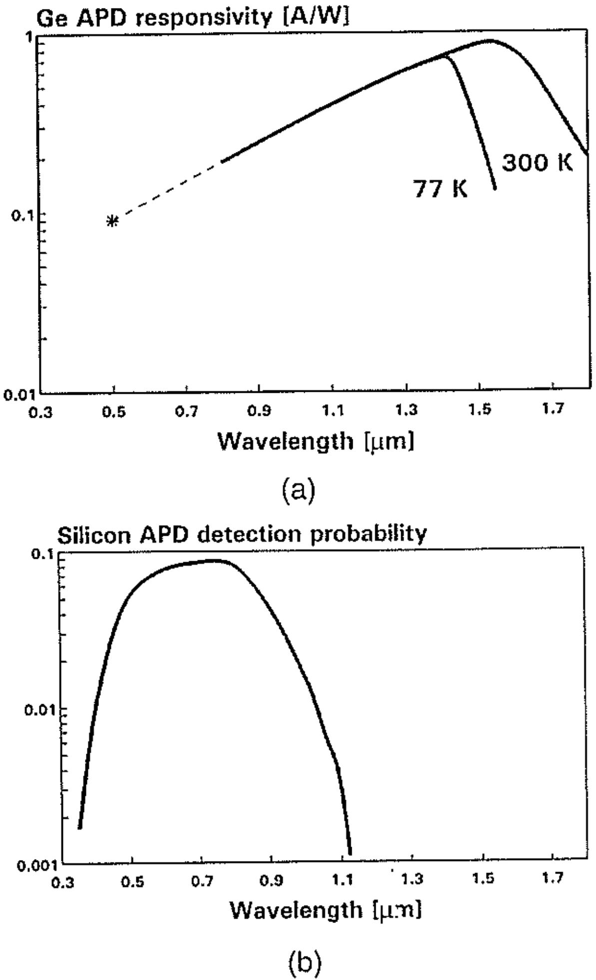

Fig. 1. Spectral responsivity of germanium- and silicon based APD's. (a) Solid curves, germanium APD data from the EG&G Judson infrared detector data sheet (EG&G, Montgomeryville, Pa., 1994); dashed line, extrapolation toward shorter wavelengths. (b) Silicon APD data from Ref. 2.

the bias above the breakdown voltage and saturates at several volts above the break. Therefore each application requires a compromise among these three parameters for a given detector configuration.

In developing the germanium-based single-photon avalanche diode we also examined photodiodes manufactured by NEC, EG&G Judson, and Hamamatsu. For photon-counting operation in the Geiger regime these diodes have to be cooled to 77 K. To optimize the germanium APD operation we modified the existing active quenching scheme to reduce the time during which the current is flowing through the diode. The circuit allows the APD to operate in the Geiger mode when biased to 3 V above the breakdown voltage. To cool the APD we designed a novel cryostat, which permits the incoming light to be focused onto the diode's active area, using optics with a focal ratio equal to unity. The cryostat is compact and fieldable, operates in any orientation, and has a liquid-nitrogen refill interval of 14 days.

To measure the photon-counting timing resolution of the detector we applied a time-correlated photon-counting technique consisting of a Hamamatsu PLP01 laser diode pulser at 0.8-μm wavelength, a time-to-amplitude converter, and a multichannel pulse amplitude analyzer card in a personal computer. The timing resolution of the electronics chain is 30 ps FWHM, and the laser pulse duration is 32 ps FWHM. An example of the waveform of the laser

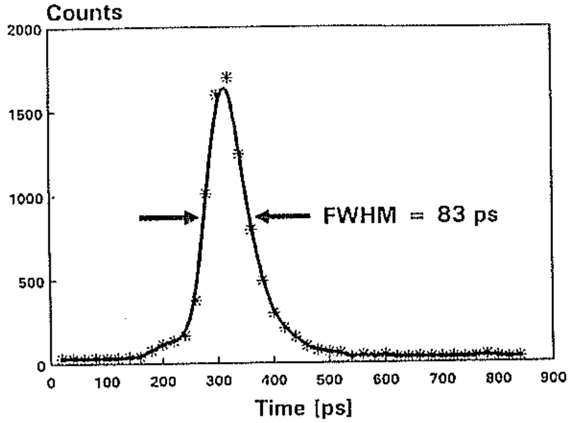

Fig. 2. Waveform of a 32-ps optical pulse from a laser diode. The APD was biased 1.7 V above the break voltage; the timing electronics contribution FWHM was 30 ps.

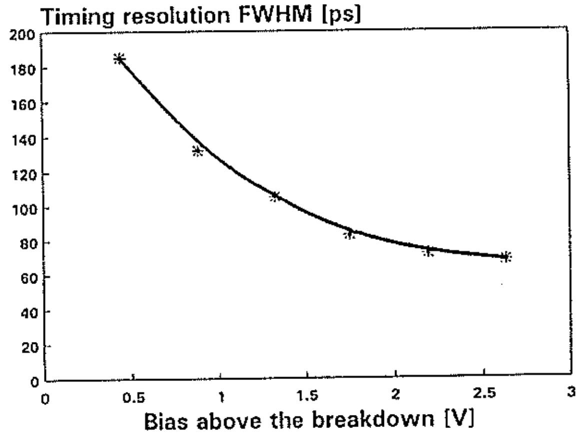

Fig. 3. Timing resolution of the germanium photon counter versus bias above the breakdown voltage.

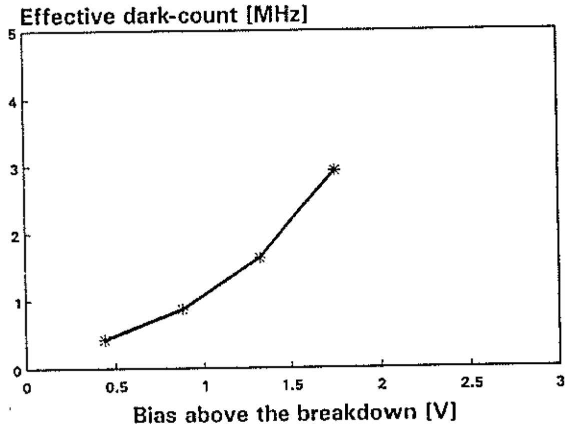

Fig. 4. Effective dark-count rate of the detector package versus APD bias above the break voltage. The APD was operated in an active quenching mode gated with a 10-Hz repetition rate.

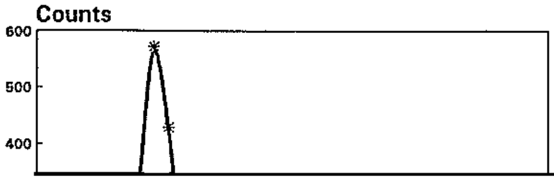

fit into the 1.54-μm eye-safe window. Using a 30-ps pulse duration laser and a ranging electronics resolution of 75 ps FWHM, we obtained the distribution of measured values shown in Fig. 5, resulting in subcentimeter range precision when we ranged the ground targets. What is to our knowledge the first eye-safe

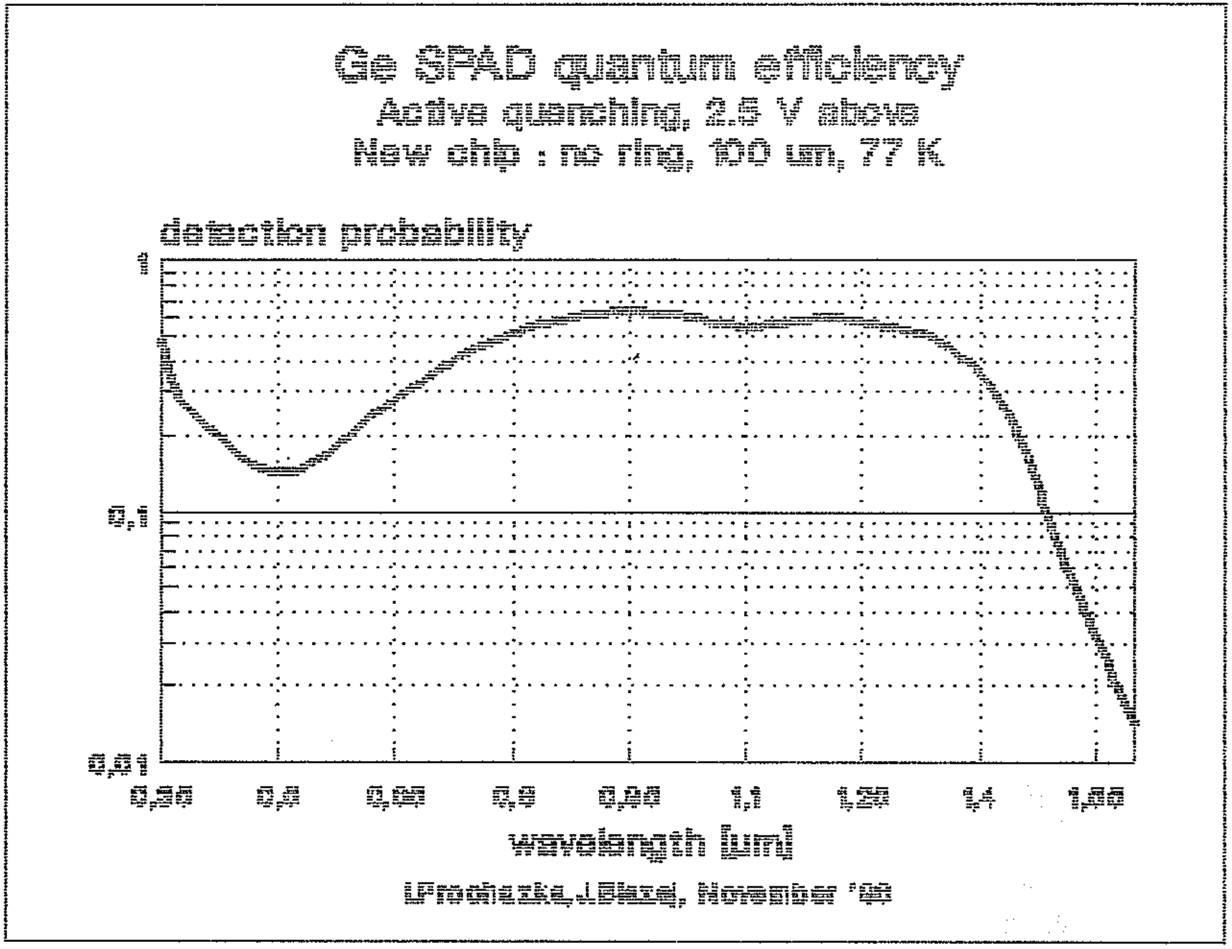
Ge SPAD quantum efficiency
Active quenching, 2.5 V above
New chip : no ring, 100 um, 77 K
detection probability
1
0,1
0,01
0,35
0,5
0,65
0,8
0,95
1,1
1,25
1,4
1,55
wavelength [um]
I.Prochazka,J.Blazej, November